Insitu Sensing and Analysis of Turbulence - Investigation to Enhance Fine-Structure Turbulence Observation Capabilities of Autonomous Aircraft Systems

by

Abhiram Doddi

B.S., B.M.S College Of Engineering, 2016

A thesis submitted to the

Faculty of the Graduate School of the

University of Colorado in partial fulfillment

of the requirement for the degree of

Doctor of Philosophy

Department of Aerospace Engineering Sciences

2021

Committee Members:

Lakshmi Kantha

Dale Lawrence

David Fritts

Thomas Lund

Julie Lundquist

Doddi, Abhiram (Ph.D., Aerospace Engineering)

Insitu Sensing and Analysis of Turbulence - Investigation to Enhance Fine-Structure Turbulence Observation Capabilities of Autonomous Aircraft Systems

Thesis directed by Prof. Lakshmi Kantha and Prof. Dale Lawrence

The advent of mobile observation platforms made possible by advances in small Unmanned Aircraft Systems (sUAS) technology has revolutionized the landscape of Observational Meteorology. sUAS are proven to be safe, reliable, economical, and easy-to-deploy atmospheric sensing platforms. Unmanned aircraft can sample on flexible flight trajectories, have increased observation range, and are increasingly equipped with miniaturized high-resolution sensing instruments, making them instrumental for targeted observations of atmospheric turbulence. The principal objectives of the investigations described in this dissertation were twofold. First, to improve the accuracy and reliability of current turbulence sensing capabilities of the University of Colorado DataHawk UAS. We explore the current landscape of observational turbulence and develop novel strategies to advance fixed-wing UAS turbulence measurement capabilities. Second, to obtain insightful turbulence data products to further our understanding of complex, small-scale turbulence processes. Challenges in turbulence data processing, analysis strategies, and interpretation of UAS sensed data are discussed. Turbulence measurements made using DataHawk

UAS during the Instabilities, Dynamics, and Energetics accompanying Atmospheric Layering (IDEAL) observational campaign are the basis for all investigations presented in this document.

Contents

List of Tables

List of Figures

Chapter 1

Introduction

The troposphere is the most accessible layer of the Earth's atmosphere. It generally extends up to $\sim 12km$ from the surface and contains about 80% of the atmosphere's mass. It exhibits complex yet fascinating, predominantly multi-scale, turbulent fluid flow phenomena. Atmospheric turbulence is ubiquitous and plays crucial roles in the transport of momentum and energy, mixing of constituents, and profoundly impacts local and global weather patterns. Therefore, there is a natural proclivity to characterize the structure, dynamics, evolution, and implications of turbulent atmospheric flows.

Numerous efforts have been made to study atmospheric turbulence in the past. Ground-based radars, lidars, instrumented towers, aircraft, free flying balloons, tethered balloons and kite-borne sensing instruments have been employed in various observational and numerical studies aimed to characterize the morphology and causes of atmospheric turbulence. However, an in-depth understanding of the dynamics of fine-structure atmospheric turbulence has been hampered by the limitations in the sampling strategies of traditional in-

situ observation platforms, and the bandwidth and resolution of the sensors employed.

Recent innovations in small Unmanned Aircraft Systems (sUAS) have paved new avenues for observational meteorology. Since the early 2000s, fixed-wing UAS have been extensively used to probe the convective and stable boundary layers, super-cell thunderstorms, low-level clouds, typhoons, and hurricanes in the lower troposphere (up to $5km$). Equipped with high-resolution sensing elements, UAS enable targeted observations along controlled flight trajectories, and are therefore optimally suited to conduct observations of small-scale flow features. However, in-situ fine-structure turbulence in the free, stably stratified atmosphere using UAS remains vastly unexplored.

The investigations presented in the following chapters are a subset of ongoing efforts at the University of Colorado to measure and characterize the structure and dynamical features of multi-scale turbulent flows in the free stratified troposphere using the DataHawk2 — a lightweight sUAS, engineered and manufactured in-house. The development of DataHawk2 UAS (DH2 hereafter) and the on-board turbulence sensors to conduct measurements during IDEAL campaign (see Section 1.1) constitutes the central theme of all the investigations presented here. The research reported in this dissertation is part of extensive studies made during both ShUREX and IDEAL observational campaigns. The results of ShUREX studies have been reported

in Kantha et al. (2017a, 2019); Luce et al. (2018b,a, 2019) and will not be a part of this dissertation. Instead, the focus is on DH2 measurements conducted during IDEAL campaign.

1.1 IDEAL Observation program

Under stable conditions, the vertical structure of the atmosphere is characterized by thin, strongly stable, non-turbulent "sheets" separated by thicker, less stable and (often weakly) turbulent "layers" (Gage and Green, 1978; Röttger and Liu, 1978). These sheet and layer (S&L) structures are often observed in temperature, humidity, and horizontal winds within the lower troposphere (Balsley et al., 2006, 2003; Chimonas, 1999; Mahrt, 1999; Xing-Sheng et al., 1983; Kantha et al., 2019) and into the edge

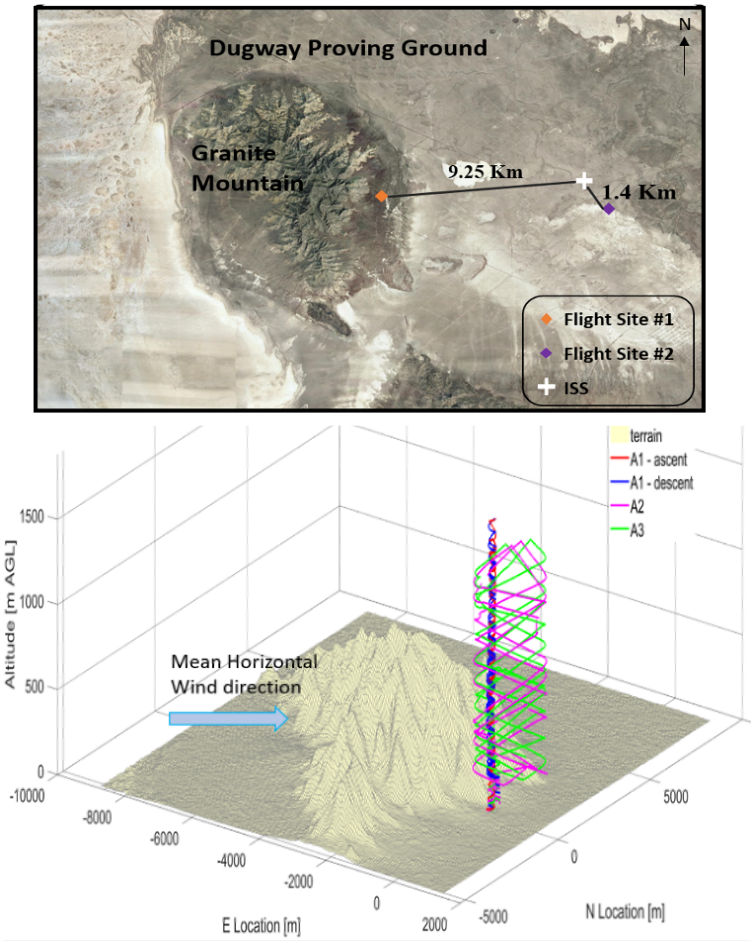

Figure 1.1: IDEAL field campaign location at Dugway Proving Ground (DPG), Utah (top panel). The image shows locations of DH2 observation sites (orange and purple diamonds) and the NCAR Integrated Sounding System (ISS) deployment site (white cross). The satellite imagery was obtained from Google Earth 3D mapping tool.

of the Stratosphere (Barat, 1982; Fairall et al., 1991; Gage and Balsley, 1980; Röttger, 1980; Woodman and Guillen, 1974). The S&L structures are known to play an important role in the transport and mixing of heat, momentum, and constituents (Barat, 1982; Chimonas, 1999; Dalaudier et al., 1994; Hunt et al., 1985), as well as important roles in optical (Coulman et al., 1995) and radio wave propagation (Gossard et al., 1984; Luce et al., 2001; Röttger, 1980; Xing-Sheng et al., 1983).

The large-scale vertical features of the layering structures have been qualitatively analyzed using monostatic and bistatic VHF radar observations (Balsley et al., 2006, 2003; Dalaudier et al., 1994; Luce et al., 2001, 1995; Woodman and Chu, 1989). Details have been characterized in terms of typical sheet thickness and stability, thickness of turbulent layers, Richardson Number, and turbulence Reynolds number through in-situ measurements from soundings, stationary observation towers and tethered lifting systems (TLS) (Balsley et al., 2003, 2006; Muschinski et al., 2001a), and more recently, using aircraft (Lawrence and Balsley, 2013; Muschinski and Wode, 1998). High-resolution multi-point measurements of temperature (Barat, 1982; Coulman, 1973; Frehlich et al., 2003; Hunt et al., 1985; Xing-Sheng et al., 1983) and VHF radar estimates (and comparison with theoretical models) of refractive index structure function parameter (C_n^2) (VanZandt et al., 1978; Woodman and Guillen, 1974) have established the intermittent nature of turbulence within deep layers. More recently, quantitative aircraft measurements of tur-

bulence kinetic energy dissipation rate (ϵ) and the temperature structure function parameter (C_T^2) have characterized the small-scale turbulence features within shallow layers (Balsley et al., 2018a; Eaton et al., 1998; Fernando et al., 2015; Muschinski et al., 2001b; Scipión et al., 2016).

Numerous explanations for the prevalence of S&L structures have been proposed. Concurrent observations using VHF radars and in-situ measurements suggest that S&L are the result of multi-scale gravity waves (GWs) interacting with the fine structure (FS) of the background atmosphere (Barat, 1982; Coulman et al., 1995; Luce et al., 1995; Röttger, 1980). Various analytical studies and numerical modeling results support this conjecture (Fairall et al., 1991; Fritts and Rastogi, 1985; Fritts et al., 2009a; Fua et al., 1982; Sidi et al., 1988; Smith et al., 1987; VanZandt et al., 1978). More recent Direct Numerical Simulations (DNS) achieving very high spatial and temporal resolution, primarily addressing multi-scale GW-FS interactions in "stable" environments (Fritts and Wang, 2013; Fritts et al., 2009b, 2013), suggest that Kelvin-Helmholtz instabilities (KHI), GW breaking and intrusions lead to the formation of S&L. Tjernström et al. (2009) suggested that airflow over low-relief terrain (i.e., small-scale mountain waves) are a plausible formation mechanism for S&L in the lower troposphere. However, the formation mechanisms for some S&L structures observed in the moist lower troposphere during ShUREX campaigns remain unknown (Kantha et al., 2019).

A deeper understanding of the formation, morphology, and evolution of

S&L is hampered by current observational methods that are limited by spatial and temporal resolution, and inadequate range and dexterity of measurement platforms (Chimonas, 1999; Muschinski et al., 2001a; Muschinski and Wode, 1998; Tjernström et al., 2009). Additionally, the single-point vertical profiles (instrumented towers, balloon-borne soundings, and TLS) provide little information about the lateral scales of S&L structures (Muschinski and Wode, 1998). The limited lateral-scale characterization and the dearth of high-resolution, quantitative measures of turbulence parameters provide poor guidance for modeling studies employing high-resolution DNS.

The Instabilities, Dynamics, and Energetics accompanying Atmospheric Layering (IDEAL) project was conceived to address this limitation through a synergistic combination of precisely targeted multi-point observations using small unmanned aircraft system (sUAS) measurements guiding DNS modeling to characterize the dynamics driving S&L structures and associated flow features. The first phase of the project featured an observational field campaign to systematically probe stable lower atmosphere conditions, using multiple DH2 UAS, guided by NCAR Integrated Sounding System (ISS) continuous radar profiling, and hourly radiosonde profiling of the lower troposphere. Measurements were conducted employing multiple-DH2, most-commonly in sorties of three aircraft, for in-situ profiling and horizontal and/or slant path sampling. A total of 72 DH2 flights coordinated with 93 balloon-borne radiosondes were deployed supporting the IDEAL field campaign. Additionally,

an array of Surface Atmospheric Measurement Systems (SAMS) collected surface winds, temperature, and relative humidity at $2m$ and $10m$ heights (AGL) to monitor surface and boundary layer activity. Observational locations of IDEAL field measurements are shown in Figure 1.1. Following the field campaign, the second phase focused on high-resolution DNS modeling efforts, guided by the DH2 and radiosonde in-situ observations, to permit more quantitative exploration of S&L formation mechanisms, evolution, and morphology.

Analysis of aircraft and turbulence sensor performance from operations of DH1 (predecessor of the DH2 UAS) during ShUREX2016 and ShUREX2017 field campaigns held in Kyoto, Japan to observe atmospheric boundary layer (ABL) and S&L turbulence in the lower troposphere (Kantha et al., 2017a, 2019)) served to identify the limitations of DH1 turbulence sensors and deficiencies in data quality. Investigations presented in Chapters 2 through 3 were conducted to improve DH2 turbulence sensing ability for the IDEAL observation program. The research discussed in Chapters 4 and 5 were mainly motivated by the intricacies of turbulence data processing, and the complexities of UAS data analysis and interpretation exposed by post-ShUREX and IDEAL campaigns.

1.2 Autonomous UAS: A Modern in-situ Atmospheric Sensing Platform

Instrumented manned aircraft have been traditionally deployed to observe common weather phenomena in the boundary layer, high-level clouds, typhoons, hurricanes, and thunderstorms (Payne and Lumley, 1966; Lenschow, 1972; Cho et al., 2003; Marwitz, 1972; Aberson and Franklin, 1999; Muschinski et al., 2001b). But operational safety and logistical complexities of employing manned aircraft for severe weather observations constrained aircraft deployment and flight range, and increased risks for crew and aircraft. This motivated the development of inexpensive Remotely Piloted Aircraft (RPA) for use in observational meteorology (Chilson et al., 2009; Lawrence and Balsley, 2013).

The last two decades have witnessed the evolution of RPAs operated by skilled remote pilots into autonomous aircraft controlled by sophisticated autopilot systems implementing robust guidance, navigation and control systems (GNC). Legacy RPAs utilized mass-produced hobby model airframes hosting miniature meteorological sensors (radiosonde sensor modules) to measure atmospheric pressure, temperature and relative humidity (T/RH), and were limited to visual line-of-sight flights within the surface layer. Contemporary fixed-wing UAS retain the desirable characteristics of manned aircraft like longer endurance, range, ability to fly dexterous patterns beyond visual line-of-sight, and host miniature and fast electronic. sensor packages. Mod-

ern UAS are compact, cost-efficient, reliable, and low-risk platforms. Some, like the DH2, are specifically engineered to make atmospheric observations. They have been employed in numerous meteorological experiments including verification of radar measurements (Chilson et al., 2009; Kantha et al., 2017a; Luce et al., 2017), measurement of air-mass boundaries (Houston et al., 2012), boundary layer structure characterization (Balsley et al., 2013; Witte et al., 2016) and also arctic environment monitoring (de Boer et al., 2019).

Fixed-wing UAS span a large range of size and capability. Here we classify them by weight into three categories. Weighing between $10kg$ and $30kg$, aircraft like Manta (Thomas et al., 2012a), ScanEagle (Reineman et al., 2013), and Aerosonde (Holland et al., 1992) have large payload capacity and endurance, allowing heavy and sophisticated sensors to be mounted. The mid-tier MMAV (van den Kroonenberg et al., 2008), MASC (Wildmann et al., 2014b), Tempest (Argrow et al., 2011), and SMARTSonde (Chilson et al., 2009) weigh between 5 and $10kg$, are relatively inexpensive to manufacture, maintain, and are conveniently deployed. The smallest UAS platforms, e.g. the DataHawk (DH1 and DH2) (Lawrence and Balsley, 2013) and SUMO (Reuder et al., 2008) have wingspans $< 2m$, weigh $< 2kg$, and have modest payload capacity. However, they are simple to construct and maintain, quick and easy to deploy, and are the most economical and versatile UAS. Elston et al. (2015) provides a detailed account of prominent autonomous UAS platforms, their sensing capabilities and applications.

Atmospheric flows are locally distorted by a UAS airframe. The distortions are prominent at or below scales on the order of the wingspan. Small UAS have small-scale impacts on the background flow and are therefore generally effective for measuring larger-scale features. However, to measure at smaller scales, sensor design and placement on the UAS is crucial to make unperturbed measurements.

1.2.1 DataHawk-2 UAS

The DH2 UAS used for IDEAL campaign (Figure 1.2) is a product of many years of development at the University of Colorado. It is specifically designed to make high-resolution, in-situ observations in the lower troposphere, and for operations in challenging environmental conditions. The precursor DH1 was used in campaigns in Peru (Balsley et al., 2013; Lawrence and Balsley, 2013; Scipión et al., 2016) and Utah (Balsley et al., 2018a; Fernando et al., 2015). The DH2 was used in campaigns in Japan (Kantha et al., 2017a, 2019; Luce et al., 2018a,b, 2019, 2017), Colorado (de Boer et al., 2019), and Alaska (de Boer et al., 2018). Altogether, over 650 science flights have been performed with the DH2, totaling 430 flight hours.

Figure 1.2: DH2 UAS prepared for launch during Multidisciplinary drifting Observatory for the Study of Arctic Climate (MOSAiC) campaign (2019).

Relevant attributes of DH2 UAS to the IDEAL field program are noted below:

- **Low cost.** At approximately $1,000 each, many vehicles can be deployed for a campaign, enabling multiple, simultaneous measurements (as employed extensively for IDEAL) or sequences of overlapping flights to provide continuous measurements over many hours. This also enables observations in marginal conditions (e.g., high winds) that would ground more expensive vehicles due to the risk of loss. Ten DH2 vehicles were available for the 23-day IDEAL campaign.

- **Ruggedness.** The airframe is resilient foam, strengthened by a system of interior spars and flexures that absorb impacts, enabling the vehicle to "bounce" rather than break when landing on unprepared surfaces and encountering unexpected impact with obstacles. It has a no-tail design, since these extended members are easily broken, and unbreakable wing trailing edges and vertical fins. It also has a rear pusher propeller with folding blades to prevent damage to the propulsion system during landing. In the IDEAL campaign, five DH2 aircraft were used extensively, of which two were retired after the campaign due to accumulated wear. No aircraft were lost.

- **Ease of operation.** A custom autopilot provides automatic launch, landing, and vector field flight control (Lawrence et al., 2008), enabling a variety of measurement strategies to be set up with ease and flown

under minimal operator supervision. Flight patterns can also be changed during flight to target specific volumes of interest, e.g., based on real-time measurements — an ability that was extensively used during IDEAL to identify and more thoroughly sample turbulence fields. A bungee cord is used for launch, guided by a simple two-rail launch ramp (see Figure 1.2).

- **Gust-insensitive design.** The unique aerodynamic design eliminates the roll moment due to side-slip, making the vehicle point into a gust rather than roll away from it, enabling well-behaved flight in high-wind and strong turbulence conditions. Normally, flights are not performed when surface winds exceed $10m\ s^{-1}$, or predicted winds aloft exceed $15m\ s^{-1}$. The vector field guidance uses a wind-aware algorithm to stabilize the flight even when wind speed exceeds airspeed. During IDEAL, synoptic winds aloft often exceeded $20m\ s^{-1}$, limiting the flight ceiling to $3km$.

- **Flexible sensor interfacing.** The custom DataHawk autopilot provides multiple serial interfaces (7 UART, 3 I2C, 4 SPI), enabling a variety of sensors to be supported, and their data stored on-board (on a micro SD card), and telemetered to the ground station for real-time display. Tables 1.1 and 1.2 provide details of the sensors employed for IDEAL. Sensors can be installed at various locations in the body or the wings of the airframe without altering the flight dynamics, provided that center

of mass is preserved.

- **Efficiency.** Flight duration exceeds $80min$, making altitudes of $5km$ AGL accessible with a typical $2m\ s^{-1}$ ascent/descent rate, and a lateral range (out and back) of $30km$ at a nominal airspeed of $15m\ s^{-1}$. IDEAL employed circular vertical profiling trajectories to $3km$ altitude, and oblong racetrack patterns extending up to $3km$ laterally from the launch location.

A DH2 UAS equipped with various sensors is shown in Figure 1.3, and sensor characteristics used during IDEAL field campaign are given in Tables 1.1 & 1.2 below:

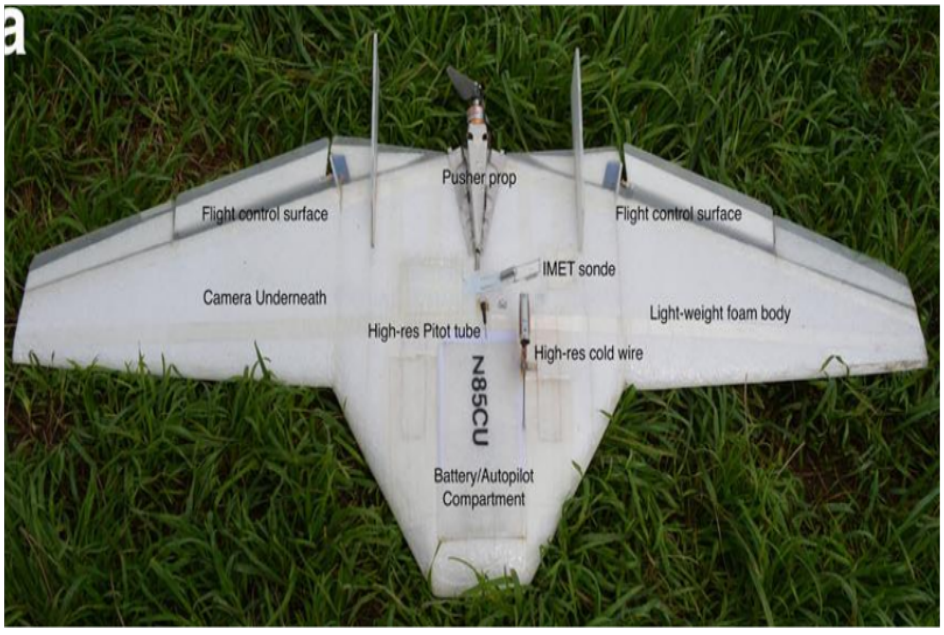

Figure 1.3: DH2 UAS equipped with various sensors during the SHUREX2017 campaign (Kantha et al., 2017a)

DH2 Characteristics		**DH2 Capabilities**	
Wingspan	$1.3m$	Airspeed	$10 - 20m\ s^{-1}$
Mass	$1.3kg$	Duration	$80minutes$
Vehicle Cost	\$1000	Range (one way)	$60km$
Sensor Cost	\$400	Altitude (balloon Drop)	$6km$ AGL
Design	Flying wing, rear propeller	Altitude (ground launch)	$5km$ AGL
Telemetry	IEEE 802.15.4, $900MHz$	Turning radius	$> 50m$
Propulsion	Electric, folding propeller	Climb rate	$< 3m\ s^{-1}$
Autopilot	Custom M4	Down link throughput	$>$ 1500 bytes per second
Control	Auto, operator supervised	Down link update rate	$10Hz$
Power	$11V$ LiPo, $7600mAhr$	Sensor sampling	up to $800Hz$
Construction	Polypropylene foam	Data storage (on board)	Micro SD card

Table 1.1: Characteristics of the DH2 UAS.

Type	**Resolution**	**Accuracy; Range**	**Time Constant; Cadence**
Hor. Location (GPS)	$10cm$	$10m$; worldwide	$0.2s$; $5Hz$
Altitude	$10cm$	$20cm$; $-1km$ to $20km$ MSL	$1ms$; $100Hz$
Time (GPS)	$1ms$	$0.2s$; $1week$	$0.2s$; $5Hz$
In-situ temperature	$0.1C$	$2C$; $-60C$ to $+40C$	$5s$; $10Hz$
Rel. humidity	0.01%	4%; 0% to 100%	$8s$; $10Hz$
Airspeed	$0.05m\ s^{-1}$	$0.2m\ s^{-1}$; $10m\ s^{-1}$ to $20m\ s^{-1}$	$5ms$; $800Hz$
Coldwire temperature	$0.003C$	$2C$; $-60C$ to $+40C$	$0.5ms$; $800Hz$
Hotwire velocity	$0.01m\ s^{-1}$	$0.2m\ s^{-1}$, $10m\ s^{-1}$ to $20m\ s^{-1}$	$0.5ms$; $800Hz$
C_T^2	$10^{-6}m^{-2/3}K^2$	10^{-5}; 1.0	$1s$; $1Hz$
ϵ	$10^{-7}m^2s^{-3}$	10^{-6}; 0.1	$1s$; $1Hz$
$2D$ vector wind	$0.001m\ s^{-1}$	$0.5m\ s^{-1}$; $0m\ s^{-1}$ to $30m\ s^{-1}$	$0.1s$; $1Hz$
IR temperature	$0.1C$	$5C$; $-40C$ to $+40C$	$0.1s$; $10Hz$

Table 1.2: Sensing Capabilities of the DH2 UAS.

Small UAS are gaining a reputation as reliable observational platforms

alongside more established in-situ platforms like radiosondes, tethersondes, and instrumented towers. Despite their widespread applications to large-scale atmospheric flow measurements of T/RH and pressure, autonomous UAS have seldom been tailored to quantify the fine-structure features of turbulent atmospheric flows. The DH2 aircraft, due to its compact form factor ($1.2m$ wingspan and $1.2kg$ mass), is a suitable platform to measure small-scale flow features. However, limited payload capability precludes DH2 from hosting sophisticated, commercially available, often heavy turbulence sensing instruments. This necessitated the development of custom, miniature turbulence sensing instruments as described in this thesis. First, to provide context for these details, an overview of the main research questions that guided this work is presented.

1.3 Guiding Research Questions

Sensing elements with high-bandwidth and low noise floor are desirable to measure motions on a wide range of scales exhibited by turbulent flows. Particle image velocimeters (PIV) provide 3D flow-field imaging, but are too large for use in small UAS. In-situ point sensing is provided by multi-hole pitot (MHP) probes, thin-film anemometers (TFA), and fine wire anemometers and thermometers (FWA and FWT). These have reliably been used to quantify a broad range of turbulence scales represented by the velocity and temperature fluctuations. Commercially available MHP, TFA/FWA/FWT systems

are large, heavy, and expensive; therefore unsuitable to be mounted on small UAS. Therefore, DH2 employs a custom single-board turbulence measurement instrument containing $5\mu m$ diameter Hot-wire (HW) and Cold-wire (CW) sensing elements. A cylindrical shroud protects the fragile sensing elements from debris (dust, rain, snow) in flight and during landings, and shields against insolation. Preliminary wind tunnel tests of protected fine-wire sensors showed signal attenuation at high-frequencies of HW velocity spectra. Further, calibrated CW temperature data sampled on helical flight trajectories during previous DH2 field campaigns indicated periodic artifacts, on the period of one circle, caused by exposure to solar heating. This warranted a better understanding of the distortion effects associated with the shroud, that could lead to a redesign of the protective shroud to minimize/mitigate them. The corresponding research question is as follows:

1. What is the nature of contamination introduced by the protective element on the spectral content of the fine-wire data? How do we quantify these effects? Can the protective shroud be redesigned to mitigate/minimize fine-wire data contamination for parameterizing geophysical turbulence?

UAS measurements of static pressure, T/RH, winds and potential temperature describe the background state of the atmosphere and provide important

insights. But to facilitate comprehensive scientific analysis, raw UAS data need to be processed into derived parameters more indicative of flow physics. Atmospheric flow dynamics are commonly characterized by representative parameters like wind shear, buoyancy frequency (N), Richardson number (Ri), turbulence kinetic energy dissipation rate (ϵ), turbulence temperature dissipation rate (ϵ_T), temperature and refractive index structure function parameters (C_T^2 and C_n^2) to list a few. We limit our scope to deriving robust algorithms to estimate wind vector ($\vec{U}$), ϵ and C_T^2. As we discover in Chapters 4 and 5, these can be tricky to reliably estimate from raw UAS data samples.

Conventionally, the 3D wind vector using aircraft data is estimated by combining the airspeed, aircraft attitude and GNS (inertial) motion data (Axford, 1968). Complex autonomous aircraft dynamics and variable sensor time constants together pose challenges for accurate wind characterization.

TKE dissipation rate (ϵ) is estimated using spectral analysis derived from scaling laws of turbulence as established by Kolmogorov's K41 theory (Kolmogorov, 1962). However, preliminary studies revealed artifacts in velocity spectra (of both pitot and hot-wire anemometer) caused by the UAS. The construction of robust and reliable algorithms to estimate $\vec{U}$ and ϵ is the overarching objective of the second investigation:

2. How can accurate estimates of $\vec{U}$ and ϵ be derived from raw UAS samples? How can the confidence in these estimates be meaning-

fully quantified?

The questions presented in this section provided top-level guidance for the research efforts to improve small-scale turbulence sensing capabilities of UAS.

1.4 Chapter Organization

This document is divided into two parts to address the guiding research questions established in the previous section. Part I consists of Chapters 2 and 3 and is based on the theme of improving raw turbulence measurement capabilities of DH2 UAS to prepare for the IDEAL observation campaign (Doddi et al., 2021). Investigations conducted to redesign the protective shroud and calibration procedures for DH2 turbulence sensors (pitot differential pressure sensor, hot-wire anemometer, and cold-wire thermometer) are discussed. Part II is based on the theme of UAS data processing and consists of Chapters 4 and 5. In these Chapters, novel algorithms for $\vec{U}$, ϵ and C_T^2 estimation from raw data are developed and assessed.

Part I

UAS Turbulence Sensing

Chapter 2

Protected Fine-Wire Turbulence Sensors

Fluid flows in the troposphere occur at high Reynolds numbers. Atmospheric flows transition from laminar to turbulent well before these Reynolds numbers are attained. Turbulent atmospheric flows are sustained by sources like shear, convection, and topographic effects. Turbulence, seemingly irregular and random, is a multi-scale stochastic flow property that exhibits universal cascading kinetic energy conversion between a large scale (called outer scale) dictated by the source, and a small scale (called inner scale) limited by fluid viscosity. The Universal Equilibrium Theory of turbulence (Kolmogorov, 1962) hypothesizes that the separation between the outer and inner scales is governed by a dimensionless number called the Buoyancy Reynolds number Re_b (Tennekes and Lumley, 2011). Thus, turbulent flows of higher (lower) Re_b contain a broader (narrower) range of spatial and temporal scales. For instance, the outer and inner scales for boundary layer turbulence are $\sim 1km$

and, $\sim 10mm$ respectively (Tennekes and Lumley, 2011). So comprehensive analysis of turbulence requires measurements that resolve motions on a wide range of scales, and this is particularly challenging for the small energy contained within the small scales. Therefore, high-bandwidth and low noise floor are desirable traits of turbulence measurement instruments.

Measurements of atmospheric turbulence have been conducted using fine-wire and sonic anemometers mounted on instrumented towers or hoisted using tethered kites/balloons (Coulman, 1973; Balsley et al., 2013), and more recently using manned aircraft (Muschinski et al., 2001a,b; Meischner et al., 2001; Dehghan et al., 2014). UAS are seldom equipped with sensors able to measure small-scale turbulent motions. Contemporary UAS platforms such as MMAV (van den Kroonenberg et al., 2008), Manta (Thomas et al., 2012b), MASC (Wildmann et al., 2014a), ALADINA (Altstädter et al., 2015), SUMO (Bäserud et al., 2016), and OVLI-TA (Alaoui-Sosse et al., 2019) combine high-cadence multi-hole pitot sensor data with GNS and aircraft attitude data (from estimators using inertial measurement units) to estimate 3D turbulent wind fluctuations. Canter (2019) and Witte et al. (2016) report that multi-hole probes require tedious in-flight calibration procedures in addition to wind tunnel calibration, and generally have bandwidths $< 100Hz$, which makes them undesirable to measure small-scale structures. Witte et al. (2016) implemented a custom 1D HW anemometer on BLUECAT UAS (fixed-wing UAS weighing $8kg$ with $3m$ wingspan) able to measure velocity fluctuations

up to $20kHz$. But the low signal-to-noise ratio (SNR) of the HW system severely degraded measurements above $100Hz$.

The miniature turbulence measurement system on DH2 UAS consists of a hotwire (HW) anemometer and a coldwire (CW) thermometer (see Section 1.2.1). These custom fine-wire sensors have inherent time-constants of $\sim 0.5ms$ and sampling rates of $800Hz$. This is sufficient to accurately resolve turbulence scales as small as $\sim 0.05m$ (at a nominal airspeed of $15m\ s^{-1}$). In laboratory experiments conducted in wind and water tunnels, constant temperature-controlled fine-wire/thin-film anemometry techniques (Saarenrinne and Piirto, 2000), using fine-wires $\sim 5\mu m$ in diameter and $\sim 1mm$ in length, are known to provide excellent turbulence data due to their ability to resolve velocity fluctuations at bandwidths exceeding $20kHz$ with adequately high SNR. These delicate fine-wire sensors and associated electronics are generally suitable for use only in carefully controlled laboratory environments, unlike UAS that primarily operate in rugged terrain and are exposed to environmental factors like rain, snow, dust etc., during flight and debris during landing. The fragile fine-wire sensing elements are susceptible to damage when exposed to harsh UAS operating conditions. Protective elements, such as a cylindrical shroud, seemed necessary to make fine-wire sensors conducive to DH2 operating conditions. Preliminary tests of protective designs in the wind tunnel revealed spectral artifacts in HW measurements, likely caused by the distorting effects of these protections.

In the rest of this chapter, we focus on characterizing the distorting effects of protective elements through numerous wind tunnel studies and on the redesign of these protections to mitigate spectral artifacts for geophysical measurements. Section 2.1 describes the universal characteristics of turbulence energy spectrum using Kolmogorov's universal equilibrium theory of turbulence and highlights some problems observed in DH2 HW velocity spectra. In Sections 2.2 and 2.3, wind tunnel studies assessing various design features of the protections are presented. Results and insights from the wind tunnel experiments, and prominent features of the redesign, are discussed in Section 2.5.

2.1 Protected fine-wire turbulence sensing: Problems

The Universal Equilibrium Theory of turbulence (Kolmogorov, 1962) (hereafter, K41) utilizes the concept of dimensional analysis, combined with spectral analysis to describe the spectrum of turbulent kinetic energy (TKE). The one dimensional energy spectrum $E(\kappa)$ of stationary homogeneous isotropic turbulence is shown in Figure 2.1. K41 establishes that $E(\kappa)$ in the inertial subrange (between the outer scale and inner scale) follows a $\kappa^{-5/3}$ roll-off with wavenumber κ. Turbulence kinetic energy is produced by the source at large scales and cascades by virtue of turbulent eddy interactions down to smaller scales, where viscous effects overwhelm the inertial effects and dissipate the macroscopic kinetic energy into heat. This mechanism constrains

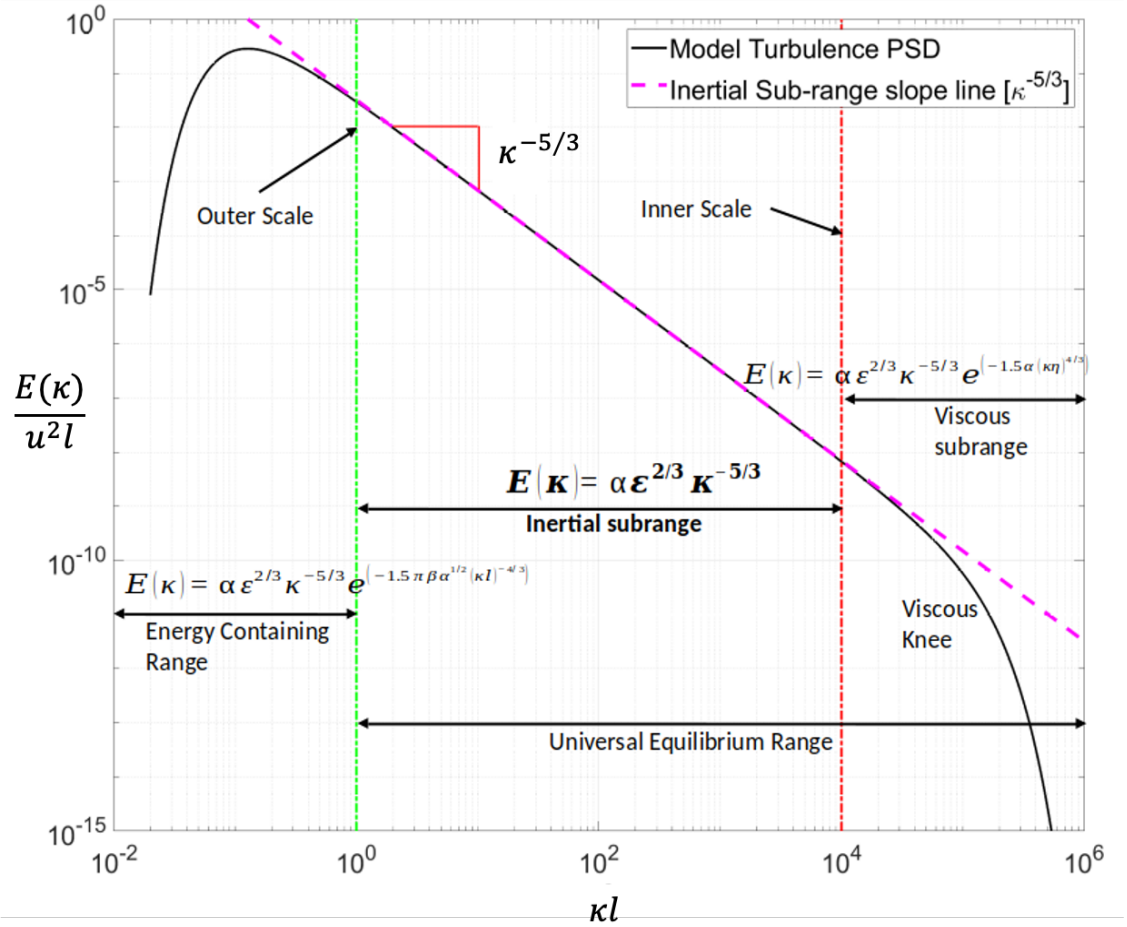

Figure 2.1: The normalized Energy spectrum of three-dimensional, homogeneous, isotropic turbulence is plotted against the normalized wavenumber. The model Energy spectrum shown here is representative of typical atmospheric outer ($\sim 100m$) and inner ($\sim 10mm$) scales.

$E(\kappa)$ within the inertial subrange to depend on only the TKE dissipation rate ϵ. Hence, (ϵ) is indicative of turbulence intensity and is necessary to calculate mixing and transport properties of fluid constituents. Estimation of ϵ relies on capturing, fully or partially, the inertial subrange of the TKE spectrum through measurements of velocity fluctuations. Power spectra of measured velocity fluctuations are examined for a characteristic $\kappa^{-5/3}$ inertial subrange cascade, and spectral data are fit to the model spectrum (as in Figure 2.1) to determine ϵ.

A cylindrical shroud protects the delicate fine-wire turbulence sensing elements from undesirable external factors during flight and when landing on rugged terrain. The protected DH2 HW anemometer was tested for distortion effects in a wind tunnel, by generating synthetic turbulence using a grid at the inlet (see next section). Figure 2.2 compares power spectral density (PSD) of uncalibrated (voltage) HW measurements sampled from the wind tunnel turbulent free stream (top panel) with those from the protected HW (bottom panel) at identical wind tunnel flow velocities ($15m\ s^{-1}$). The free stream HW spectra follow, reasonably well, the inertial subrange slope characteristic expected of turbulent velocity fluctuations, whereas, the protected HW spectra showed noticeable deviation from $f^{-5/3}$ slope starting above $50Hz$

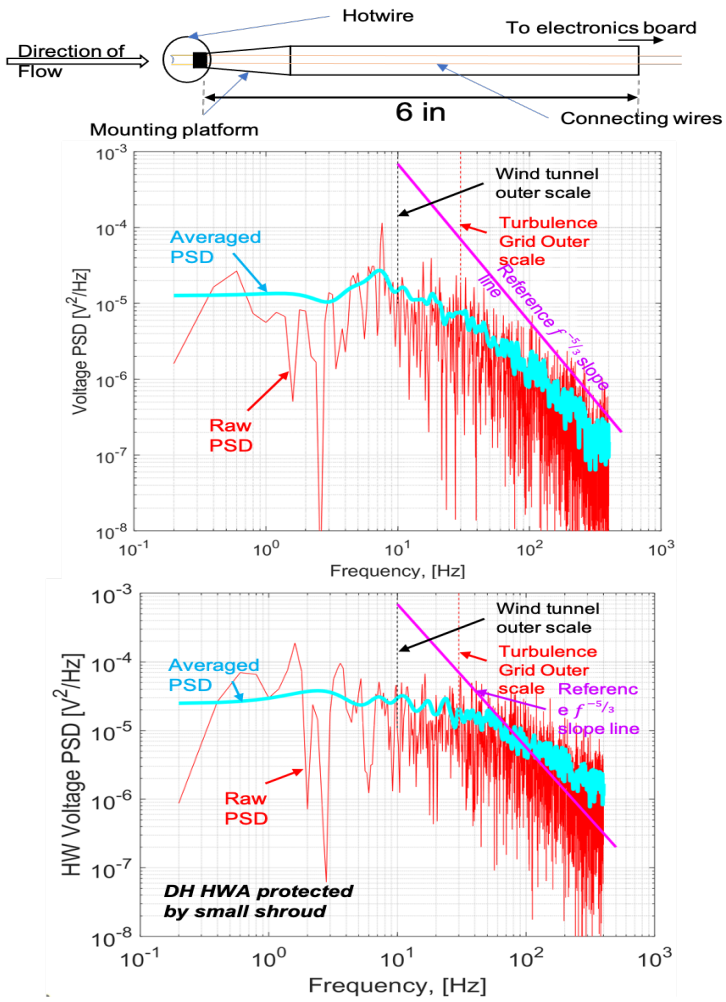

Figure 2.2: PSD of uncalibrated HW (voltage) in the free-stream (top panel) compared with PSD of protected HW (bottom panel) from preliminary wind tunnel tests. The magenta line is a $f^{-5/3}$ depiction of the expected inertial subrange spectral slope.

and had elevated spectral levels overall. Clearly, at the scales of turbulence produced in the wind tunnel, the departure from $f^{-5/3}$ inhibits accurate ϵ estimation.

This was surprising because the scale of the protective obstructions in the flow were so small that the turbulence induced by these was thought to be too small in scale, hence the additional fluctuations too high in frequency, to detect in the spectral data. These preliminary wind tunnel test results confirm such obstructive effects warrant a more detailed study.

Figure 2.3 shows a schematic of the protective elements enclosing the fine-wire sensors. The delicate sensing elements are protected from large debris like rain drops, snow, grass/twigs during landing. The sensing elements are soldered onto a pair of prongs and made to face downstream. Rectangular ($3mm \times 4mm$) shields made of thin copper sheets are soldered onto the upstream prongs as shown in the figure for additional protection from debris entering the cylindrical shroud. Free-stream air flowing into the cylindrical shroud is perturbed by the wake produced by the leading edge of the electronics board, the growing boundary layer inside the shroud, and the wake of the rectangular wire shields. Figure 2.4 visualizes these effects, including the potential obstructive wake effects of the DH2 airframe. The wind tunnel study described in Section 2.3 was conducted to isolate influences of individual perturbation sources on the spectral characteristics of HW turbulence measurements, with the goal of mitigating/minimizing spectral contamina-

tion.

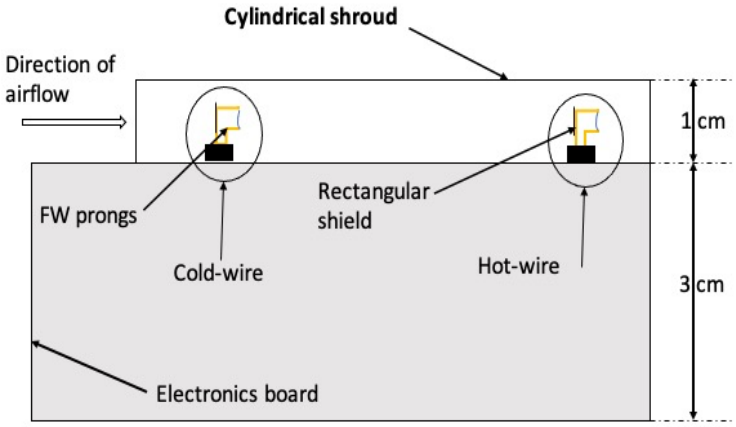

Figure 2.3: Schematic of the original shroud design. Notable features protecting the fine-wire sensing elements include the cylindrical shroud, rectangular shields, and wire prongs.

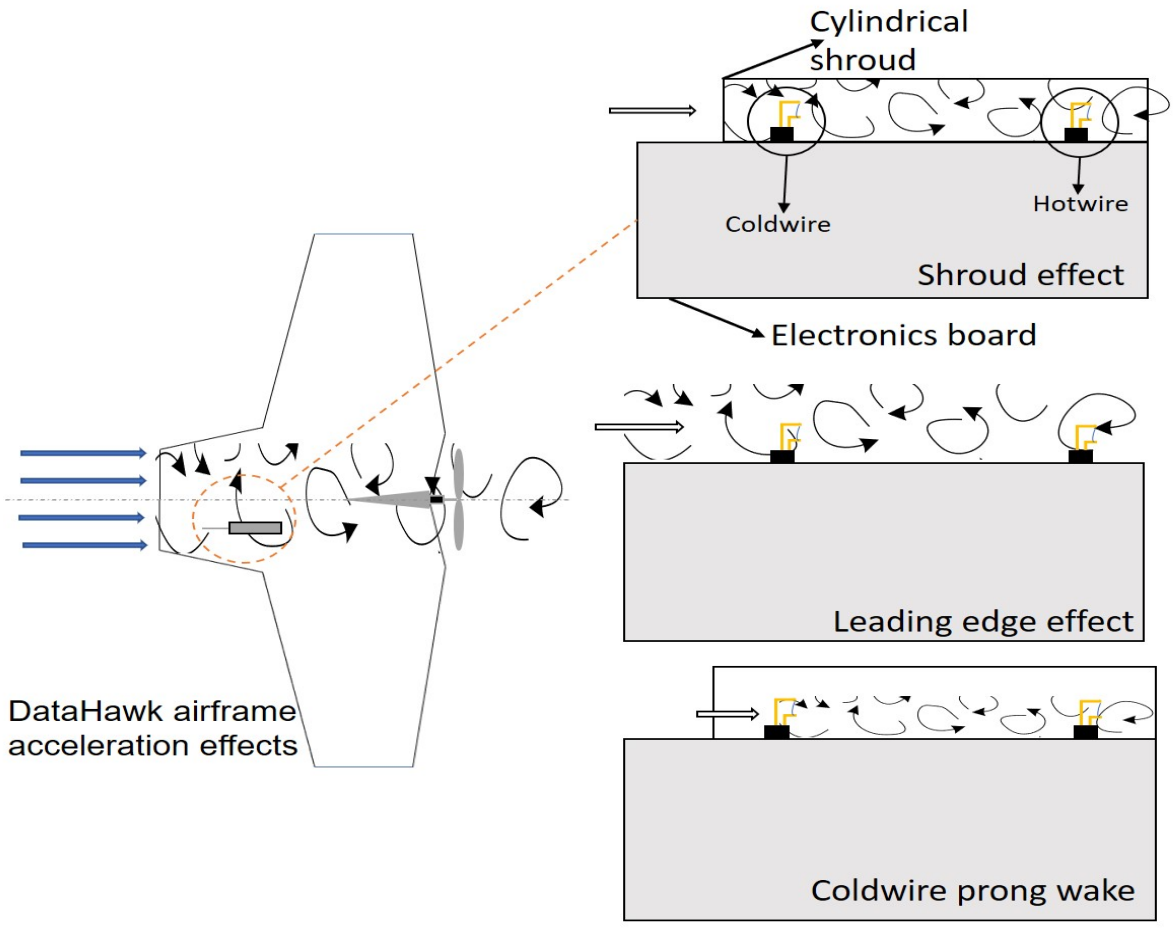

Figure 2.4: Distortion effects from the wake of fine-wire electronics board, cylindrical shroud, wake of rectangular shield, and flow over DH airframe are illustrated.

2.2 Experimental Setup

Tests of protected fine-wire sensors were conducted at the University of Colorado research wind tunnel facility (Farnsworth et al., 2020). The sequence of tests proposed to study various design features of fine-wire protective elements ideally requires steady and repeatable turbulent flow conditions. A grid consisting of 9 smooth cylinders (steel electrical conduit) of 1" diameter and spaced 2.25" apart was installed at the inlet of the wind tunnel test section ($0.5m \times 0.5m \times 3m$ in breadth, height and length). The tunnel was operated to achieve a mean flow velocity of $15m\ s^{-1}$, matching the nominal flight speed of DH2 UAS. Flow around the turbulence grid cylinders attained a Reynolds number of $\sim 25,500$. The resulting wakes produced by the cylinders spread at an angle of 15° and coalesce to produce a homogeneous turbulent flow field downstream of the grid. Figure 2.5 shows the schematic of the experimental setup, with the relative positions of the turbulence generation grid and the sensor test stand. Free stream velocity measured along the test section breadth at a distance of $1.85m$ downstream of the grid (and beyond) was found to show variations $< 10\%$ of the mean flow velocity, indicating sufficient mixing of wakes. A streamlined platform designed to hold either the unprotected or the protected DH2 HW sensor was placed at $2.2m$ downstream in this uniform turbulent flow field. Using dimensional analysis (Tennekes and Lumley, 2011), the outer scale of turbulence generated by the grid was calculated to be $\sim 0.5m$ corresponding to measured frequencies

of $30Hz$. The same experimental setup described above was used for every study described in Section 2.3.

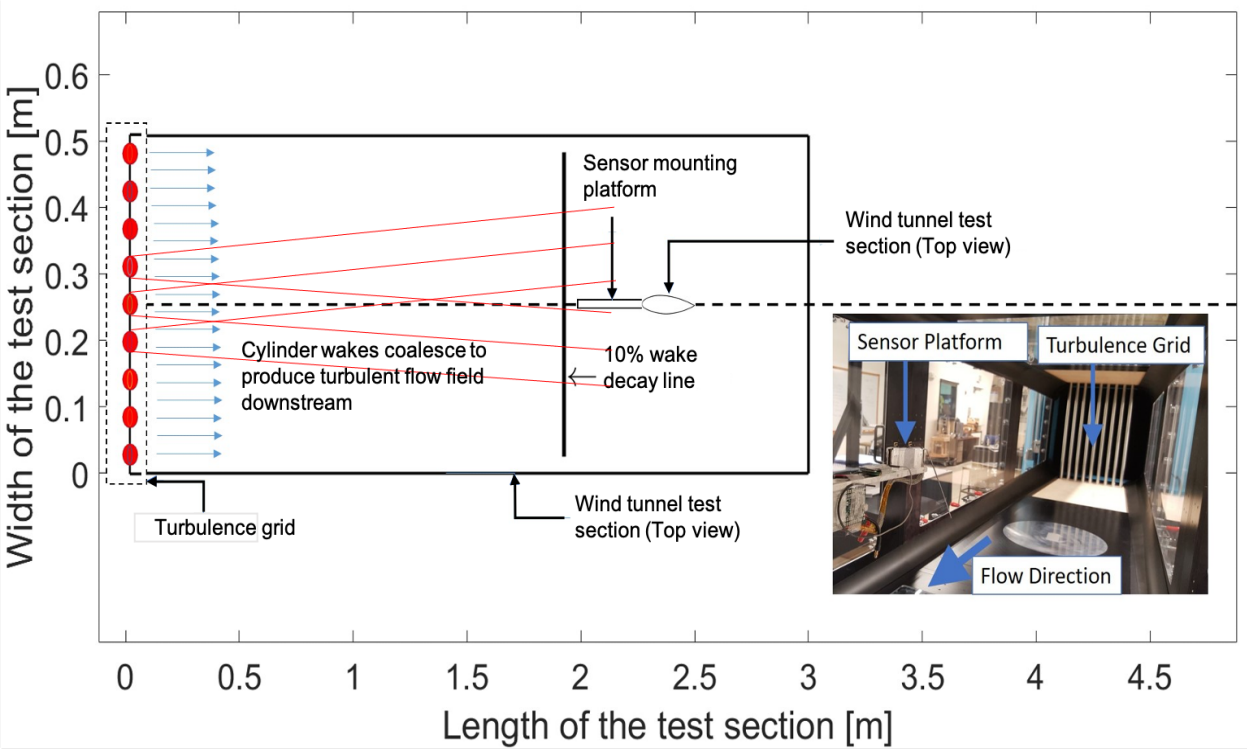

Figure 2.5: Schematic of the experimental setup — Top view of wind tunnel test section. Inset shows an image of the test section taken from the downstream end.

2.3 Results and Discussion

Even small, streamlined UAS can be intrusive measurement platforms. The free-stream air parcels are perturbed as they flow over the DH2 airframe, then over the electronics sensor board before being channeled into the cylindrical shroud, where the fine-wire sensors are located (illustrated in Figure 2.4). The shields protect the fine wires from particles, but also cause small-scale

disruptions in the flow. The HW measurements are also affected by, albeit at very small scales, the wake of the upstream CW prongs. Perturbation from each of these sources, relative to a free-stream measurement at the same location, was characterized and treated individually in a sequence of wind tunnel studies.

The free-stream flow acceleration over the top of the DH2 airframe was found to enhance the mean airspeed, but had negligible impact on the measured turbulence spectrum (not shown). The mean flow acceleration effects at angle of attacks between -5° and 15° were characterized in the wind tunnel and a suitable factor was derived to calibrate the measured mean airspeed as a function of angle of attack.

Next, the wake effect from free stream flow over the electronics board leading edge was isolated by extending the cylindrical shroud beyond the board leading edge, as shown in Figure 2.6. Voltage PSD for the HW in the extended shroud configuration (right panel) shows overall power attenuation above $10Hz$. The spectral slope above $100Hz$ was restored to $f^{-5/3}$, while the signal intensity between 30 and $100Hz$ was found to be attenuated (compare with the top panel of Figure 2.2). These results were identical for shroud extension lengths of 0.25, 0.75 and 1.25" (measured from the board leading edge). Evidently, the turbulent wake effects due to the electronics board were suppressed by extending the shroud beyond the board's leading edge, but the overall intensity of turbulence was reduced by the longer shroud tube.

This may be due to the enhanced frictional effects of a long, small-diameter tube. Due to the strength of this effect, the tube was removed in the next series of tests, so this would not dominate other obstructive effects we wish to understand.

The effects from the wake of upstream CW prongs on the HW were studied next. HW anemometers operate at temperatures well above the local ambient temperature (high overheat ratio), when compared to coldwire (CW) thermometers. The HW sensor on the DH2 is placed behind the CW sensor inside the shroud to prevent the warmer-than-ambient HW wake from contaminating CW temperature measurements. However, the wake produced by the upstream CW prongs could enhance HW spectral power enough to cause difficulties in parameterizing turbulence.

To isolate the effects of the upstream CW prongs from the board wake effect, the CW and the HW prongs were elongated (tripled in length) as shown in Figure 2.7.This elevated the CW and the HW sensors well above the board's wake. The shields were also removed, and the prongs were turned so the sensor wires were upstream of their supporting prongs. This was done to remove these other obstructive effects from the present question. PSDs of the HW placed in the wake of the CW (in the same plane behind the CW) were found to have enhanced power at frequencies above $50Hz$ and to noticeably deviate from the expected inertial subrange slope (see the left panel of Figure 2.7). To verify that the upstream CW is the culprit, this test

was followed by separating the CW and the HW measurement planes by a small angle ($\sim 20°$) to put the HW outside the wake of the CW prongs.

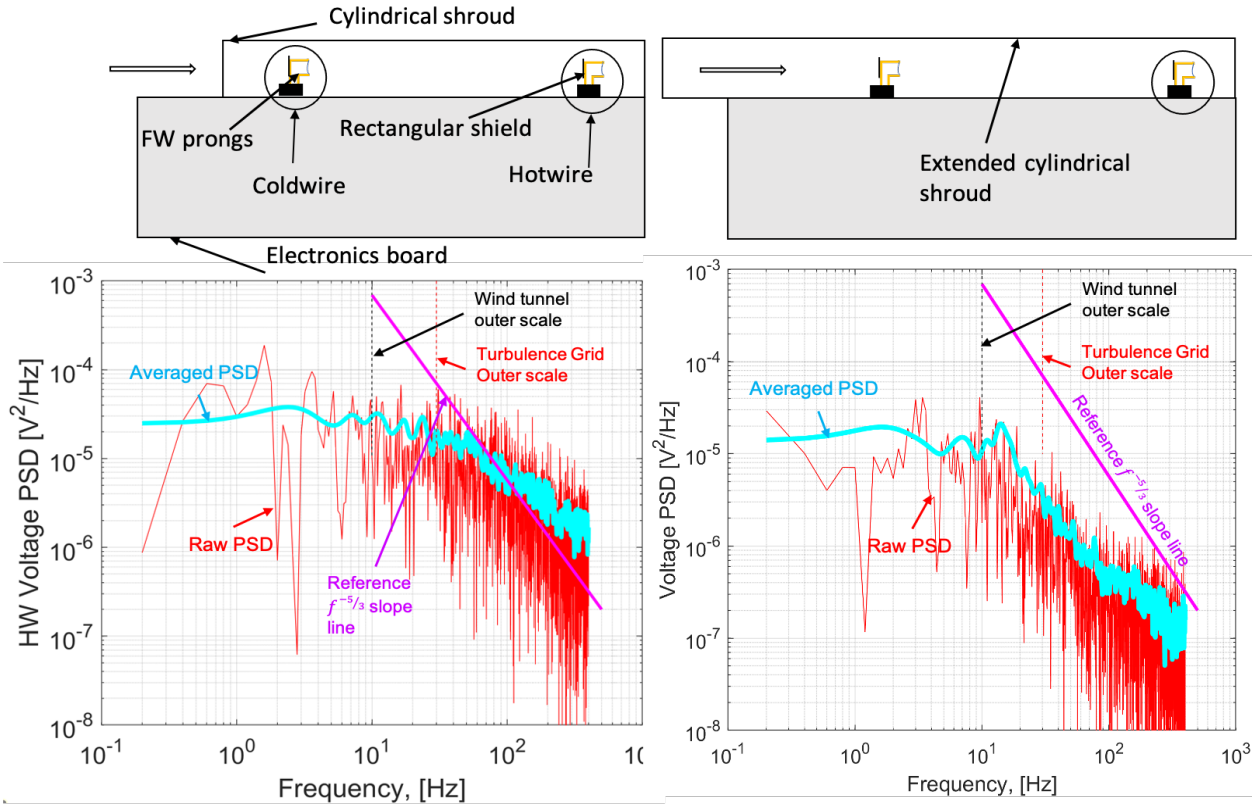

Figure 2.6: Plots comparing sample voltage spectra of HW in nominal DH2 configuration (left) and HW in extended shroud configuration (right). The outer scale for turbulence grid (vertical red line) and the wind tunnel (vertical black line) are marked on the spectra. A $f^{-5/3}$ slope line (magenta) is plotted for reference.

The resulting HW measured spectra (right panel of Figure 2.7) had an improved inertial subrange slope at frequencies above $30Hz$, but enhanced power remained beyond $100Hz$. Clearly, the wake of upstream prongs has a measurable effect, despite their small size, and this arrangement should be avoided. This also calls into question the wisdom of the upstream shields on each sensor wire. These are extremely effective in preventing wire breakage from particles in the flow, but are probably not worth the deleterious effects

they cause in the turbulent spectra. Although an explicit test comparing reversed and shielded wires to a free stream case was not carried out, the upstream CW results were convincing enough to avoid this highly protected arrangement in subsequent tests.

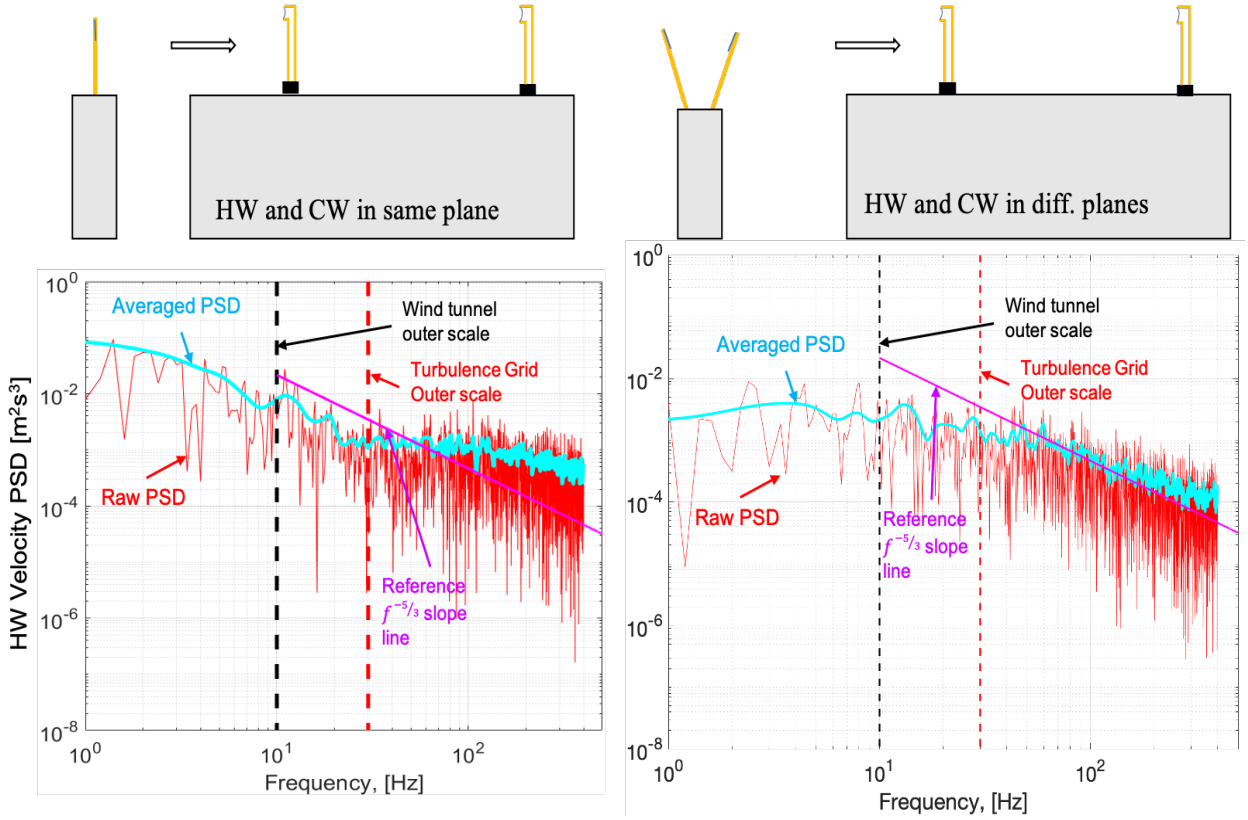

Figure 2.7: Plots comparing sample voltage spectra of HW on tall prongs. (left) The CW and HW prongs are in the same plane. (right) The CW thermometer and HW anemometer prongs are separated by an angle (see side views).

The cylindrical shroud was reintroduced for the final test. A shroud is quite useful in protecting the wires from inadvertent damage by operators while preparing and launching the aircraft, and helps keep large objects (leaves, sticks) from contacting the wires on landing. As discussed in Section 2.1, a shroud is also effective against biases on the coldwire from solar radiation. So,

the question here was: is there a large enough shroud diameter to retain these protections, but reduce the attenuation effects on the turbulence spectrum to an acceptable level?

Tests were conducted where the shroud diameter was increased in steps of $1cm$ to test four configurations, i.e., $1, 2, 3$ and $4cm$ respectively. Figure 2.8 shows velocity spectrum from the HW in a shroud of $3cm$ diameter. The power attenuation between 30 and $100Hz$ observed on the spectrum of the $1cm$ diameter shroud was no longer observed on the spectra of larger diameter shrouds ($> 5cm$). Linear least squares fit slopes for the spectra from this experiment were found to be within $f^{\frac{-5}{3}\pm 0.16}$ ($< 10\%$ slope error). Such a slope deviation error is within the tolerance accepted for ϵ estimation by some authors, e.g. (Wyngaard, 1968). To the extent that the wind tunnel turbulence is representative, re-designing the

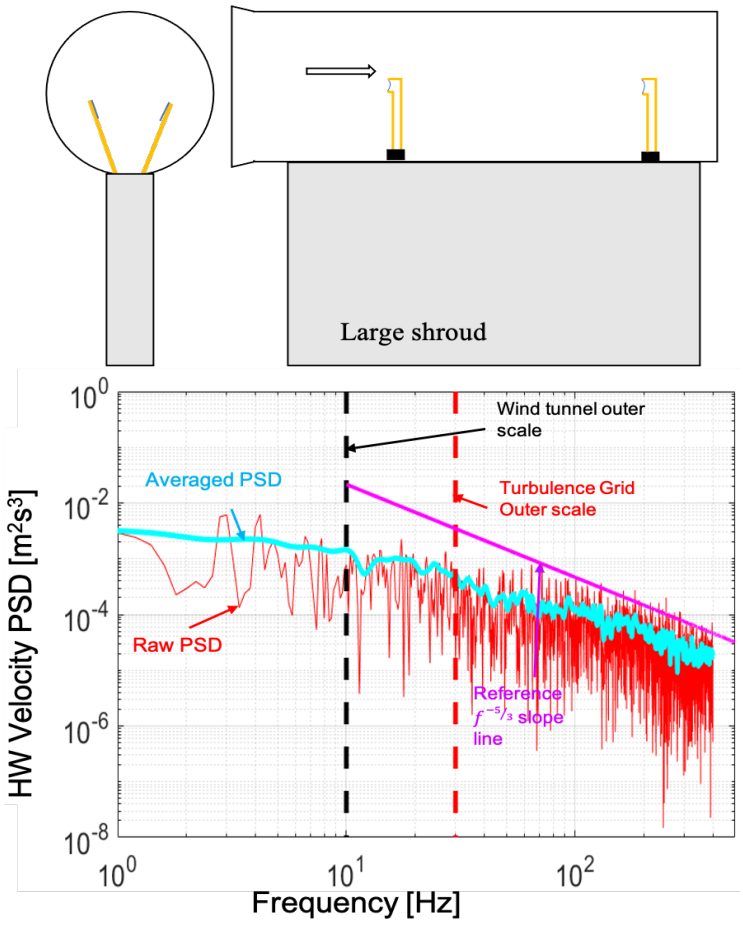

Figure 2.8: Wind tunnel spectral response of a HW sensor protected by a $3cm$ diameter shroud.

DH2 turbulence sensor to conform to the arrangement of Figure 2.8 is suggested by these results.

However, the synthetic turbulence flow field in these studies is composed of a narrow range of spatial scales due to the restricting size of the wind tunnel test section. Atmospheric turbulent flows span a much broader range of scales when compared to the wind tunnel turbulence, and parameterization of turbulence in these flows typically is based on a wider extent of the inertial subrange. This raises the question: are the larger scales of the turbulence spectra affected by the small-scale protections of the fine-wire sensors? This can only be answered outside the wind tunnel. Therefore, the performance of the new prototype protections was evaluated by conducting HW measurements in both free stream and in protected conditions in DH2 flight tests, carried out in the convective boundary layer on a warm summer morning.

2.4 Field Test

The DH2 was equipped with an auxiliary pitot and HW sensors mounted on a platform protruding beyond the DH2 airframe leading edge and into the free-stream flow, as shown in Figure 2.9. The reconfigured DH2 aircraft was flown under nominal convective boundary layer conditions with a flight ceiling of $100m$. DH2 flight data produced ~ 300 spectra for the HW sensors in free-stream and protected configurations. Representative spectra comparing HW in free stream flow and the protected HW are shown in Figure 2.9. The

protected HW PSD (blue line) shows negligibly small attenuation compared to the free stream HW spectrum (red line). The high-frequency noise (above $40Hz$) is suspected to be a remnant of motor vibrations transmitted to the HW on the free stream mount. Several spectra (as in Figure 2.9) were analyzed to build confidence in the redesigned fine-wire sensor configuration for use in estimation of the TKE dissipation rates from the spectral magnitudes in the inertial subrange.

The lessons learned from the above studies can be succinctly summarized by the spectral schematic in 2.10. This shows a section of the PSD from 2.1 representing free stream geophysical turbulence (blue line) cascading down from its outer scale with a normalized wavenumber of about 10. The red line shows the turbulence cascade predicted by the K41 theory applied to a small-scale obstruction in the flow, gener-

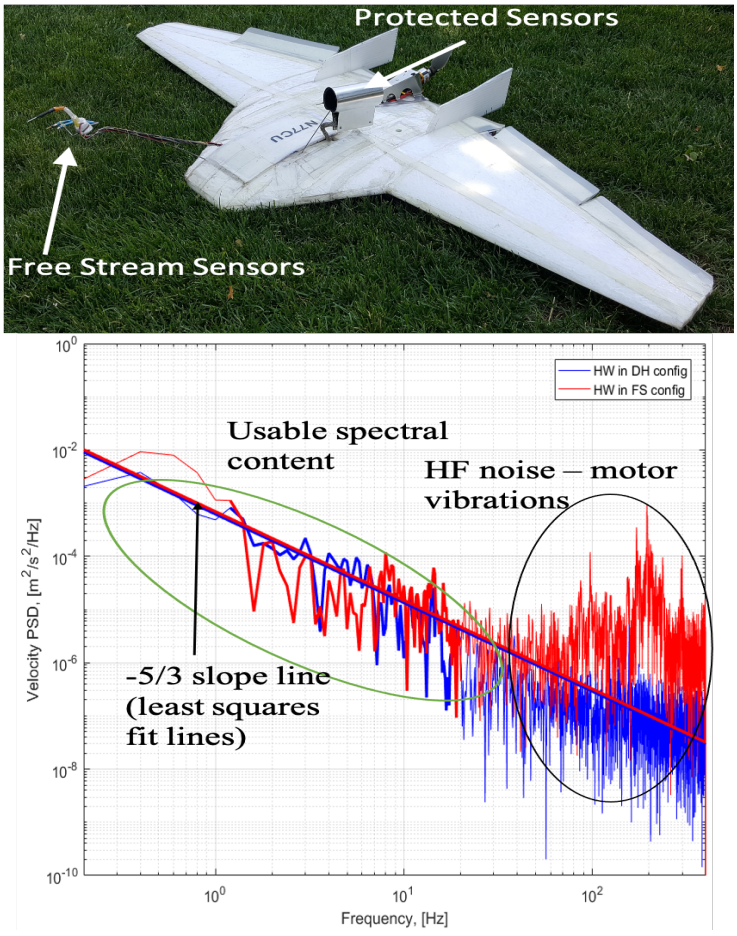

Figure 2.9: Top panel:Instrument setup for the field test of a DH2 equipped with HW and pitot on a mounting platform protruding into the free-stream flow, as well as a protected HW sensor mounted on top of the airframe. Bottom panel: Plot comparing free stream HW PSD to the new prototype protected HW PSD.

ating its own inertial cascade above its (much smaller) outer scale, at a normalized wavenumber of about 10^4, that elevates the measured spectrum (orange line) at and above the sensor Nyquist frequency. This was the expected behavior of small-scale protective obstructions leading to the original design of small protective elements for the sensor wires. However, the wind tunnel measurements produce obstructive spectra more like the purple line, where spectral energy does not fall off at large scales as in the K41 theory. Instead, it remains flat down to scales much larger than the obstruction's outer scale. In turn, this elevates the actual measured turbulence spectrum (green line) at larger scales (lower wavenumbers) than anticipated. This results in a characteristic reduction in the slope of the geophysical turbulence cascade (near the sensor Nyquist frequency in this example), leading to large errors in estimation of ϵ (or C_T^2, since the spectral issues are the same). This would be a significant problem if only data near the Nyquist frequency was used for turbulence parameterization. On the other hand, if spectral intensity at lower wavenumbers in the PSD are available, the geophysical turbulence could still be accurately parameterized by suitably ignoring this high-wavenumber region where obstructive turbulence is significant. Thus, obstructions do not affect geophysical turbulence parameterization if they are suitably small in scale and low in intensity. The above studies have identified protective design modifications that satisfy this guiding principle, provided that spectral curve fitting does not utilize data above about 100Hz. Since most analy-

sis of turbulence that we have undertaken uses time records of 1 second or longer, corresponding to the lowest spectral frequencies of $1Hz$ or smaller, this typically results in 2 decades of uncorrupted spectral data for estimation of turbulence parameters, leading to high-quality parameterization data products.

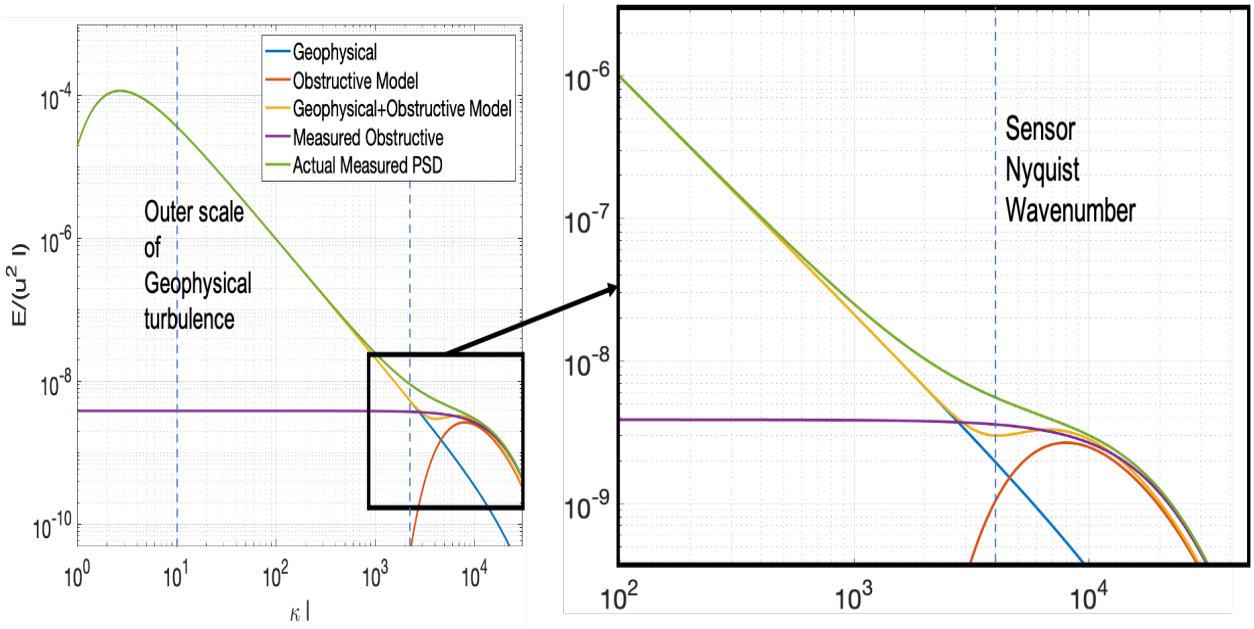

Figure 2.10: Sketch showing the conjecture based on wind tunnel observations of numerous shroud designs.

2.5 Insolation effect on CW temperature

We digress from studying the problems in HW turbulence measurements to briefly discuss the unexpected impacts of the aluminum protective shroud on CW temperature measurements. DH2 temperature measurements from ShUREX2016 and ShUREX2017 field campaigns (Kantha et al., 2017a) contained noticeable periodic artifacts during typical UAS science flights carried

out on helical profiling trajectories. It was conjectured that alternating insolation and shading of the highly thermally conductive metal shroud could be responsible for the periodic artifacts observed in sampled data. This was approximately recreated in ground tests by manual periodic exposure to insolation and shading for $5s$ across a range of solar incidence angles, where a 0° angle has the sun directly in-line with the cylinder axis of the shroud and the wire is directly exposed to the sun, and a 90° angle has the sun normal to the sensor board and the shroud, where no direct illumination of the CW is possible. A $3cm$ shroud was used for this test, so the CW was only directly illuminated for sun angles less than 45°. Figure 2.11 shows raw CW voltage time series from an experiment at 0° solar incidence. The steep rise in voltage at the beginning of each exposure cycle is due to the small CW thermal time constant of $0.5ms$. The underlying slow response is likely due to the heating of the much larger sensor board and metal shroud (a relatively large thermal mass). Applying nominal CW sensitivity of $16^\circ C/V$ suggests temperature swings up to $0.4^\circ C$ for each period are sensed by this exposure.

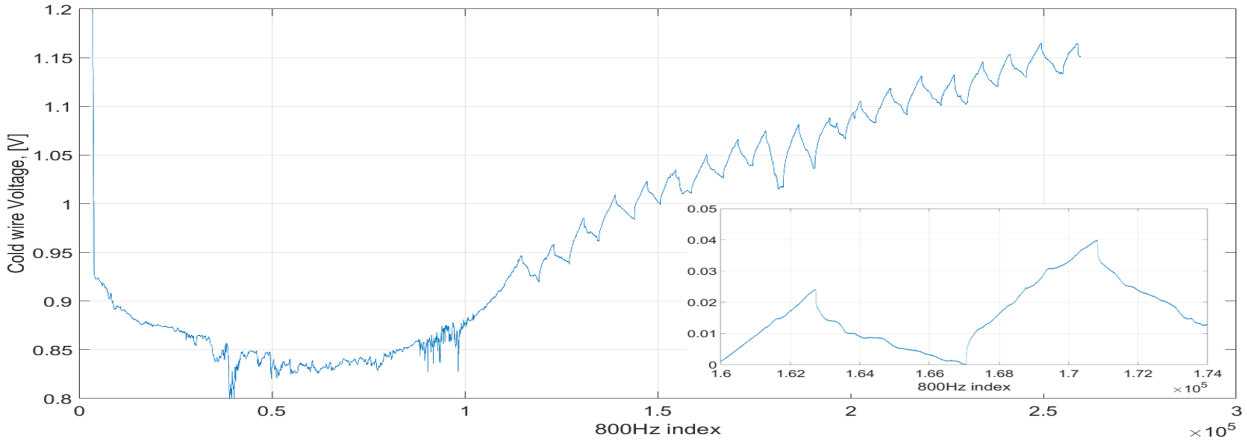

Figure 2.11: Plot showing raw CW voltage timeseries contaminated by repeated heating and cooling for $5s$ periods. Inset shows an enlarged picture of CW data from two $5s$ periods. The voltage axis in the inset is normalized to range between $0V$ and $0.05V$.

Sensor response to insolation was expected to vary smoothly with incidence angles until the $45°$ point where the CW would become shaded. Figures 2.12 and 2.13 show uncalibrated CW voltage for $0° - 80°$ incidence angles in steps to $20°$ that partially confirm this behavior. Insolation response decreases with incidence angle, but the fast blips in the response at the beginning of the insolation pulse remain well past the shading angle. This indicates that the CW is receiving reflected radiation from the inside of the shroud, since the thermal time constant of the metal shroud is much too long to explain these blips. The slower ramps in the response are due to the relatively slow heating of the shroud and/or electronics under the shroud. This indicates that the internal surface of the shroud should be treated to both reduce solar reflections and insulate the CW from thermal radiation coming from the shroud. This would not completely eliminate insolation effects, since there is still a $90°$ cone where the sun would directly illuminate the CW. But these

instances are rare, unless the sun is low on the horizon, and could be easily seen as fast blips in the data that could be marked and removed.

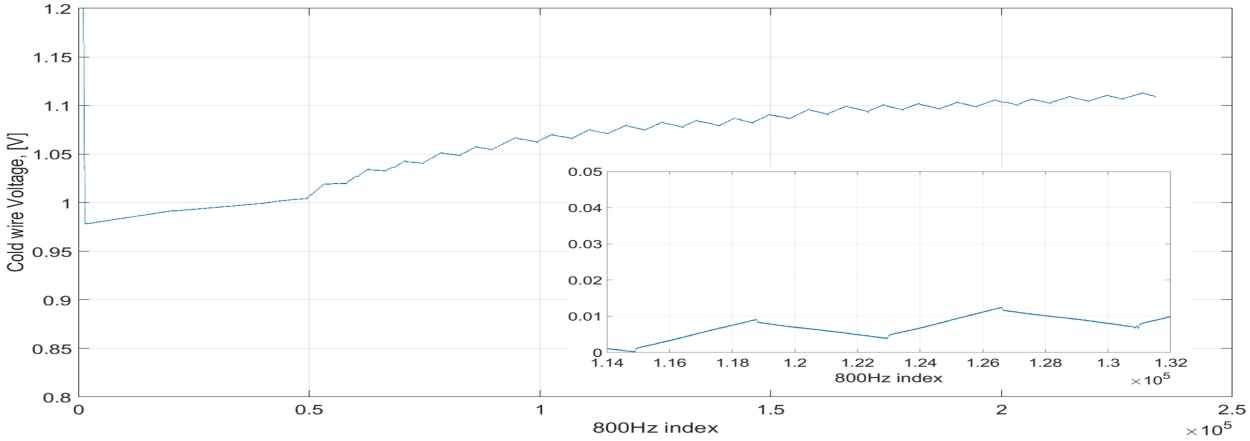

Figure 2.12: Plot showing protected (uninsulated) CW voltage at 0° incidence for 5s.

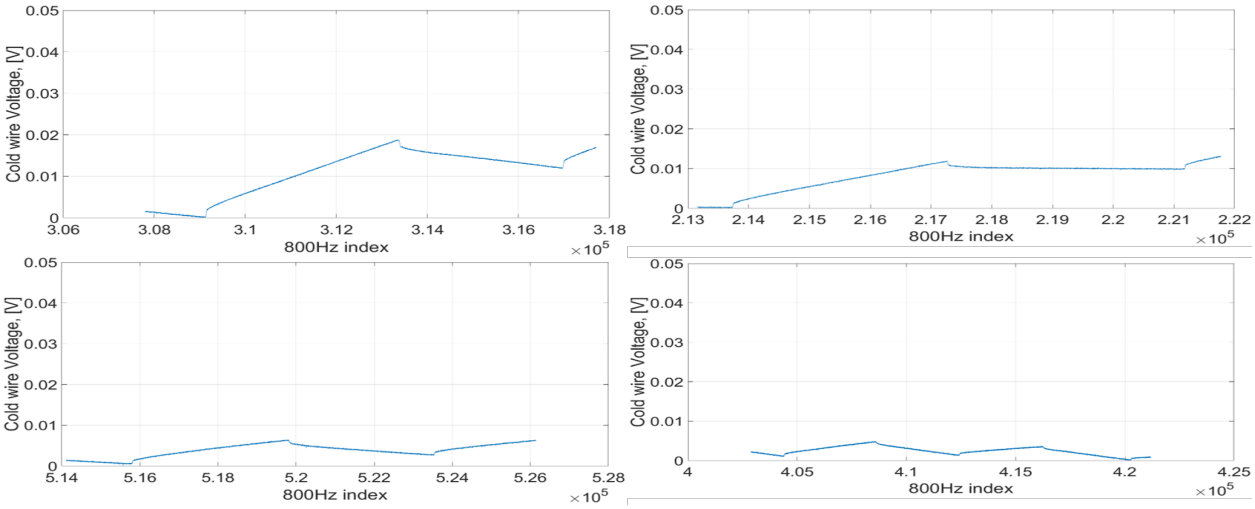

Figure 2.13: Plots showing protected (uninsulated) CW voltage at various incidence angles. Top left panel: 20°; top right panel: 40°; bottom left panel: 60°; bottom right panel: 80°.

A redesigned protective shroud from was lined with 1mm thick adhesive black foam to minimize reflection inside the shroud. On the outside, 1mm thick adhesive white foam cladding was used to insulate the shroud from solar heating. A narrow air gap, 2mm wide, insulated the fine-wire electronics board from direct insolation effects and from indirect heating of the shroud,

due to the passage of air through this gap in flight. Figure 2.14 shows a schematic of the fine-wire electronics board enclosed by the redesigned, insulated protective shroud.

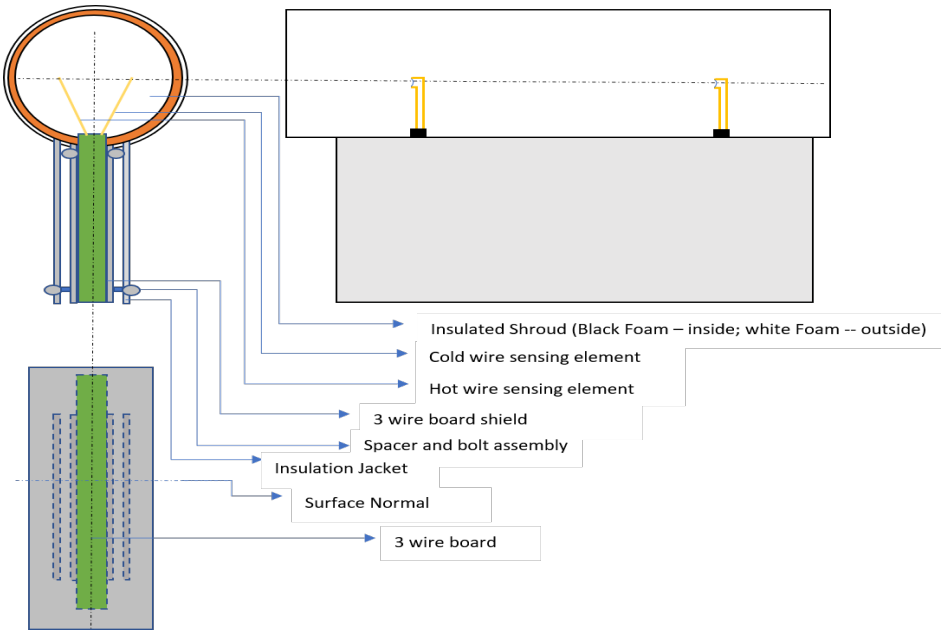

Figure 2.14: Drawing of the redesigned, insulated protective shroud used in the DH2 fine-wire turbulence measurement system.

Figure 2.15 shows the voltage timeseries of insulated CW periodically exposed for $5s$ at 90° incidence angle. The smooth wrinkles in CW voltage are about 5 times smaller than the 80 degree incidence test with the uninsulated shroud. This redesigned, insulated protective shroud was employed on the DH2 UAS during IDEAL campaign.

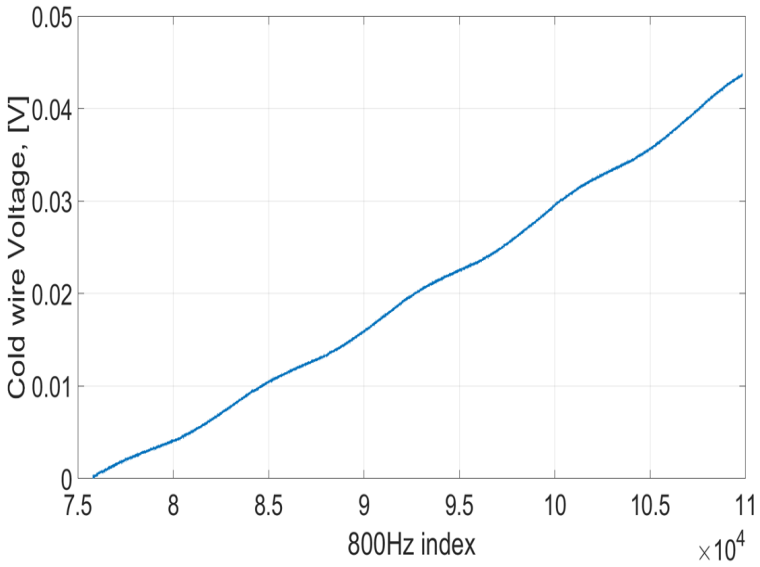

Figure 2.15: Plot showing voltage timeseries of insulated CW exposed periodically for $5s$ at 90° incidence angle.

2.6 Summary

Operational protections for delicate fine-wire turbulence sensors on small UAS were evaluated for their turbulence estimation impact in quantitative wind tunnel testing using synthetic turbulence generated by a grid of cylindrical obstructions in the flow. This data was used to re-design the DH2 turbulence sensor module to retain useful protections, but with acceptable consequences in corruption of spectral data at high wavenumbers. This new design consisted of a larger-diameter shroud, longer fine-wire mounting prongs, elimination of wire shields on the prongs, facing the prongs into the air stream, and tilting the prongs so the CW and HW do not influence each other. The improved design was verified in wind tunnel tests at small turbulence scales and through field tests at geophysical turbulence scales. This helped obtain

more accurate spectra in the inertial subrange, crucial to accurate determination of the TKE dissipation rate ϵ and turbulence temperature structure function parameter C_T^2. The shroud was also modified to greatly reduce the effects of insolation on CW temperature measurements by application of insulation and anti-reflective coatings. This resulted in significant improvements in the quality of the raw data produced by the DH2 turbulence sensor. Chapter 3 will discuss the techniques developed to calibrate this raw data for generation of higher-level data products and scientific analysis of the phenomena observed.

Chapter 3

Sensor Calibration

Chapter 2 described investigations to improve the quality of raw data from the DH2 HW and CW turbulence sensors. The raw data sampled by the custom turbulence sensors is in units of volts, and must be calibrated to physical units before turbulence parameters can be extracted. In this chapter, the calibration procedures for DH2 turbulence sensors are discussed.

The DH2 CW thermometer employs a straightforward calibration procedure. The custom electronics of the CW sensor was designed to yield a constant sensitivity factor of $16°C/V$ throughout its operational range ($-60°C$ to $40°C$). A commercial SHT temperature sensor is mounted on the turbulence sensor board, exposed to the flow inside the shroud, hence is colocated with the CW within about $3cm$. This sensor is factory-calibrated, but is much slower than the CW. The CW is calibrated in post-flight analysis by plotting CW voltage against SHT temperature and computing a best-fit calibration curve to convert the measured cold-wire voltage (in V) to temperature (in K).

Hotwire anemometers are notoriously difficult to calibrate, due to their variation over time, and the need to calibrate against a known velocity reference. This would be exceedingly tedious to do before every DH2 flight. Instead, a novel spectral analysis method to calibrate the DH2 custom hot-wire anemometer is developed in Section 3.2. This employs in-flight pitot airspeed data in a post-flight calibration procedure using its turbulence spectra as a reference for HW spectral calibration. Calibration for the pitot airspeed sensor using a wind tunnel is outlined in Section 3.1. A conventional procedure to derive mean airspeed from raw pitot pressure data is discussed in Section 3.1.1. Pitot-measured airspeed is compared with aircraft velocity in inertial frame (GPS velocity) to check (and correct) for measurement consistency in Section 3.1.2.

3.1 Calibration of Pitot differential pressure sensors

3.1.1 Pitot mean airspeed calibration

Contemporary UAS carry a cluster of high-resolution pressure transducers fitted with custom multi-hole pitot probes (5 or 9 holes) primarily in autopilot GNS sensor suite (Johansen et al., 2015; Velasco-Carrau et al., 2016; Neumann and Bartholmai, 2015; Borup et al., 2016), and for applications in 3D wind and turbulence sensing (Calmer, 2018; Rautenberg et al., 2018, 2019; Alaoui-Sosse et al., 2019). Multi-hole probes are known to employ complex pre-flight wind tunnel calibration procedures and also require elaborate

in-flight calibration (Garman et al., 2006; Calmer, 2018; Calmer et al., 2018). These sophisticated multi-hole pitot probes are also expensive and considerably heavy for use on micro-class UAS like the DH2. A digital pitot differential pressure sensor (TE MS4515) fitted with a miniature custom pitot-static tube records $800Hz$ pressure data on DH2 UAS. The pressure sensor is buried securely inside the airframe and the pitot-tube protrudes from the surface such that the tube inlet comfortably clears the aircraft boundary layer in flight. Mounted behind the aircraft leading edge, the pitot sensor measures the dynamic pressure in airflow accelerated due to the airfoil effect. The bias in pitot pressure measurements due to the flow acceleration around the leading edge of the wing was addressed through wind tunnel calibration experiments.

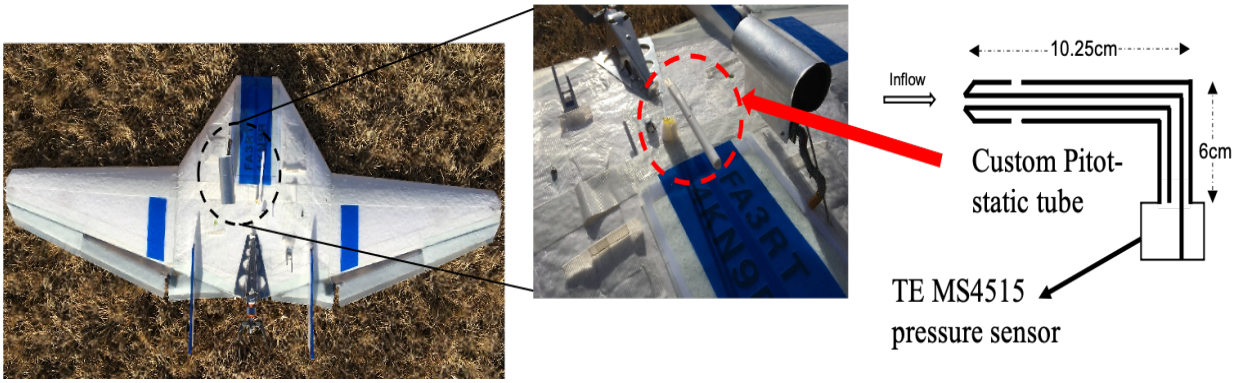

Figure 3.1: Pitot-Static tube and differential pressure sensor mounted on DH2 UAS. The figure also shows a schematic of the custom manufactured pitot-static tube.

A full-scale DH2 aircraft (wings truncated to fit inside the test section) was equipped with pitot and fine-wire turbulence sensors and mounted on a platform able to pivot about the pitch axis inside the wind tunnel test section. Calibration experiments were conducted at three distinct free stream

velocities of $15, 20$ and $25m\ s^{-1}$ for aircraft angle of attack (AOA) between 0° and 15° in steps of 5°. The unitless calibration constant (c) was derived by method of linear regression of $(p_{pit} - p_{ref})$ and $\rho(V_{wt})^2$. Rearranging the pressure-velocity relation gives

$$V_{wt} = \sqrt{\frac{p_{pit} - p_{ref}}{\rho c}}. \tag{3.1}$$

Air density ρ was measured periodically during each experiment, and an average value was used. The pitot sensor recorded the reference pressure p_{ref} at no-flow wind tunnel condition before the start of each experiment. Free stream wind tunnel velocity V_{wt} was obtained from pressure measurements of static rings mounted in the wind tunnel settling chamber. The mean calibration constant (c), obtained from averaging the regression slope obtained from various AOA experiments, was found to be 9.5×10^{-5}.

Biases in pitot-measured mean airspeed resulting from flow accelerations are removed using wind tunnel derived calibration constant (c) in post-flight calibration procedures. Impacts of flow distortions on pitot fluctuation measurements were also extensively studied using spectral analysis of the wind tunnel data, but are outside the scope of this document. These studies revealed negligible power attenuation due to flow acceleration over the vehicle at large scales and no impact on small scales.

3.1.2 Adjusting mean airspeed to median ground speed

The pitot airspeed sensor is an integral element of the autopilot GNS sensor suite. The DH2 autopilot heavily relies on pitot airspeed data for automatic launch, landing, and vector field control to enable a wide variety of measurement strategies. Control laws in the DH2 autopilot are designed to regulate airspeed to track a desired setpoint (nominally $14.5m\ s^{-1}$) in flight. Measured airspeed for circular flight trajectories follows the mid-point of GPS speed variation measured over every circle.

Figure 3.2 shows typical variation of the aircraft GPS horizontal speed (blue line) and the calibrated pitot airspeed from a DH2 flight segment (six circular periods long). The periodic excursions in pitot airspeed coincide with maximum GPS (ground) speed, and are due to the high bank angle required to stay on the circular ground path at high ground speed. The aircraft loses lift at high bank angles and tends to dip down in altitude, causing a local airspeed increase. In case of constant horizontal winds, the artifacts are observed at the same aircraft bearing angle on every circle. The pitot airspeed is also typically offset from the mid-point ground speed. The periodic artifacts and offsets in calibrated pitot airspeed manifest as systematic biases in the estimated wind vector, and also affect the TKE dissipation rate determined from airspeed spectra. Therefore, it is necessary to mitigate the periodic artifacts in the pitot-measured airspeed.

The offset and periodic excursions in calibrated pitot airspeed are treated

in post-flight data processing. For simplicity, the processing algorithm is explained through an example using helical sampling strategy. As a necessary pre-processing step, all the participating data arrays (GPS speed, airspeed, bearing angle etc.) are filtered and re-sampled to a common cadence, say, $10Hz$. Using bearing angle estimates as the reference, the data arrays are divided into segments spanning one circle each. The airspeed correction algorithm operates on each of these data segments separately.

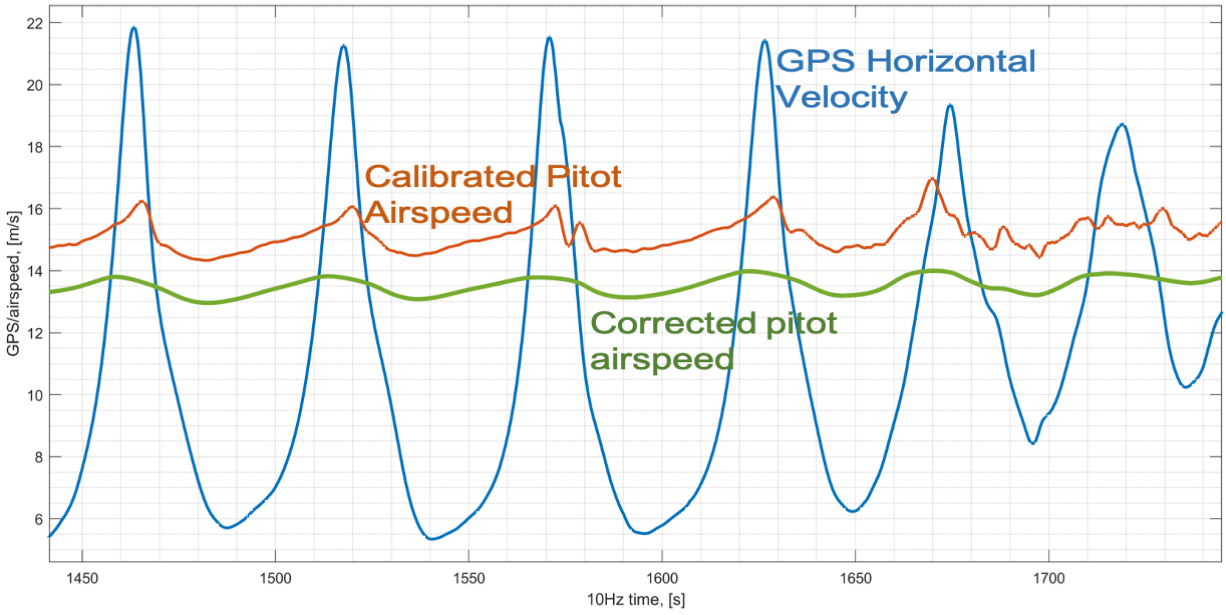

Figure 3.2: Plot showing aircraft ground speed/ GPS horizontal speed (blue), calibrated pitot airspeed (red), and corrected pitot airspeed (green). Note that the GPS speed (sampled at $5Hz$), and pitot airspeed (sampled at $800Hz$) are resampled at $10Hz$ to simplify data processing.

Periodic excursions in calibrated airspeed coincide with the crests of aircraft ground speed data (see Figure 3.2). These excursions are identified using apex ground speeds, and the contaminated data segments (usually a few seconds long) are replaced by median filtered (smoothed) airspeed data of equal duration. The modified airspeed data (v_{as}), now free of excursions,

is further treated using correction factors to remove offsets.

A correction factor (γ_i where $i = 1, 2, 3...n$ periods/circles) is calculated using the mid-point of aircraft ground speed (β_i) and mean airspeed (α_i) over each circle (or period). This is given by

$$\gamma_i = \beta_i - \alpha_i. \tag{3.2}$$

The corrected airspeed v_{corr} is calculated by combining v_{as} and spline interpolated correction factor γ using Equation 3.3. This is shown in Figure 3.2.

$$v_{corr} = v_{as} + \gamma. \tag{3.3}$$

This algorithm is used to obtain corrected airspeed at $10Hz$ and $800Hz$ for use in various analysis procedures described in Chapters 4 and 5.

3.2 Hotwire Calibration

HW anemometers operate on the principle of convective heat transfer. The delicate sensing element, typically $3 - 5\mu m$ in diameter and $1 - 2mm$ in length, are made of tungsten or platinum alloy intercepts the fluid flow to exchange heat through forced convection. The HW sensing element is made to be an element of the Wheatstone bridge circuit and excited by a power source to maintain either a constant temperature (CT anemometer — CTA) or a constant current (CCA). Ignoring the minuscule losses due to conduction and radiation, the flow velocity is inferred by equating the power supplied

to the sensing element (I^2R_w) and heat lost to the flow (Q_{fc}) through forced convection. Thus,

$$I^2R_w = Q_{fc} = hA_s(T_w - T_f) \tag{3.4}$$

where R_w is the HW resistance at wire temperature T_w, h is the heat transfer co-efficient, A_s the HW surface area and T_f the fluid temperature. Empirical models relating the convective heat-transfer coefficient (h) and the fluid velocity (v) are used to infer the flow velocity. HW calibration is conducted in wind tunnels, preferably, shortly before the experiments due to the drifting tendency of HW calibration factors. Furthermore, the calibration factors are non-linear, and unique to each sensing element and electronics.

A typical DH2 campaign utilizes up to 100 HW shipped well in advance to the field. The standard wind tunnel-based HW calibration procedures are tedious and in-efficient to frequently calibrate abundant sensors in advance. Therefore, a reliable post-flight calibration algorithm was developed to efficiently process HW-sampled data.

A novel algorithm applying spectral analysis to high-resolution airspeed data obtained by the co-located pitot sensor (see Section 3.1) was developed to calibrate the HW fluctuation measurements (ignoring mean airspeed measurements of HW). The calibration principle is easily visualized from Figure 3.3. The PSD of measured pitot airspeed $\hat{S}_p(f)$ and the corresponding uncalibrated HW voltage $\hat{S}_v(f)$ calculated using $5s$ data segments for a representative calibration sample are shown in the figure. Linear least squares

regression, constrained to $f^{-5/3}$ slope, is performed to obtain fit levels p and h for pitot velocity and uncalibrated HW voltage spectra, respectively. The fit levels p (in units of $[m^2 s^{-1}]$) and h (in units of $V^2 s^{-1}$) are compared to recover an offset c (in units of $[(m^2/s^2)/V^2]$) defined by

$$c = log_{10}(p) - log_{10}(h). \tag{3.5}$$

This calibration offset c is applied to uncalibrated HW voltage PSD to obtain the calibrated HW velocity PSD $\hat{S}_{hw}(f)$ using Equation 3.6. This is illustrated by the red line in Figure 3.3.

$$\hat{S}_{hw}(f) = \hat{S}_v(f) + c. \tag{3.6}$$

HW calibration is performed periodically throughout the measured data. This is explained using a hypothetical data record (of pitot airspeed and HW voltage) of $3600s$ long. PSD of pitot airspeed $\hat{S}_p(f)$ and HW voltage $\hat{S}_v(h)$ calculated using $5s$ segments of the time series results in 720 spectra each with corresponding spectral fit levels p and h respectively. If HW calibration is conducted every $60s$, the algorithm segments the time series of fit levels p and h into $p_{i,m}$ and $h_{i,m}$ where $i = 1, 2, 3, ...60$ is the number of times HW calibration is conducted and $m = 1, 2, 3, 4, 5$ are the number of spectral fit levels 'scanned' during each calibration cycle. From each calibration cycle i, the fit level with the smallest fit standard deviation p_{i,m^*} (best $f^{-5/3}$ fitting spectrum out of $m = 1, 2, 3, 4, 5$) is used to obtain a series of calibration fac-

tors c_i (Equation 3.5). Figure 3.4 shows a series of 51 HW calibration factors c_i calculated for a representative DH2 flight data set from IDEAL campaign. The mean calibration factor was found to be unique to each HW sensor wire, with the standard deviation $< 0.5(m^2/s^2)/V^2$ (scattered around $2.15 m^2/V^2$ here).

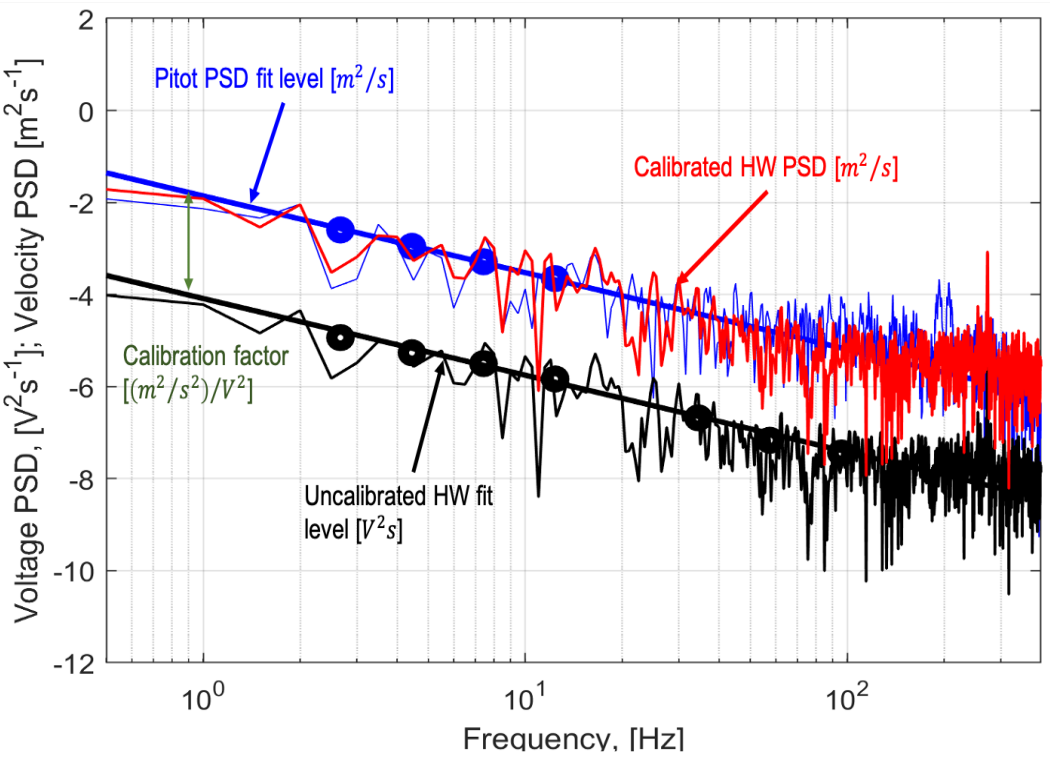

Figure 3.3: Plot showing PSD of measured airspeed (thin blue line) and the corresponding uncalibrated HW voltage (thin black line). Least squares fit calculated using the dots (blue and black) results in fit levels p and h for pitot and HW respectively (thick blue and black lines).

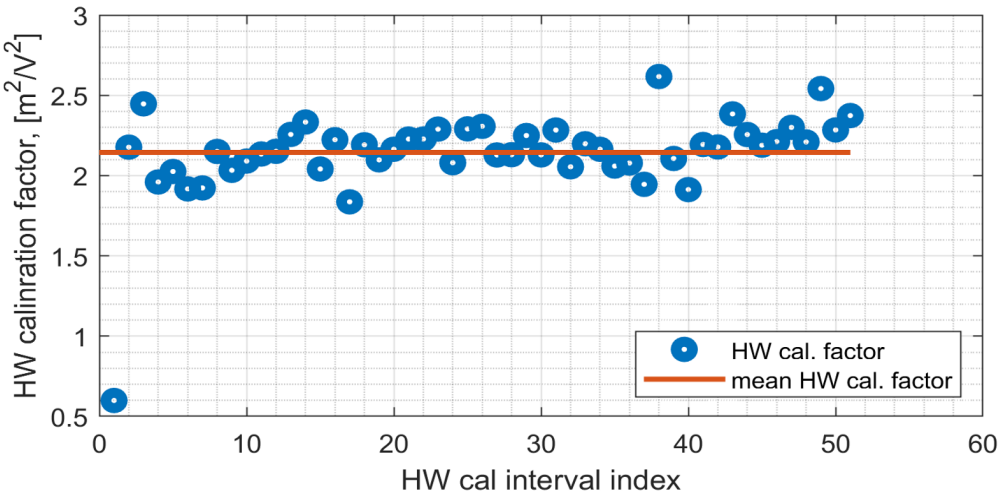

Figure 3.4: Plot showing HW calibration factors c_i (blue dots) along with the average value $\bar{c}$ (orange line) for an arbitrarily chosen data set from IDEAL field campaign.

Figure 3.5 shows a scatter plot of HW and pitot derived ϵ (on $\log_{10}$ scale) highlighting the pitot data points used in HW calibration (red stars). The calibration points span a wide range of ϵ values ($\sim 3.5 decades$) indicating that the automated algorithm calibrates HW fluctuations over a wide range of turbulence intensities. The linear fit through all the data points (discounting the outliers) in figure 3.5 suggests that the co-located HW and

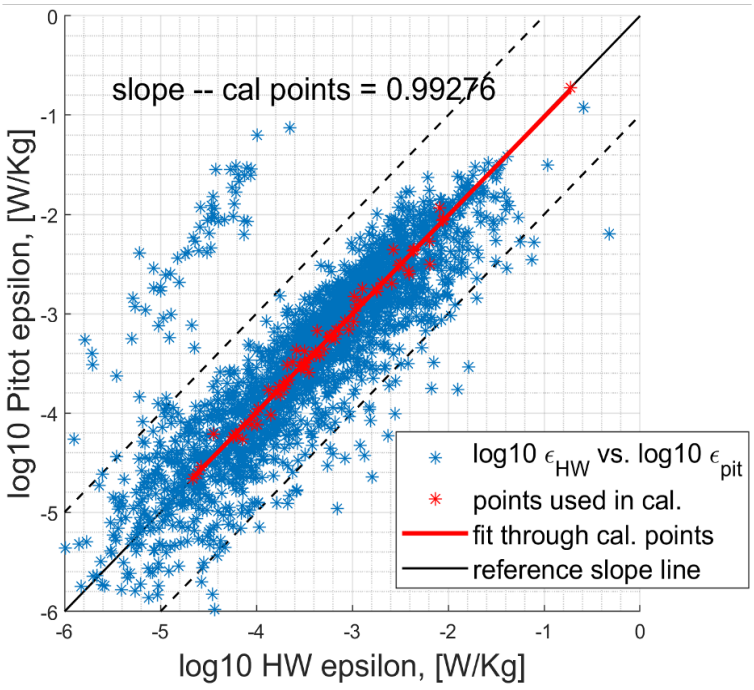

Figure 3.5: Plot showing correlation between HW and pitot derived ϵ (blue stars). The pitot data points used in HW calibration are highlighted (red stars) and a linear fit line is shown (red line).

pitot sensors measure turbulence similarly, except for a constant scale factor. Further, figure 3.6 shows the distributions of pitot and HW derived ϵ along with the distributions of standard deviation. The distributions of pitot and HW derived ϵ show remarkable agreement with each other.

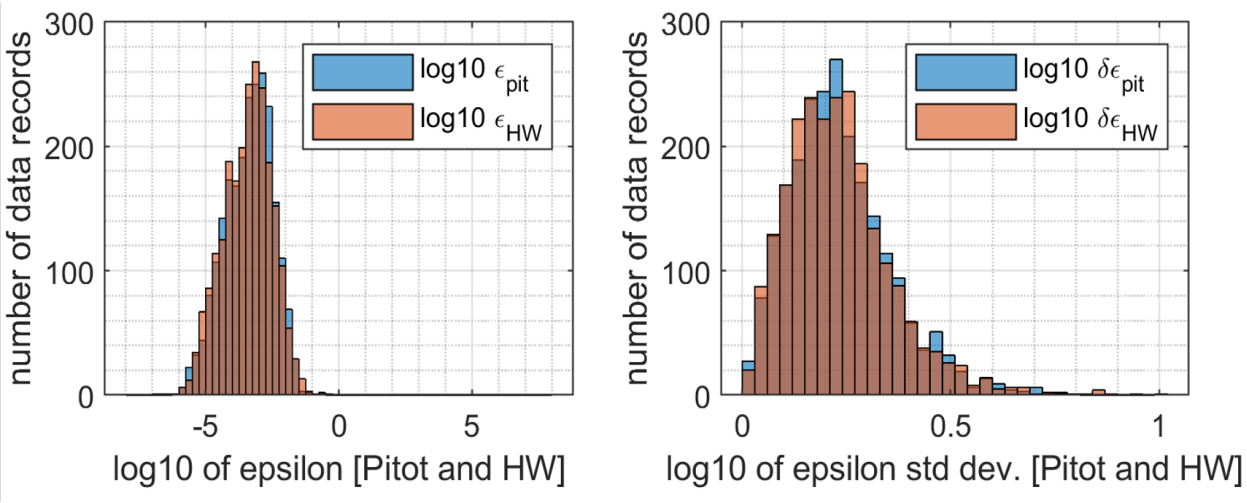

Figure 3.6: Plot showing distributions of pitot and HW derived ϵ_{pit} and ϵ_{HW} (left tile). The right tile shows distributions of ϵ standard deviations ($\delta\epsilon$) which represents the estimation error.

The novel HW calibration technique, using spectral analysis of calibrated pitot PSD described in this chapter, was successfully applied to all DH2 UAS HW datasets from the IDEAL, and MOSAiC field campaigns (Doddi et al., 2021). The calibration procedure was exclusively developed to be conducted post-flight, and that enabled calibration and turbulence analysis of DH1/DH2 HW data from observation campaigns conducted in the past. The calibration algorithm has also been applied to HW measurements from ShUREX2016, ShUREX2017, ISARRA, and POPEYE campaigns (Kantha et al., 2017a,b; Luce et al., 2018b,a, 2019; De Boer et al., 2016; de Boer et al., 2019).

3.3 Part I: Conclusions

In part I we set out to address the problems in UAS turbulence sensing. Chapter 1 focused on mitigating the contaminants in DH2 UAS raw fine-wire turbulence measurements. The protective shroud introduced to shield the delicate fine-wire sensing elements from various environmental factors was found to corrupt the power in the inertial subrange of HW-measured spectra. Subsequently, the protective shroud was redesigned using extensive wind tunnel studies to mitigate the spectral aberration due to shroud obstructive effects. Field tests described in Chapter 2 resulted in protected HW (and CW) sensors that demonstrated the ability to accurately measure a decade or more (in frequency) of the atmospheric turbulence inertial subrange.

Chapter 3 tackled the challenges in simplifying calibration procedures for raw DH2 turbulence data. First, the mean airspeed information was extracted from pitot differential pressure sensor data. The inferred mean airspeed was checked for consistency with flight dynamics data, and the airspeed fluctuations were tested for biases resulting from apparent flow accelerations due to flow over the DH2 airframe (study not discussed in this document). A novel procedure for calibrating HW sensors using spectral analysis of pitot and HW sensors was developed. Chapters 4 and 5 (Part II) will describe the estimation procedures to derive TKE dissipation rate, turbulence structure function parameter, and horizontal wind components for scientific analysis of atmospheric turbulence using calibrated pitot, HW and CW data.

Part II

UAS data processing

Chapter 4

Turbulence Parameterization

4.1 Introduction

Turbulence is ubiquitous in the atmosphere. Numerous experiments employing different combinations of remote sensing and in-situ sensors have been conducted to support analytic and numerical studies of turbulent atmospheric phenomena. UAS applications in meteorology have made accessible the regions of free atmosphere that were previously either inaccessible or uneconomical for most traditional in-stu observation platforms. Despite their measurement dexterity and range, the UAS have seldom been exclusively used for targeted observations of atmospheric turbulence (Witte et al., 2016, 2017; Canter, 2019).

However, numerous in-situ platforms including UAS have demonstrated the ability to measure turbulence (Coulman, 1973; Alaoui-Sosse et al., 2019; Theuerkauf et al., 2011; Wildmann et al., 2014b; Bäserud et al., 2016; Balsley, 2008; Dehghan et al., 2014; Balsley et al., 1999; Witte et al., 2016) predom-

inantly using 3D turbulent wind estimates from multi-hole probe data. The scope of these studies was mostly limited to establishing a proof-of-concept for turbulence measurements. Balsley et al. (2018b) present a robust method to derive C_T^2 from high-resolution fine-wire measurements of temperature using tethered kite/blimp data. Frehlich et al. (2003) and Luce et al. (2019) describe spectral estimation methods to derive ϵ from UAS-measured pitot airspeed data. The spectral estimation method described in Section 4.3 uses the same empirical atmospheric turbulence model used by Frehlich et al. (2003) and Luce et al. (2019) to derive ϵ from DH2 UAS measurements.

The TKE dissipation rate ϵ and temperature structure function parameter C_T^2 are two fundamental quantities that characterize mechanical and thermal turbulence intensity. Chapter 4 uses high-resolution pitot, HW, and CW calibrated sensor data with the objective to derive these representative parameters of atmospheric turbulence.

4.2 Turbulence Spectral Analysis: Theory

Laboratory experiments on turbulence using wind tunnels commonly employ HW anemometry and PIV techniques (Saarenrinne and Piirto, 2000; Witte et al., 2016, 2017). ϵ in these experiments is calculated by

$$\epsilon = \nu \frac{\partial u_j}{\partial x_i} \left(\frac{\partial u_i}{\partial x_j} + \frac{\partial u_j}{\partial x_i} \right), \tag{4.1}$$

where ν is the kinematic viscosity, u_i are the components of velocity along $i, j = 1, 2, 3$ representing the three spatial dimensions x_i (Einstein summation convention is invoked). Estimating ϵ using this method requires mean and fluctuation measurements along all three spatial axes. Typically, only longitudinal velocity measurements are made using single channel HWA. Assuming homogeneity and isotropy of turbulence structures at small scales, Equation 4.1 simplifies to

$$\epsilon = \nu \left(\frac{\partial u_1}{\partial x_2} \right)^2, \tag{4.2}$$

where u_1 is the longitudinal velocity component and x_2 is the transverse direction. The instantaneous method results in noisy ϵ estimates and requires several repeatable measurements to obtain a distribution that provides suitably averaged ϵ estimates. On the other hand, spectrum-based methods provide confident estimates of spatially (or temporally) averaged ϵ with substantially less noise. UAS measurements are conducted on complex flight trajectories and seldom provide independent measurements in longitudinal and transverse flow directions. This renders the instantaneous method unsuitable for UAS-sampled data. Therefore, UAS turbulence data are subjected to spectral analysis.

4.2.1 One and three-dimensional turbulence energy spectra

UAS measurements of turbulent velocity (or temperature) are made along a trajectory in a moving fluid as a function of time. Measurements of this kind

generate a random function of either position or time. Assuming that the function is homogeneous or stationary, the spectrum can be computed using auto correlation. The resulting spectra, produced by measurements in one dimension, are called one-dimensional spectra.

Turbulence is an unsteady 3D flow phenomena. One dimensional spectra obtained in a 3D flow field suffers from aliasing, i.e., data at wavenumber κ contains contributions from components of all wavenumbers. Aliasing problems are mitigated by conducting measurements along all three directions. The 3D Fourier transform of the resulting correlation produces a spectrum that is a function of vector wavenumber $\boldsymbol{\kappa}$ (or κ_i). The 3D energy spectrum eliminates aliasing at the cost of complexity, which makes it less useful. Instead, the directional information is ingested by integrating the spectrum over spherical shells of radii mod $\boldsymbol{\kappa}$ centered around the origin of wavenumber space. The resulting spectrum, a function of scalar wavenumber magnitude (κ), is called 3D turbulence spectrum.

The equilibrium theory of turbulence (Kolmogorov, 1962) describes the universal behavior of 3D turbulent energy spectrum $E(\kappa)$. The 3D energy spectrum is expressed in terms of spectrum tensor, ϕ_{ii} which is the Fourier transform of velocity correlation tensor $[R_{ij}(\boldsymbol{r}) = \overline{u_i(\boldsymbol{x},t)u_j(\boldsymbol{x}+\boldsymbol{r},t)}]$ (function of vector separation $\boldsymbol{r}$). The energy spectrum of turbulence is given by

$$E(\kappa) = \frac{1}{2} \oiint \phi_{ii}(\boldsymbol{\kappa})\, d\sigma, \tag{4.3}$$

where $d\sigma$ is the surface element of the spherical shell. Typical measurements of atmospheric turbulence are made using 1D sensors sampling fluctuations of longitudinal or transverse flow velocity. The corresponding 1D longitudinal and transverse spectrum, F_{11} and F_{22}, are the Fourier transforms of R_{11} and R_{22}, respectively. Batchelor derived the relationships between F_{11}, F_{22} and $E(\kappa)$ for isotropic turbulence as

$$E(\kappa) = (\kappa)^3 \frac{d}{d\kappa}\left(\frac{1}{\kappa}\frac{dF_{11}}{d\kappa}\right), \tag{4.4}$$

$$\frac{d}{d\kappa_1}F_{22}(\kappa_1) = -\frac{\kappa_1}{2}\frac{d^2}{d(\kappa_1)^2}F_{11}(\kappa_1). \tag{4.5}$$

Kolmogorov (Kolmogorov, 1962) proposed that the energy spectrum of turbulence scales as $E(\kappa)\alpha\epsilon^{2/3}\kappa^{-5/3}$ in the inertial subrange of turbulence spectrum. Equations 4.4 and 4.5 suggest that F_{11} and F_{22} also follow $\kappa^{-5/3}$ if $E(\kappa)$ goes as $\kappa^{-5/3}$.

Turbulence measurements using towers, masts, and other variants of fixed-weathervaning sensors commonly assume longitudinal spectrum (F_{11}). The lightweight airframe of the DH2 UAS weathervanes into the relative wind during flight and measures turbulence on slant-paths. Therefore, assuming a longitudinal spectral model (F_{11}) for all DH2 turbulence measurements is warranted. Weiss (1961) and Frehlich et al. (2003) recommend using an empirical spectral model for F_{11} (represented by $S_u(f)$) that best characterizes turbulence in the stratified free atmosphere. Assuming the Taylor frozen turbulence hypothesis, the model 1D longitudinal spectrum as a function of

frequency is given by

$$S_u(f) = 0.55\epsilon^{2/3}\left(\frac{\overline{u}}{2\pi}\right)^{2/3} f^{-5/3}, \tag{4.6}$$

where $\overline{u}$ is the mean airspeed (corrected airspeed from Equation 3.3) taken over the duration of time series. ϵ is derived from the measured spectrum $\hat{S}_u(f)$ (Discrete Fourier Transforms - DFT), which is expected to exhibit ($f^{-5/3}$) characteristic in a wide range of scales described by

$$\hat{S}_u(f) = \beta f^{-5/3}. \tag{4.7}$$

Linear Least Squares (LLS) regression constrained to $f^{-5/3}$ is performed on the measured spectrum $\hat{S}_u(f)$ to obtain the fit level β. Combining Equations 4.6 and 4.7 gives

$$\epsilon = \frac{2\pi}{\overline{u}}\left(\frac{\beta}{0.55}\right)^{3/2}. \tag{4.8}$$

Turbulence structure function parameter C_T^2 is also calculated using identical analysis scheme as described by

$$S_T(f) \approx 0.25C_T^2\left(\frac{\overline{u}}{2\pi}\right)^{2/3} f^{-5/3}, \tag{4.9}$$

$$C_T^2 = \frac{\beta_T}{0.073\overline{u}^{2/3}}. \tag{4.10}$$

Here, β_T is the counterpart of β obtained through LLS regression on measured temperature spectrum $\hat{S}_T(f)$. The coefficients presented in Equations **??** are empirically derived. Hocking (1983) arrived at a similar value ($< 10\%$ error

compared to coefficients mentioned in previous works) using radar backscatter measurements of turbulence made in the boundary layer. Frehlich et al. (2003), Siebert et al. (2007), Luce et al. (2018b), Luce et al. (2019) have adopted the spectral estimation described above to estimate qualitatively consistent estimates of ϵ and C_T^2. The estimation algorithm described in the next section applies the spectral fitting method described here to compute ϵ from pitot airspeed spectra.

4.3 Estimation of ϵ

4.3.1 Problems in UAS pitot spectra

Of the three turbulence sensors on-board DH2 UAS, pitot airspeed sensor is most susceptible to noise from external factors. Figure 4.1 shows two commonly observed practical problems in pitot airspeed spectra. The DH2 rear propulsion unit consists of an electric motor and propeller assembly. Vibrations of varying severity are produced by the motor at different throttle settings, which are transmitted to the pitot pressure sensor through the DH2 airframe. The motor and structural vibrations manifest as periodic artifacts in the spectra (e.g. 'spike' at $20Hz$ in Figure 4.1). The artifacts are prominent during ascent flight legs when the motor throttle is set higher than that for descent.

A notable feature in the spectra when measuring low intensity turbulence is the sensor noise floor, which is commonly observed in the spectra of HW,

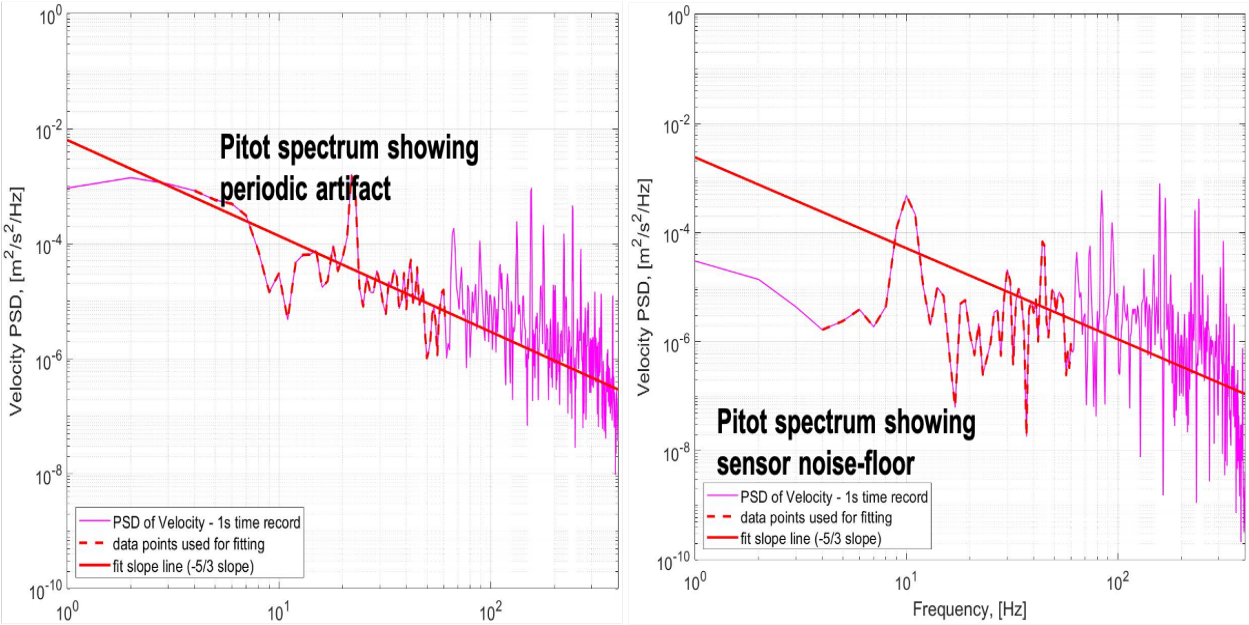

Figure 4.1: Plot shows airspeed PSD obtained (magenta) from pitot sensor during ascent leg of a typical DH2 flight. The LLS fit line (red line) was calculated using a portion of the spectrum (dashed red line) as shown. Left panel: Periodic artifact between observed $20 - 30Hz$ is due to motor vibrations. Right panel: Flattening of the spectrum depicts the sensor noise-floor.

pitot and CW indiscriminately. Figure 4.1 shows a sample pitot airspeed spectrum contaminated by the noise floor. Fitting measured spectra to a model inertial spectrum (Equation 4.6) is hampered by the contamination problems described above. The estimation algorithm developed below treats artifact and noise-floor contamination to minimize fit variance in each spectrum.

4.3.2 Estimation Algorithm

The spectral fitting algorithm devised to compute β (for use in equation 4.8) is implemented in three distinct steps. First, the calibrated airspeed data is divided into non-overlapping time series. A variance-preserving window is applied to the detrended time series. The discrete Fourier transform (DFT) is

computed and normalized by frequency to produce PSD, as shown in Figure 4.2. The periodic artifacts centered around $80Hz$ (and its harmonics at higher frequencies) contaminate the raw spectrum, thereby altering the local slope.

The high variance in the raw PSD mask the overall shape spectral shape. To reduce the spectral variance and aid in fitting the inertial subrange on to the measured spectra, the raw PSD is averaged by dividing it into equally spaced frequency bins (on log scale) and computing the mean power in each bin. The raw spectrum, frequency bins, and averaged spectrum points are illustrated in Figure 4.3. The bin-averaged spectrum drastically reduces spectral variance, and highlights the spectral shape.

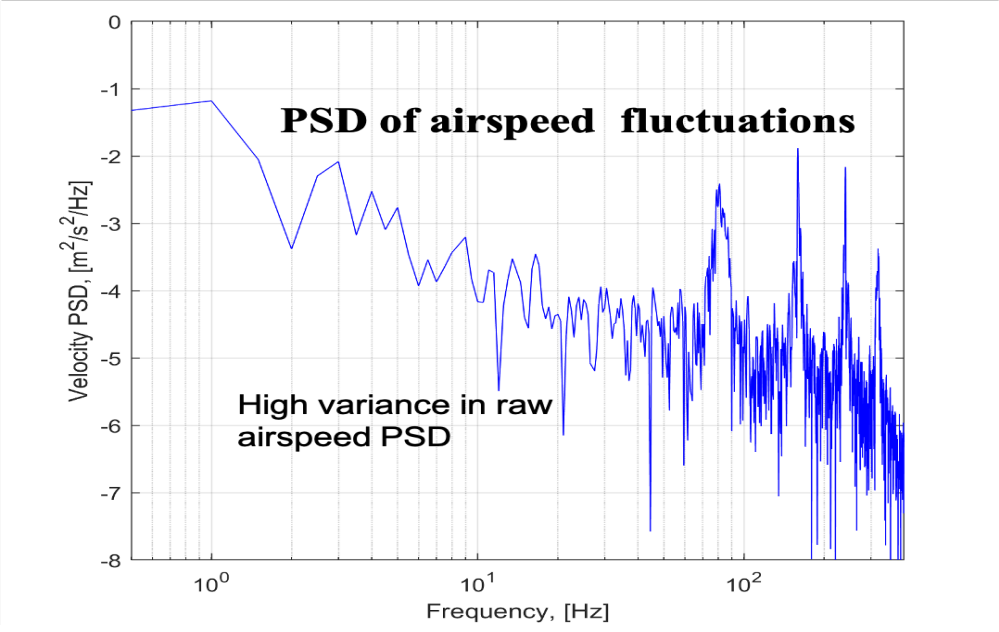

Figure 4.2: The plot shows sample pitot airspeed PSD computed from detrended and windowed time series of $5s$ duration.

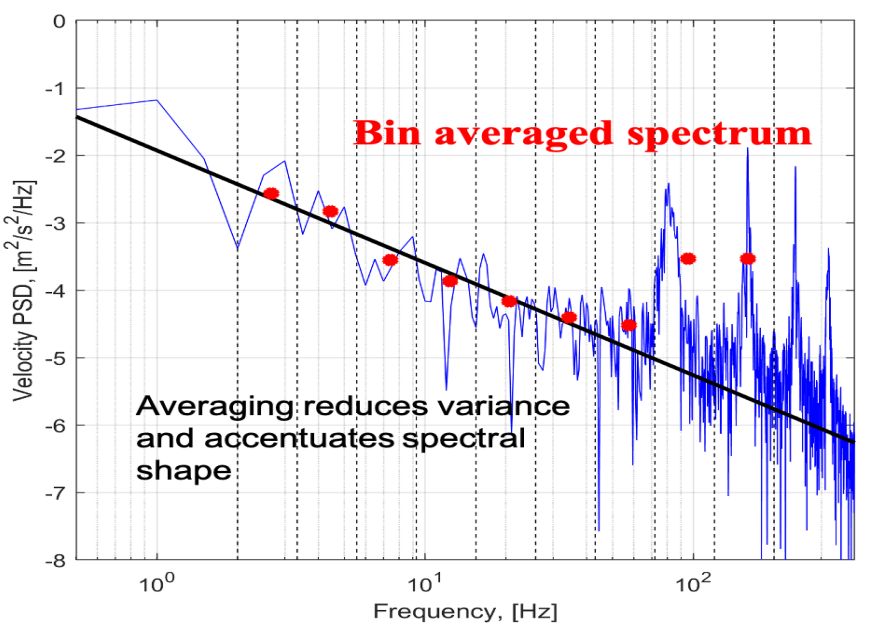

Figure 4.3: Plot shows raw PSD (blue line) and bin averaged frequency spectrum (red pucks). Frequency bins shown here are $\sim 1/5$ decade wide.

Finally, a preliminary LLS fit is conducted on the first three points of the bin-averaged spectrum and subsequent points are included iteratively in the fit. The averaged spectrum points contributing to increase the fit variance are discounted in each iteration until all the points in the averaged spectrum are exhausted. The retained spectral points are used to perform final fits, resulting in fit level estimates β which are used to determine ϵ using Equation 4.8 and its standard deviation. These steps are shown in Figure 4.4.

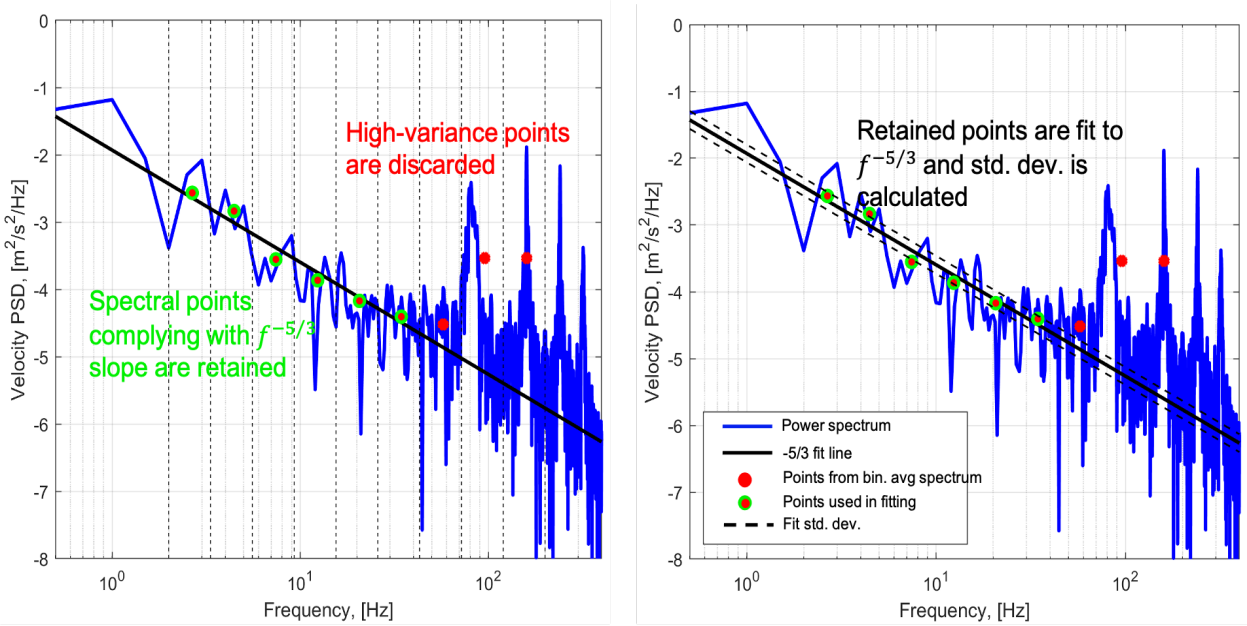

Figure 4.4: Plots show bin averaged spectrum (red pucks) and the points used in LLS fitting procedure (green pucks). The Fit line (thick black line) and fit standard deviations (dashed black lines) are also shown.

The basic steps of the spectral estimation algorithm developed above translate to deriving β_T to compute the temperature structure function parameter C_T^2 from CW measurements as well.

4.3.3 Qualifying criterion

The estimation technique described in the previous section fundamentally assumes that the spectra follow a $f^{-5/3}$ slope. The resulting ϵ estimates may contain illegitimate values emerging from poorly fit spectra emerging from non-turbulent samples. Criteria to qualify ϵ estimates are therefore essential to discard these inconsistent and misrepresented data points.

Luce et al. (2019) performs unconstrained fitting on each pitot airspeed spectra to compute actual fit slope and discounts the estimates that do not

satisfy $f^{\frac{-5}{3}\pm 0.42}$, thereby increasing the risk of discarding legitimate spectral estimates. This arbitrarily chosen qualification criterion was applied to DH pitot measurements from ShUREX2016, and ShUREX2017 data sets and used in comparison studies with VHF radar estimates of TKE dissipation rate.

Further, Luce et al. (2019) use a relationship derived by Kantha and Luce (2018) between ϵ and C_t^2 to validate their estimation method. Kantha and Luce (2018) proposed that under the conditions of stable stratification ϵ and C_T^2 are related by

$$\epsilon_{CT2} = \left(\frac{\gamma C_T^2 g_0^2}{T^2 N^2} \right)^{3/2}, \tag{4.11}$$

where $\gamma \sim 1.92$ is a parameter given by

$$\gamma = \frac{1}{\beta_\theta} \frac{1 - R_f}{R_f}. \tag{4.12}$$

Here, $\beta_\theta \sim 3$ is a universal constant, R_f is the flux Richardson number, T and N are temperature and buoyancy frequency respectively.

Following the procedure described in Luce et al. (2019), estimates of ϵ_{CT2} were computed employing the algorithm described in section 4.3.2. Figure 4.5 shows a scatter plot of ϵ_{CT2} and ϵ_{UAS} derived from pitot measurements for all data points from ShUREX2017 campaign (left panel). Also shown are the histograms of ϵ_{UAS} and ϵ_{CT2} (right panel). A regression slope of 0.97 was observed, suggesting that the UAS derived ϵ (from pitot) are overestimated. The histograms confirm this conclusion. This validation method is effective

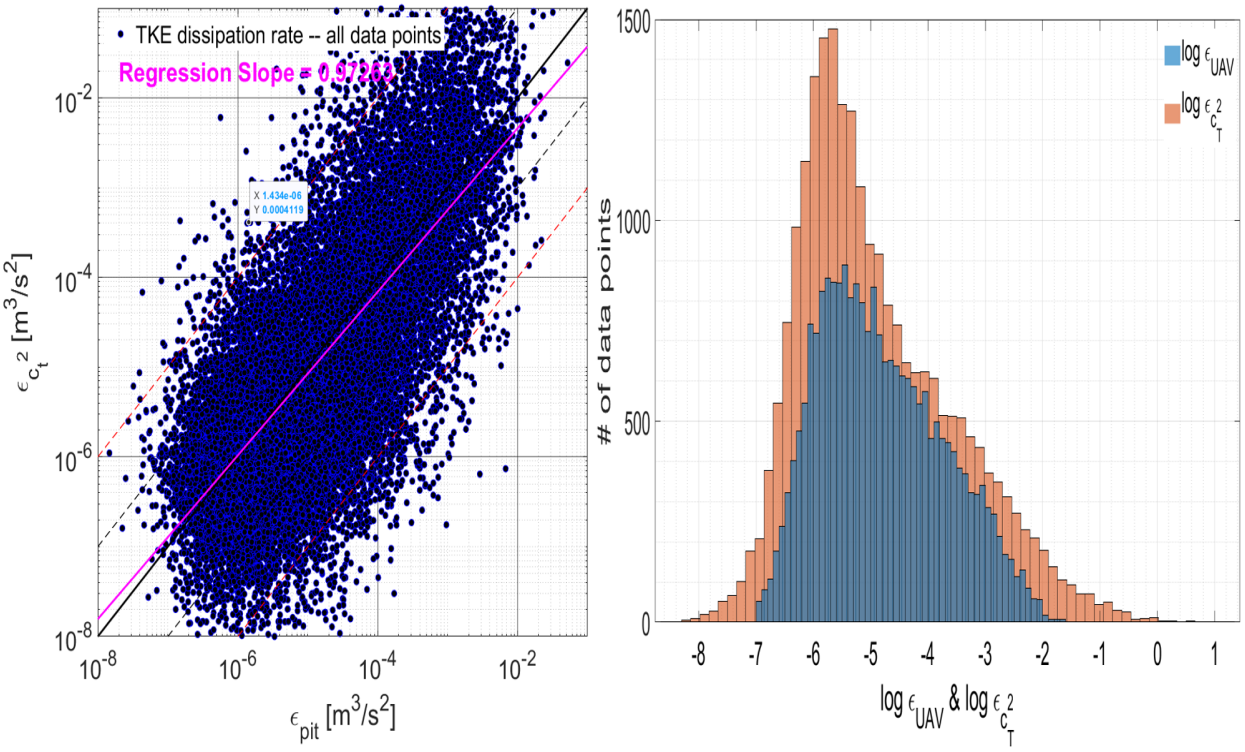

Figure 4.5: Left panel: Scatter plot of ϵ_{CT2} and ϵ_{pit}. Right panel: Histograms of ϵ_{pit} and ϵ_{CT2}.

to verify legitimate working of the estimation algorithm over a wide range of ϵ values, but fails to provide insights on the accuracy of individual data points.

The measured PSD following turbulence inertial subrange slope are expected to have small fit standard deviation, which corresponds to high confidence ϵ estimates. The fit standard deviation is calculated for each spectrum, thus providing a confidence measure for every estimated data point. Figure 4.6 shows a time series of ϵ along with error bars computed using fit standard deviation. The inset compares estimates with low and high standard deviation. Interesting profiles of ϵ are further scrutinized by visually inspecting the PSD of data points with low confidence (high standard deviation).

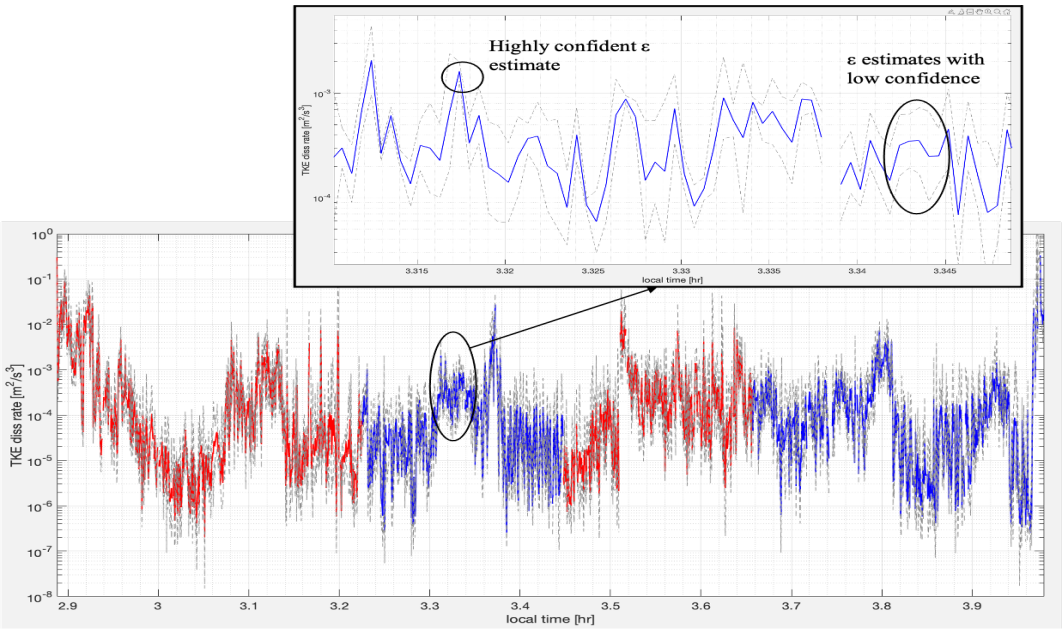

Figure 4.6: Plot showing time series of pitot derived ϵ from a representative DH2 UAS flight during IDEAL. Inset shows a comparison between high and low confidence estimates of ϵ.

The techniques described here to extract ϵ from airspeed measurements complements the technique developed by Luce et al. (2018a), which uses overlapping $50s$ segments of corrected airspeed data from the DH2 pitot sensor, collected during the ShUREX campaigns. The study uses a different technique than the one described here to discard low confidence ϵ estimates. However, while equally skillful, it does not provide error estimates of the retained epsilon points.

4.4 Results and Discussion

The spectral analysis algorithm described in this chapter translates to estimate β_T from CW temperature spectra in computing C_T^2 using Equation 4.10. Parameters such as the time series duration T, percentage of overlap

(we used non-overlapping time series), choice of window, width of frequency bins, and the range of frequencies used for fitting have implications on ϵ and C_T^2 estimates. These parameters can be appropriately 'tuned' to adjust the spectral resolution, the range of inertial subrange scales to be used in fitting and the desired spatial (or temporal) averaging of ϵ and C_T^2 estimates.

The estimation procedure described above is a fragment of the data-processing algorithm employed to derive scientific parameters using DH UAS raw measurement data. Figure 4.7 shows a flowchart which illustrates the data-processing algorithm constructed to derive turbulence parameter estimates of TKE dissipation rate ϵ and C_T^2. Initial steps to check (and treat when necessary) for 'time synchronization' between various data arrays (procedure not discussed in this document) are vital to ensure consistency between the measurements of T/RH, pressure and airspeed data recorded.

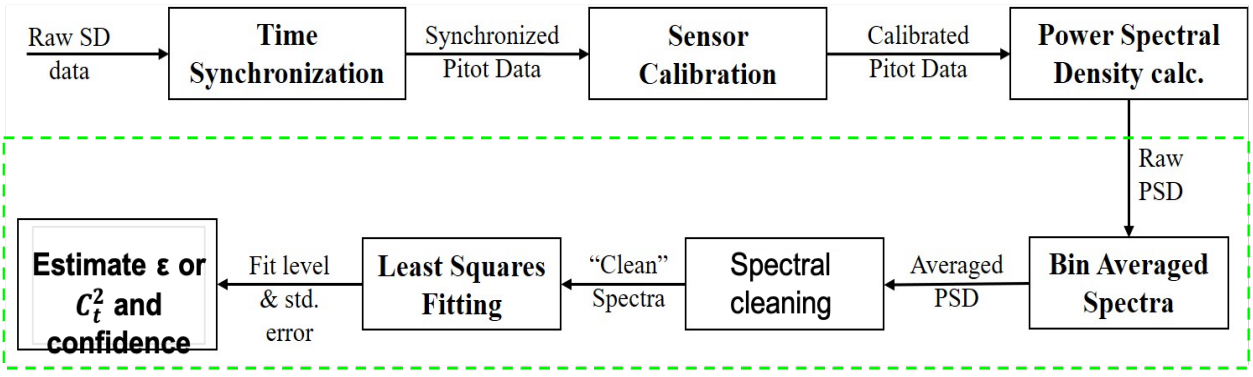

Figure 4.7: Block diagram illustrating different steps of the spectral analysis algorithm employed to estimate ϵ and C_T^2.

Every UAS flight dataset produces 1000s of spectra each from HW, pitot, and CW measurements. The spectra have unique contamination problems

due to the changing intensities and frequencies of periodic artifacts. Despite these uncertainties, the spectral estimation algorithm was progressively made robust by visually inspecting large volumes of spectra to identify patterns in spectral contamination and generalize the spectral 'cleaning' step of the estimator.

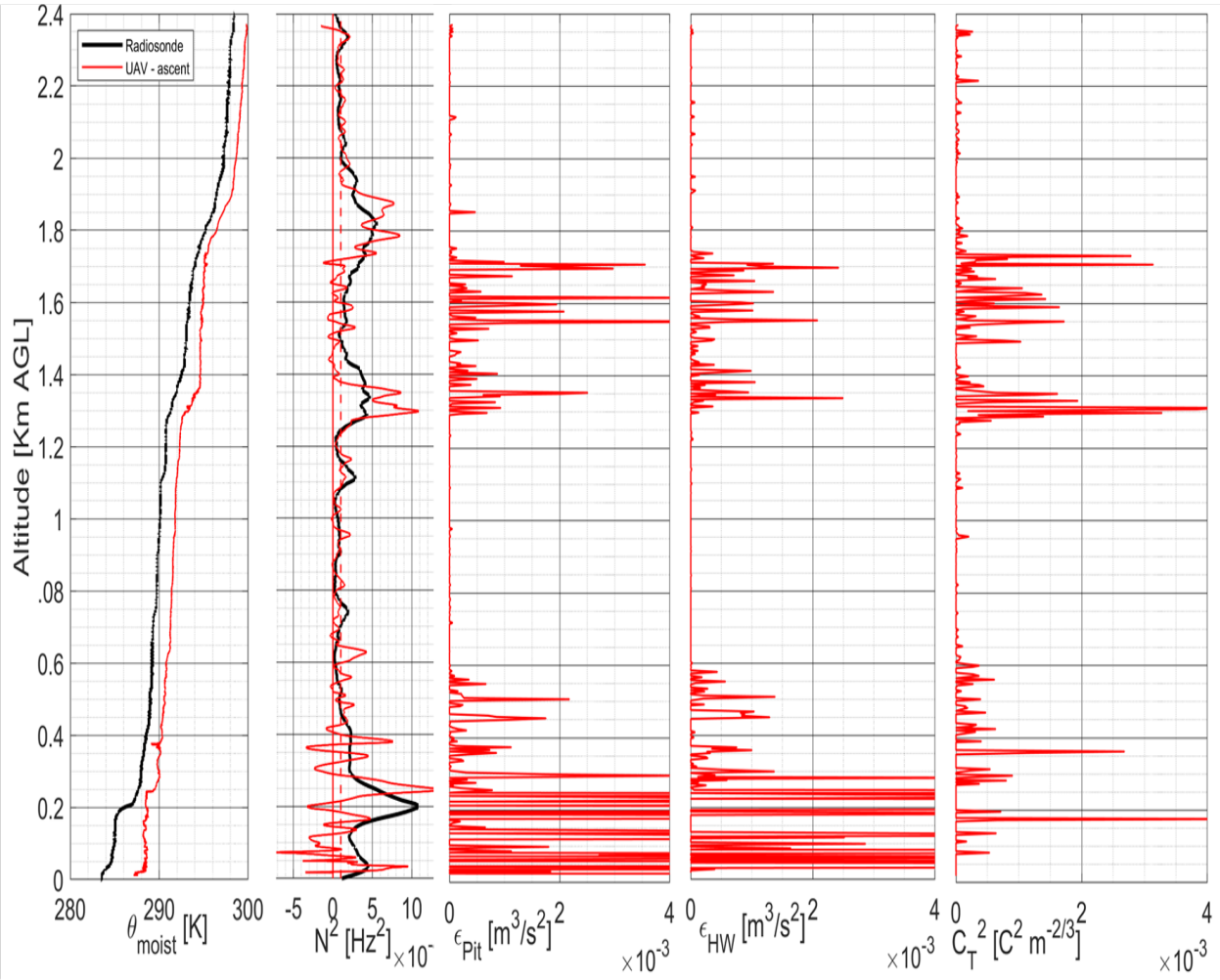

Figure 4.8: Plot shows ascent profiles of potential temperature θ, buoyancy frequency N^2, ϵ_{pit}, ϵ_{hw}, and C_T^2 for a representative data set from IDEAL campaign. Note: θ and N^2 are also shown for concurrent radiosonde dataset.

Altitude profiles of ϵ and C_T^2 estimates taken from an IDEAL flight data set are presented in Figure 4.8. The buoyancy frequency (N^2) infers two regions

of enhanced stability (stable 'sheets') undulating about $\sim 800m$ and $\sim 1500m$ with a marginally stable layer laminated in-between. S&L structures found in the lower troposphere are theorized to exhibit regions of intermittent turbulence at the fringes of the stable sheets. The UAS derived profiles of ϵ and C_T^2 are consistent with this hypothesis.

The estimation algorithm was applied to all DH2 UAS flight datasets from IDEAL, ShUREX2016-2017, MOSAiC, and POPEYE campaigns. Estimates of ϵ and C_T^2 were found to be generally consistent with the background atmospheric dynamics described in the literature. However, carefully designed UAS experiments of turbulence with universally accepted instruments like radars and instrumented towers are necessary to further invoke more confidence in UAS derived turbulence parameters.

Chapter 5

Wind Estimation

5.1 Introduction

Vertical sounding UAS have become valuable instruments for data collection in atmospheric boundary layer research. Most boundary layer phenomena, predominantly shear or buoyancy driven, are becoming increasingly interesting for the wind energy community. Rigorous study of boundary layer processes involve characterizing shear, turbulent fluxes and dynamic instabilities, which require accurate 3D wind measurements. Atmospheric wind sensing using in-situ instruments has been pursued for over five decades (Wyngaard, 1968; Axford, 1968). We briefly digress from turbulence sensing and data processing into the subject of atmospheric wind sensing and estimation techniques. Our scope is strictly limited to fixed-wing aircraft, as wind estimation techniques for copters employ techniques unique to that platform.

A wide variety of UAS have been used to measure atmospheric winds. Multi-hole probe combined with aircraft inertial measurement unit (IMU) is

desirable for 3D wind sensing using fixed-wing UAS. van den Kroonenberg et al. (2008) reports an accuracy of $0.5m\ s^{-1}$ in the vertical wind component using a custom 5-hole probe and IMU on the MMAV platform. Bäserud et al. (2016) reports horizontal wind with $1m\ s^{-1}$ uncertainty for the SUMO UAS. Manta (Thomas et al., 2012a) also employs a custom 5-hole probe and IMU to sense vertical winds as small as $0.17m\ s^{-1}$. Calmer (2018) catalogs wind sensing instruments and estimation techniques used by various contemporary UAS platforms, and presents detailed error analysis for each.

Section 5.2 describes the standard wind estimation technique proposed by Axford (1968) and refined by Wyngaard (1968) for fixed-wing aircraft. Some shortcomings of this method and the challenges for micro-class UAS are discussed. Section 5.3 illustrates a novel wind estimation technique developed exclusively for micro-class UAS. Finally, the resulting wind estimates and their implications are presented in Section 5.4.

5.2 Wind Sensing Challenges for Micro-Class UAS

3D wind vector from a moving platform is easily visualized using the vector wind triangle defined by

$$\vec{V}_{gps} = \vec{W} + \vec{V}_{as}. \tag{5.1}$$

$\vec{V}_{gps}$ is the GPS velocity, $\vec{V}_{as}$ is the relative wind, and $\vec{W}$ is the vector wind. 3D airspeed sensors, like multi-hole probes and sonic anemometers, provide measurements of $\vec{V}_{as}$. Winds are inferred from Equation 5.1 by combining

aircraft attitude estimates with 3D airspeed measurements provided by the aircraft standard sensor suite (IMU+3D airspeed sensor data) and GPS velocity. Typically, aircraft include an IMU equipped with 3D accelerometer, 3D gyroscope, GPS and an airspeed sensor.

The standard wind estimation technique described by Equation 5.1 was employed to calculate the horizontal wind vector from DH2 UAS. Figure 5.1 shows sample wind estimates (horizontal wind magnitude) taken over one circle from the helical flight trajectory of DH2 UAS. The artifact in wind magnitude observed between 2000 and 2015s in the time series occurs periodically on each circle. The periodic artifacts were found to be correlated with aircraft bearing angle, as shown in Figure 5.2.

Lightweight aircraft, such as the DH2, exhibit complex motions when banking steeply. This occurs when the aircraft maneuvers the high-ground speed upwind-downwind transition on each circle (for circular sampling trajectories). Data suggests that the apparent increase in airspeed results from loss of altitude during this high-speed turn (see Figure 5.1). The inset in Figure 5.1 shows the time spent by DH2 on upwind (yellow markers) and downwind (blue markers) legs. Aircraft quickly maneuvers through downwind flight legs (made apparent by sparser data points in Figure 5.2 inset) accentuating differences in sensor time constants. Pitot airspeed (800Hz), GPS velocity vector (5Hz), and IMU attitude estimates (100Hz) are suspected to record unsynchronized information due to non-uniform sensor bandwidths

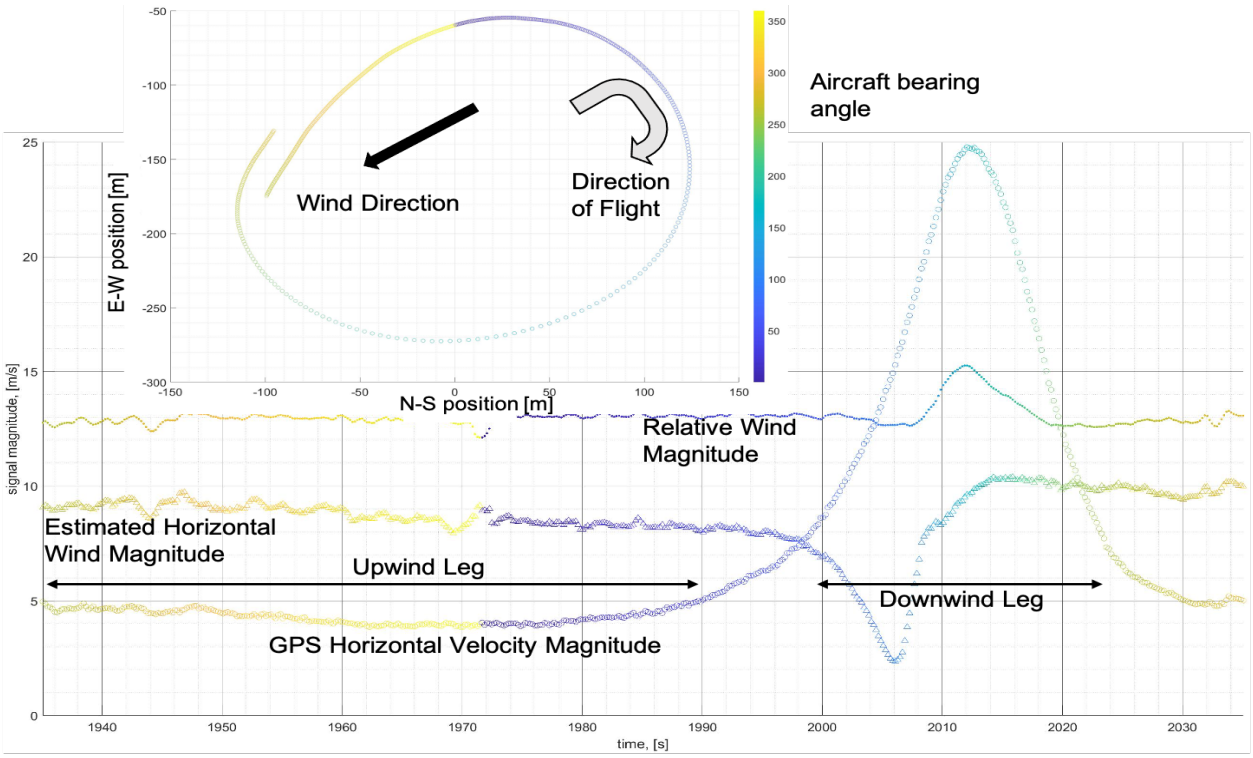

Figure 5.1: Measured horizontal GPS (circle), relative wind (dots), and estimated wind magnitudes (triangles) over one circular trajectory (inset). The upwind and downwind legs are marked based on aircraft bearing referenced to the circle center point.

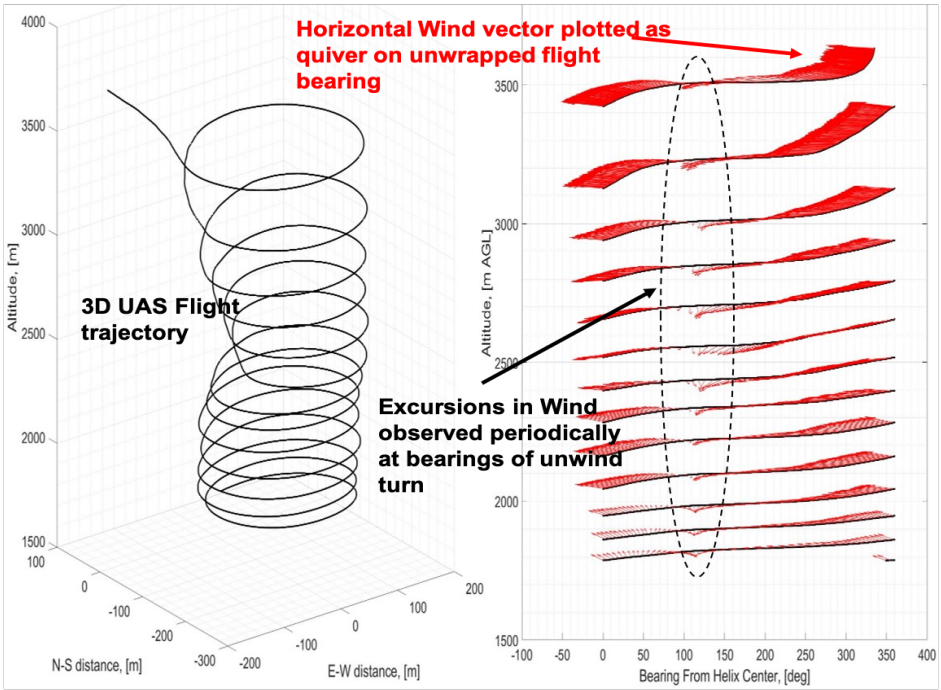

Figure 5.2: The aircraft bearing plot shows periodic artifacts in estimated wind magnitude. Artifact are observed between 75° and 150° bearing angle (right tile).

(see Table 1.2). This information mismatch manifests in the form of periodic artifacts at corresponding flight bearing angles.

Micro-class UAS are severely limited by payload and space constraints. Sophisticated multi-hole pressure probes and sonic anemometers implemented on large fixed-wing UAS are impractical for use on small and lightweight aircraft. Instead, small UAS are mounted with miniature pitot probes and IMU instruments that do not provide angle of attack α and side-slip angle γ information, which hampers the ability to estimate 3D winds. The following sections of this chapter discuss a novel horizontal wind estimation technique suitable for DH2 and other lightweight UAS using limited information provided by the standard autopilot sensors. Estimated wind data is compared to concurrent radiosonde and VHF radar data obtained from IDEAL and ShUREX campaigns.

5.3 Development of Wind Estimation Algorithm

Preliminary analysis of horizontal wind vector derived using standard estimation technique highlighted the deficiencies in DH2 measured data. In this section, a mean wind estimation procedure is developed. The method uses the pitot-measured airspeed, horizontal GPS velocity and guidance from aircraft attitude estimates to deduce physically consistent, time averaged horizontal wind velocity components.

The estimation algorithm uses the wind triangle, re-arranged to solve for

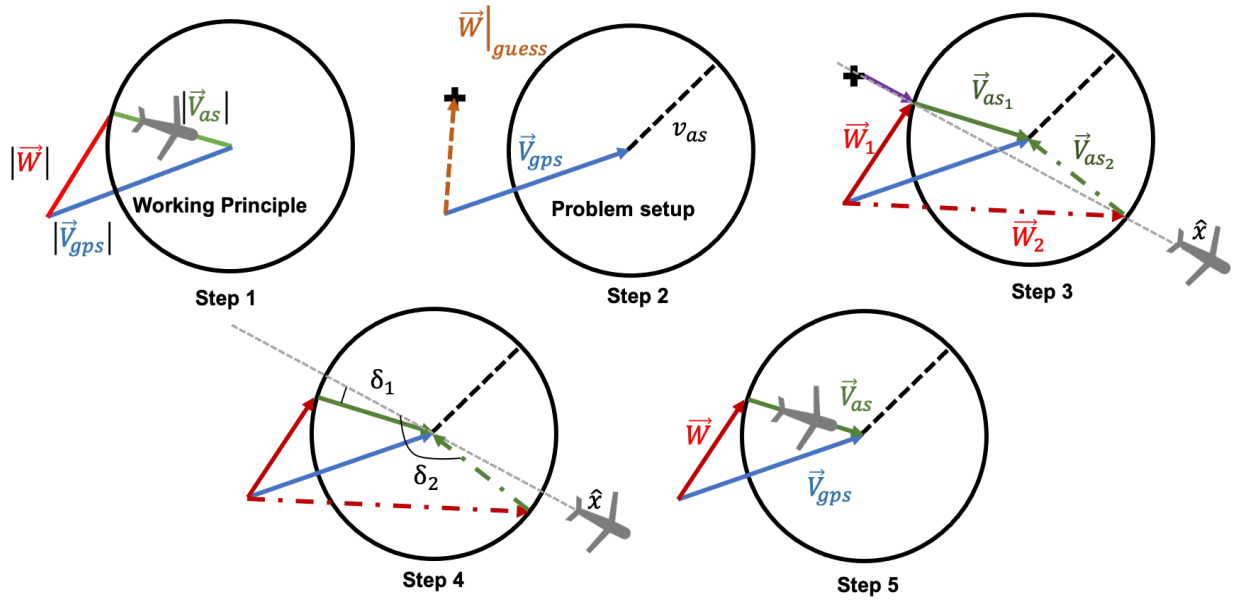

Figure 5.3: An illustration of the novel wind estimation algorithm (left). Also shown is the governing iteration scheme (right).

relative wind magnitude (squared). This infers that the wind vector compatible with the measurements of GPS velocity vector and airspeed magnitude lies on a circle with center at $\vec{V}_{gps}$ and radius $\left|\vec{V}_{as}\right|$. This is termed the 'wind circle' in Lawrence and Balsley (2013) and given by

$$v_{as}^2 = \left|\vec{V}_{as}\right|^2 = \left|\vec{V}_{gps} - \vec{W}\right|^2. \tag{5.2}$$

Figure 5.3 shows steps of the estimation algorithm.

Since this procedure is iterative, it requires a previous estimate $\vec{W}_g$ for each new estimate. We found that it is important to begin the iterations from a reasonable starting point. For this, wind data derived from standard estimation technique is heavily filtered to remove periodic oscillations and

used as $\vec{W}_g$. The guessed wind estimate $\vec{W}_g$ is projected onto the circle in the direction of estimated vehicle attitude $\hat{x}$, resulting in two wind solutions $\vec{W}_{1,2}$ and corresponding relative wind vectors, $\vec{V}_{as_{1,2}}$ as shown in Step 3 of Figure 5.3. $\vec{W}_g$ is corrected by

$$\vec{W}_{1,2} = \vec{W}_g + \lambda_{1,2} \times \vec{V}_{as}, \tag{5.3}$$

where the product terms $\lambda_{1,2} \times \vec{V}_{as}$ is the correction factor. The direction of resulting relative winds $\hat{V}_{as_{1,2}}$ are compared to the estimated aircraft attitude $\hat{x}$ to determine a compatible wind solution. This is given by

$$\delta_{1,2} = cos^{-1} \left(\frac{\hat{x}.\vec{V}_{as_{1,2}}}{|\hat{x}| \left| \vec{V}_{as_{1,2}} \right|} \right). \tag{5.4}$$

The wind vector corresponding to the smaller value between $\delta_{1,2}$ is retained, and the alternate solution is discarded. For instance, in Figure 5.3 $\delta_1 < \delta_2$ therefore $\vec{W}_1$ and $\vec{V}_{as_1}$ are retained.

The horizontal wind vector obtained by the method described above exhibited biases due to small systematic errors in the previous estimates, from which the new intercept on each circle was computed. As the GPS velocity rotates around on a circular flight trajectory, the previous wind estimate is always to the same side of the new wind solution circle. This causes the projection onto the circle in the direction of aircraft compass heading to be biased consistently. To combat this problem, a sub-iteration scheme was

applied to run the estimation backwards in time for a short interval, then forward in time up to the present. This produces sub-iteration systematic biases for circle intercept in opposite directions that effectively cancel in the resulting final estimates.

It should be noted that although this technique shares the fundamental 'wind circle' geometry with the precursor method of Lawrence and Balsley (2013), there are significant improvements in the current approach. The previous approach developed the wind vector solution by finding the intersection of two successive 'wind circles'. This suffers from nearly indeterminate solutions if the circles are positioned close together, as happens if GPS velocity data is not changing significantly between data points used. Solutions are better constrained by using GPS velocity data from more widely separated points in time, but this causes the resulting wind estimates to be averaged over larger time intervals. The current approach does not have inherent averaging since it is finding the instantaneous projection onto the 'wind circle' using GPS data at a single time instant. Also, the use of aircraft attitude to disambiguate the two potential circle intercept solutions is much more robust than the older technique of choosing the smaller wind vector of the two, since there can be times when the two solutions are close to the same magnitude.

5.4 Results and Discussion

A variety of auxiliary wind measurement instruments were deployed during field campaign in Japan (ShUREX2017). Horizontal wind components measured by periodic radiosonde soundings, a $49.5MHz$ VHF radar (Mu Radar), and a $1.3GHz$ UHF radar wind profiler (LQ7 radar WP) were used to conduct preliminary validation studies of UAS wind estimates. Figure 5.4 compares UAS, radiosonde, VHF and UHF radar wind speeds and directions. UAS flights were conducted $\sim 1km$ upwind of the radar site. Therefore, UAS wind estimates are adjusted to account for advection. UAS wind estimates of large-scale flow structures such as the deep speed shear between $400 - 2000m$ agree with those from radar and radiosonde measurements. UAS local wind estimates occasionally showed excursions outside the confidence bounds of VHF radar wind estimates. This behavior was generally observed with local shear enhancement in UAS-derived winds.

General agreement in wind estimates of large-scale flow features was also observed from concurrent UAS and radiosonde measurements from IDEAL field campaign data. Figure 5.5 compares wind estimates from UAS and concurrent radiosonde deployed at a location $\sim 10km$ away from the UAS deployment site. As such, discrepancies between radiosonde and UAS-derived wind vectors during the IDEAL campaign, larger than those during the ShUREX campaigns, can be expected. UAS wind estimates from both campaigns contain local shear enhancements (prominent at $1100m$ in Figure 5.5), which

cannot be validated due to lack of concurrent and co-located datasets. Available data sets provide insufficient evidence to draw concrete conclusions about the local shear enhancement disparities in small-scale wind structures of UAS, radiosondes and radars. Therefore, carefully designed validation experiments centered around radars and radiosondes are necessary to further verify UAS wind estimates.

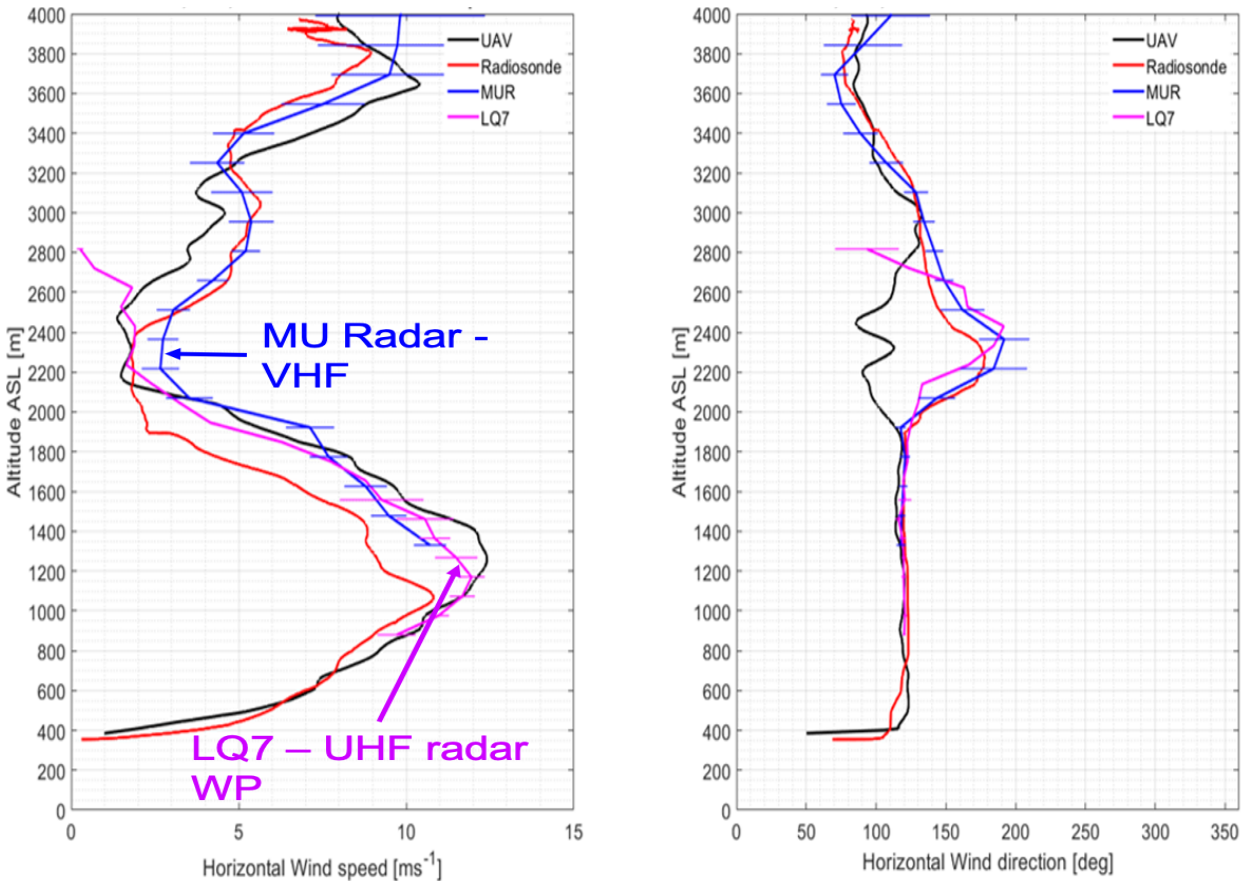

Figure 5.4: Horizontal wind speed and direction estimated using UAS and concurrent radiosonde, VHF and UHF radars from ShUREX2017 campaign. The VHF and UHF radar wind profiles are averaged over $30min$ (time taken for UAS ascent to $3500m$ AGL) duration with range resolution of $150m$

The algorithm relies on short-term variations in GPS velocity vector and aircraft attitude to improve wind estimates during successive iterations. Wind

estimates for helical profiling flight trajectories were found to closely agree with concurrent wind measurement instruments, whereas the winds estimated from DH2 transect flights, where GPS velocity is nearly constant for the strait transect portions of the path, resulted in inaccuracies and noticeable biases. This behavior necessitates further study.

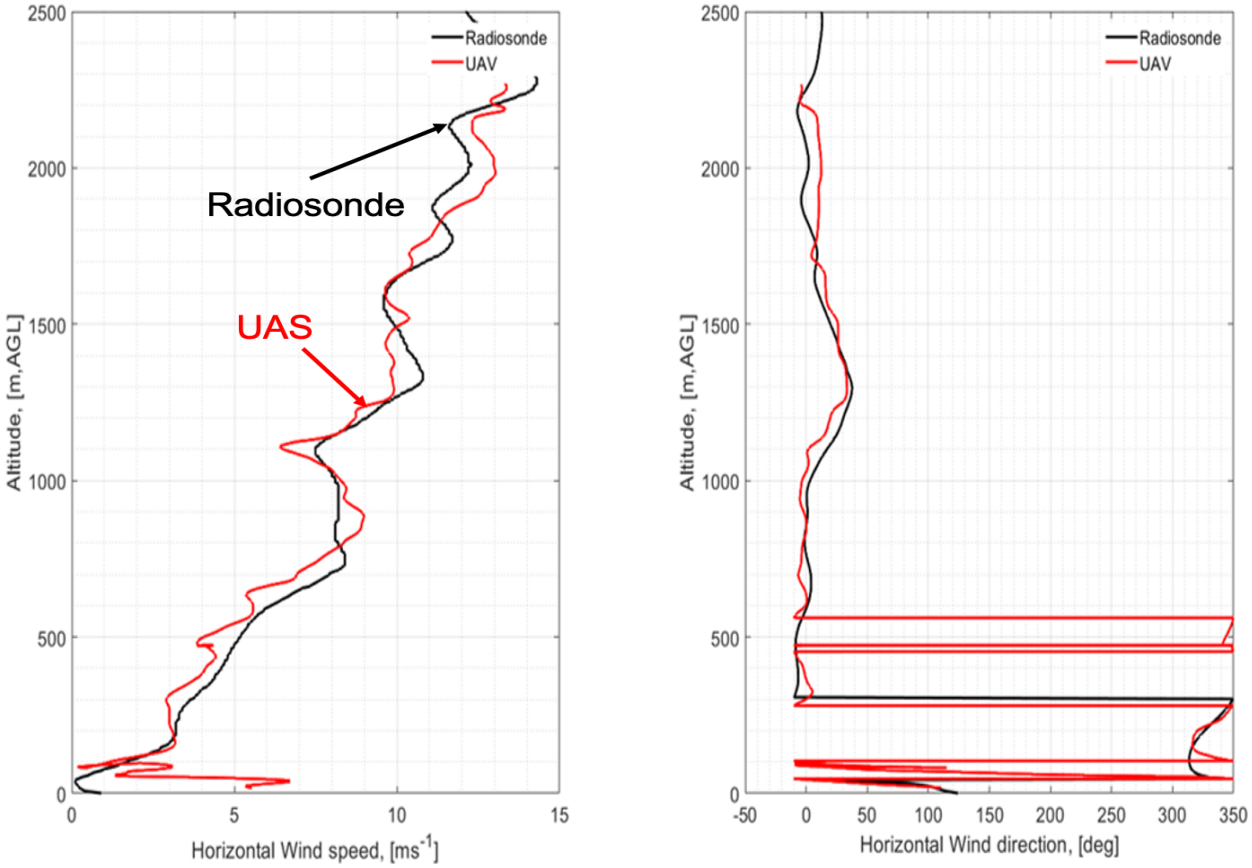

Figure 5.5: Horizontal wind speed and direction estimates derived using UAS and concurrent radiosonde measurements from IDEAL field campaign. The radiosonde was deployed at 03:02 AM local time downstream ($\sim 10km$). The DH2 UAS was launched at 3:24 AM local time.

Determination of turbulent fluxes require accurate estimates of small-scale vertical wind variations. The wind estimation method discussed in this chapter was limited to zonal and meridional wind components due to lack of angle of attack (AOA) measurements. AOA is adjusted by the autopilot elevator to

track variable climb rate and airspeed setpoints, so does not have a consistent weathervaning equilibrium value as does sideslip. Even though AOA varies throughout a limited range in flight, the large airspeed magnitude makes the vertical component of the relative wind vector very sensitive to uncertainty in AOA. Moreover, vertical winds are typically much smaller than horizontal winds, making the required vertical precision in wind estimation larger. These effects conspire to render poor vertical wind estimates on the DH2. Some means of AOA measurement is necessary for quality 3D wind sensing.

To summarize, in this chapter we have described and validated a novel horizontal wind estimation technique suitable for DH2 and other lightweight micro-class UAS, using limited information provided by the standard autopilot sensors. Essentially, the estimator corrects the guessed wind vector by collapsing it onto the circle described by Equation 5.4 in the direction of estimated aircraft attitude and selecting out of the two solutions, the one that provides the wind vector closest to the aircraft attitude vector. Validation of the technique was obtained by comparing the estimated wind vector to concurrent radiosonde data obtained during the IDEAL campaign and radiosonde and radar data obtained during the ShUREX campaigns. The technique is a significant improvement on existing 'GPS correction' algorithms, which compute the wind vector from UAS-borne instruments.

Chapter 6

Conclusions and Future Work

Lightweight, and relatively inexpensive micro-class autonomous UAS are versatile meteorological observation platforms. In addition to providing standard meteorological data, UAS can be implemented to make routine turbulence measurements in the lower troposphere. The principal objectives of the investigations described in this dissertation were twofold. First, to improve the accuracy and reliability of current turbulence sensing capabilities of the University of Colorado DataHawk UAS. Second, to obtain insightful turbulence data products to further our understanding of complex, small-scale turbulence processes.

The first research study focussed on implementing carefully designed protective elements to shield the delicate HW and CW turbulence sensors onboard the DH2 UAS. A wind tunnel study to characterize the distortion effects in the measured HW spectra arising due to the introduction of protective elements was conducted. The original protective shroud employed on all iterations of DH2 UAS before the IDEAL observational campaign was

redesigned based on results of this study. Field tests comparing the measurements made by the HW sensor protected by the redesigned shroud with the HW in free-stream flow showed negligible distortion to the turbulence inertial subrange spectrum recorded by the protected HW. The field test showed that the obstructive effects of the redesigned cylindrical shroud had negligible effect on the inertial subrange scales relevant to geophysical turbulent flows. Various other UAS platforms have produced a proof-of-concept for measurements of turbulent winds using multi-hole pressure probes (Alaoui-Sosse et al., 2019; Theuerkauf et al., 2011; Wildmann et al., 2014a; Bäserud et al., 2016; Dehghan et al., 2014). However, the low sensor bandwidth limited their ability to resolve turbulent variations at wavenumbers $< 5m^{-1}$ at a nominal airspeed of $17m\ s^{-1}$. Implementing the redesigned fine-wire protective shroud enabled the DH2 UAS to measure turbulent variations in airspeed and temperature up to wavenumbers $26m^{-1}$ at a nominal airspeed of $15m\ s^{-1}$, enabling more accurate turbulence parameterization by capturing and fitting 2 decades of uncorrupted spectral data from the measured geophysical inertial subrange.

The DH2 UAS equipped with the protected fine-wire sensors has been used in conducting measurements of small-scale turbulence supporting POPEYE observational campaign (de Boer et al., 2019) to characterize the polar boundary layer structure and improve forecasting models. The DH2 UAS was also employed to characterize the small-scale, weak turbulence layers during the

IDEAL observation campaign Doddi et al. (2021). The DH2 UAS measurement datasets along with auxiliary instrument data from POPEYE, IDEAL, and LAPSE-RATE field campaigns are available at `https://www.archive.arm.gov/discovery/`, `https://www.eol.ucar.edu/field_projects/ideal`, `https://zenodo.org/communities/lapse-rate/?page=1&size=20`.

The multi-hole probes employed by most contemporary UAS to infer 3D turbulent winds require extensive calibration in a wind tunnel, and in some instances also require that the aircraft perform calibration flight maneuvers. The post-flight HW calibration technique was developed to simplify the tedious and impractical task of calibrating each HW used in an observational campaign. BLUECAT developed at the University of Kentucky, along with DH2, are the only two UAS platforms employing HW anemometers for atmospheric turbulence measurements and use HW flight-data to calibrate the sensor post-flight. Although the novel calibration method described here, based on spectral analysis of co-located pitot sensor, was developed to enable turbulence data analysis of HW measurements made during IDEAL campaign, this calibration technique has also enabled the analysis of HW turbulence measurements from DH1/DH2 from ShUREX2015-2017, LAPSE-RATE, POPEYE and MOSAiC observational campaigns.

The second research study in this thesis focused on deriving insightful data products from UAS sampled data for use in scientific analysis of atmospheric turbulence. Robust spectral estimation algorithms were developed to com-

pute turbulence kinetic energy dissipation rate ϵ and turbulence temperature structure function parameter C_T^2 from DH2 measured pitot, HW and CW turbulence data samples, as well as an effective method of qualifying the confidence in these estimates.

The UAS literature suggests that the multi-hole probes employed to conduct UAS studies of boundary layer turbulence only resolve the large-scale features of the turbulence inertial subrange. This is due to the low sensor bandwidths (because multi-hole probes are bulky) and poor SNR. In contrast, turbulence measurements from pitot and HW measurements of DH2 UAS show good agreement in ϵ_{pit} and $\epsilon_{hw} > 10^{-5} m^2 s^{-3}$ in the inertial subrange scales up to wavenumbers of $14 m^{-1}$ at a nominal airspeed of $15 m\ s^{-1}$. This suggests that the custom pitot sensor on-board the DH2 UAS provides measurements of small-scale turbulence as reliably as the co-located HW anemometer.

Additionally, a novel wind estimation algorithm tailored to use the *available* sensor data from micro-class UAS (pitot airspeed, GPS velocity, and aircraft attitude estimates) was developed. Studies comparing concurrent UAS, radiosonde, VHF radar, and radar wind profiler derived horizontal wind estimates from ~ 40 ShUREX2017 campaign datasets showed good qualitative agreement in large-scale flow structures.The UAS wind estimates showed regions of enhanced local speed shears, with discrepancies as large as $2 m\ s^{-1}$ when compared with time averaged wind measurements by a distant radar

wind profiler. It remains unclear whether these smaller scale differences are due to estimation errors, or due to actual differences in the conditions being measured due to separation in time and space.

Extensive efforts have been invested to automate the data processing and estimation procedures to be seamlessly applied to the overwhelming amounts of data gathered by UAS from field campaigns. A data processing codebase, exclusively to all collaborators of DataHawk UAS, complete with comprehensive documentation describing the working principles of various algorithms are archived at `https://github.com/DataHawkUAS/dhscripts`. A total of $\sim$ 400 hours of DH2 measurement datasets have been processed using the data processing program suite. Estimates of ϵ, C_T^2, and horizontal wind components derived from DH2 UAS measurements have been used to parametrize turbulence in the convective boundary layer and S&L during ShUREX2015-2017 field campaigns (Kantha et al., 2017a,b; Kantha and Luce, 2018; Kantha et al., 2019; Luce et al., 2018b,a, 2019), the nocturnal boundary layer and S&L during IDEAL campaign (Doddi et al., 2021), and polar boundary layer characterization during POPEYE and MOSAiC field campaigns (De Boer et al., 2016; de Boer et al., 2019).

6.1 Suggestions for Future Work

The research studies described in this dissertation form a basis for expanding turbulence sensing capabilities of autonomous UAS in several directions.

The spectral estimation algorithm developed in Chapter 4 conducts fits in an arbitrarily chosen set of frequencies (between $2Hz$ and $200Hz$). The upper bound of the frequency range is limited by the sensor Nyquist frequency of $400Hz$. This is inadequate to resolve the turbulent scales up to the viscous subrange. In principle, the sensor Nyquist frequency can be used as the upper frequency bound used in spectral fitting. But the sensor bandwidth tends to roll-off around the Nyquist frequency, and therefore it is appropriate to choose a frequency slightly lower than the Nyquist frequency. The lower frequency bound of the inertial subrange coincides with the outer scale of turbulence and often scales as the characteristic dimension of the turbulence source. A more scientific procedure would be to first identify stratified layer depths between sheets using potential temperature, then restrict the time intervals in spectral analysis to remain within these layers. This prevents using an outer scale that exceeds the layer depth, and prevents an analysis interval from blending together characteristics from turbulent layers with the more stable sheets. A dynamically consistent frequency range used for inertial subrange fitting is expected to further improve the estimation accuracy of turbulence parameters.

There is immense value in implementing the post-flight spectral estimation procedures on-board the DH2 UAS to telemeter estimates of ϵ and C_T^2 on-the-fly. This provides better guidance to alter the aircraft flight trajectory to track interesting turbulence events. This could even be the basis for

techniques of automatic seeking or tracking of particular turbulence features through autonomous flight control.

There is still some ambiguity about turbulence parameters derived from fixed-wing UAS measuring along slant-path trajectories in the stably stratified atmosphere. Fixed-wing aircraft sampling along shallow slant-path trajectories are suspected to measure predominantly the horizontal variations. But measurements along slant-path trajectories are routinely treated as vertical profiles during turbulence analysis. High-resolution, idealized Direct Numerical Simulations (DNS) could aid in resolving these ambiguities (Balsley et al., 2018b). A hypothetical UAS probe could be 'flown' within the simulation domain to evaluate the impacts of various sampling strategies on measured turbulence data products, treating the simulation as the 'truth' so the accuracy of these 'measurements' can be evaluated (Wainwright et al., 2014; Lundquist et al., 2015; Gasch et al., 2020). This approach could further be extended to tailor optimum trajectories to sample particular atmospheric turbulence events.

References

Aberson, S. D. and Franklin, J. L. (1999). Impact on Hurricane Track and Intensity Forecasts of GPS Dropwindsonde Observations from the First-Season Flights of the NOAA Gulfstream-IV Jet Aircraft. *Bulletin of the American Meteorological Society*, 80(3):421–428.

Alaoui-Sosse, S., Durand, P., Medina, P., Pastor, P., Lothon, M., and Cernov, I. (2019). OVLI-TA: An Unmanned Aerial System for Measuring Profiles and Turbulence in the Atmospheric Boundary Layer.

Altstädter, B., Platis, A., Wehner, B., Scholtz, A., Wildmann, N., Hermann, M., Käthner, R., Baars, H., Bange, J., and Lampert, A. (2015). ALADINA – an unmanned research aircraft for observing vertical and horizontal distributions of ultrafine particles within the atmospheric boundary layer. *Atmos. Meas. Tech.*, 8(4):1627–1639.

Argrow, B., Frew, E., Houston, A., Elston, J., Stachura, M., Roadman, J., and Lahowetz, J. (2011). The Tempest UAS: The VORTEX2 Supercell Thunderstorm Penetrator. In *Infotech@Aerospace 2011*, In-

fotech@Aerospace Conferences. American Institute of Aeronautics and Astronautics.

Axford, D. N. (1968). On the Accuracy of Wind Measurements Using an Inertial Platform in an Aircraft, and an Example of a Measurement of the Vertical Mesostructure of the Atmosphere. *Journal of Applied Meteorology*, 7(4):645–666.

Balsley, B. B. (2008). The CIRES Tethered Lifting System: a survey of the system, past results and future capabilities. *Acta Geophysica*, 56(1):21–57.

Balsley, B. B., Frehlich, R. G., Jensen, M. L., and Meillier, Y. (2006). High-Resolution In Situ Profiling through the Stable Boundary Layer: Examination of the SBL Top in Terms of Minimum Shear, Maximum Stratification, and Turbulence Decrease. *Journal of the Atmospheric Sciences*, 63(4):1291–1307.

Balsley, B. B., Frehlich, R. G., Jensen, M. L., Meillier, Y., and Muschinski, A. (2003). Extreme Gradients in the Nocturnal Boundary Layer: Structure, Evolution, and Potential Causes. *Journal of the Atmospheric Sciences*, 60(20):2496–2508.

Balsley, B. B., Jensen, M. L., Frehlich, R. G., Eaton, F. D., Bishop, K. P., and Hugo, R. J. (1999). In-situ turbulence measurement technique using state-of-the-art kite/blimp platforms. In *Proc.SPIE*, volume 3706.

Balsley, B. B., Lawrence, D. A., Fritts, D. C., Wang, L., Wan, K., and

Werne, J. (2018a). Fine Structure, Instabilities, and Turbulence in the Lower Atmosphere: High-Resolution In Situ Slant-Path Measurements with the DataHawk UAV and Comparisons with Numerical Modeling. *Journal of Atmospheric and Oceanic Technology*, 35(3):619–642.

Balsley, B. B., Lawrence, D. A., Fritts, D. C., Wang, L., Wan, K., and Werne, J. (2018b). Fine structure, instabilities, and turbulence in the lower atmosphere: High-resolution in Situ Slant-Path measurements with the DataHawk UAV and comparisons with numerical modeling. *Journal of Atmospheric and Oceanic Technology*, 35(3):619–642.

Balsley, B. B., Lawrence, D. A., Woodman, R. F., Fritts, D. C., Balsley, B. B., Lawrence, D. A., and Woodman, R. F. (2013). Fine-Scale Characteristics of Temperature, Wind, and Turbulence in the Lower Atmosphere (0–1,300 m) Over the South Peruvian Coast. *Boundary-Layer Meteorology*, 147(1):165–178.

Barat, J. (1982). Some Chatacteristics of Clear-air Turbulence in the Middle Stratosphere. *Journal of the Atmospheric Sciences*, 39(11):2553–2564.

Bäserud, L., Reuder, J., Jonassen, M. O., Kral, S. T., Paskyabi, M. B., and Lothon, M. (2016). Proof of concept for turbulence measurements with the RPAS SUMO during the BLLAST campaign. *Atmospheric Measurement Techniques*, 9(10):4901–4913.

Borup, K. T., Fossen, T. I., and Johansen, T. A. (2016). A Nonlinear

Model-Based Wind Velocity Observer for Unmanned Aerial Vehicles. *IFAC-PapersOnLine*, 49(18):276–283.

Calmer, R. (2018). 3D wind vectors measurement with remotely piloted aircraft system for aerosol-cloud interaction study.

Calmer, R., Roberts, G. C., Preissler, J., Sanchez, K. J., Derrien, S., and O'Dowd, C. (2018). Vertical wind velocity measurements using a five-hole probe with remotely piloted aircraft to study aerosol-cloud interactions. *Atmospheric Measurement Techniques*, 11(5):2583–2599.

Canter, C. A. (2019). Hot-Wire Anemometer Measurements of Atmospheric Surface Layer Turbulence via Unmanned Aerial Vehicle.

Chilson, P. B., Gleason, A. M., Zielke, B., Feng, N., Yeary, M., Klein, P. M., Shalamunenc, W., Bonin, T., and Bocangel, W. (2009). Smartsonde : a Small UAS Platform To Support Radar Research. *34th Conference on Radar Meteorology*, pages 1–7.

Chimonas, G. (1999). Steps, waves and turbulence in the stably stratified planetary boundary layer. *Boundary-Layer Meteorology*, 90(3):397–421.

Cho, J. Y. N., Newell, R. E., Anderson, B. E., Barrick, J. D. W., and Thornhill, K. L. (2003). Characterizations of tropospheric turbulence and stability layers from aircraft observations. *Journal of Geophysical Research: Atmospheres*, 108(D20).

Coulman, C. E. (1973). Vertical profiles of small-scale temperature structure in the atmosphere. *Boundary-Layer Meteorology*, 4(1-4):169–177.

Coulman, C. E., Vernin, J., and Fuchs, A. (1995). Optical seeing—mechanism of formation of thin turbulent laminae in the atmosphere. *Applied Optics*, 34(24):5461–5474.

Dalaudier, F., Sidi, C., Crochet, M., and Vernin, J. (1994). Direct Evidence of "Sheets" in the Atmospheric Temperature Field. *Journal of the Atmospheric Sciences*, 51(2):237–248.

de Boer, gijS de Boer, Ivey, M., SChMid, B., dale LaWrenCe, darielle DexheiMer, Mei, F., john HuBBe, alBerT Bendure, jaSper HardeSTy, Shupe, M., alliSon MCCoMiSkey, hagen Telg, SChMiTT, C., MaTroSov, S., ian BrookS, jeSSie CreaMean, aMy SoloMon, david Turner, WilliaMS, C., Maahn, M., ArgroW, B., Palo, S., Long, C., ru Shan Gao, jaMeS MaTher, de Boer, gijS de Boer, Ivey, M., SChMid, B., dale LaWrenCe, darielle DexheiMer, Mei, F., john HuBBe, alBerT Bendure, jaSper HardeSTy, Shupe, M., alliSon MCCoMiSkey, hagen Telg, SChMiTT, C., MaTroSov, S., ian BrookS, jeSSie CreaMean, aMy SoloMon, david Turner, WilliaMS, C., Maahn, M., ArgroW, B., Palo, S., Long, C., ru Shan Gao, and jaMeS MaTher (2018). AFFILIATIONS: A BIRD'S-EYE VIEW Development of an Operational ARM Unmanned Aerial Capability for Atmospheric Research in Arctic Alaska. *journals.ametsoc.org*, 99(6):1197–1212.

de Boer, G., Diehl, C., Jacob, J., Houston, A., Smith, S. W., Chilson, P., Schmale, D. G., Intrieri, J., Pinto, J., Elston, J., Brus, D., Kemppinen, O., Clark, A., Lawrence, D., Bailey, S. C. C., Sama, M. P., Frazier, A., Crick, C., Natalie, V., Pillar-Little, E., Klein, P., Waugh, S., Lundquist, J. K., Barbieri, L., Kral, S. T., Jensen, A. A., Dixon, C., Borenstein, S., Hesselius, D., Human, K., Hall, P., Argrow, B., Thornberry, T., Wright, R., and Kelly, J. T. (2019). Development of community, capabilities and understanding through unmanned aircraft-based atmospheric research: The LAPSE-RATE campaign. *Bulletin of the American Meteorological Society*.

De Boer, G., Palo, S., Argrow, B., Lodolce, G., Mack, J., Gao, R. S., Telg, H., Trussel, C., Fromm, J., N Long, C., Bland, G., Maslanik, J., Schmid, B., and Hock, T. (2016). The Pilatus unmanned aircraft system for lower atmospheric research. *Atmospheric Measurement Techniques*, 9(4):1845–1857.

Dehghan, A., Hocking, W. K., and Srinivasan, R. (2014). Comparisons between multiple in-situ aircraft turbulence measurements and radar in the troposphere. *Journal of Atmospheric and Solar-Terrestrial Physics*, 118:64–77.

Doddi, A., Lawrence, D., Fritts, D., Wang, L., Lund, T., Brown, W., Zajic, D., and Kantha, L. (2021). Instabilities, Dynamics, and Energetics accompanying Atmospheric Layering (IDEAL) Campaign: High-Resolution

in situ Observations above the Nocturnal Boundary Layer. *Atmos. Meas. Tech. Discuss.*, 2021:1–33.

Eaton, F. D., Nastrom, G. D., Masson, B. S., Hahn, I. L., McCrae, K. A., Nowlin, S. R., and Berkopec, T. L. (1998). Radar and aircraft observations of a layer of strong refractivity turbulence. In *Proc.SPIE*, volume 3381.

Elston, J., Argrow, B., Stachura, M., Weibel, D., Lawrence, D., and Pope, D. (2015). Overview of Small Fixed-Wing Unmanned Aircraft for Meteorological Sampling. *journals.ametsoc.org*, 32(1):97–115.

Fairall, C. W., White, A. B., and Thomson, D. W. (1991). A stochastic model of gravity-wave-induced clear-air turbulence. *Journal of the Atmospheric Sciences*, 48(15):1771–1790.

Farnsworth, J., Sinner, D., Gloutak, D., Droste, L., and Bateman, D. (2020). Design and qualification of an unsteady low-speed wind tunnel with an upstream louver system. *Experiments in Fluids*, 61(8):181.

Fernando, H. J. S., Pardyjak, E. R., Di Sabatino, S., Chow, F. K., De Wekker, S. F. J., Hoch, S. W., Hacker, J., Pace, J. C., Pratt, T., Pu, Z., Steenburgh, W. J., Whiteman, C. D., Wang, Y., Zajic, D., Balsley, B., Dimitrova, R., Emmitt, G. D., Higgins, C. W., Hunt, J. C. R., Knievel, J. C., Lawrence, D., Liu, Y., Nadeau, D. F., Kit, E., Blomquist, B. W., Conry, P., Coppersmith, R. S., Creegan, E., Felton, M., Grachev, A., Gunawardena, N., Hang, C., Hocut, C. M., Huynh, G., Jeglum, M. E., Jensen, D., Kulandaivelu, V.,

Lehner, M., Leo, L. S., Liberzon, D., Massey, J. D., McEnerney, K., Pal, S., Price, T., Sghiatti, M., Silver, Z., Thompson, M., Zhang, H., and Zsedrovits, T. (2015). The materhorn : Unraveling the intricacies of mountain weather. *Bulletin of the American Meteorological Society*, 96(11):1945–1968.

Frehlich, R., Meillier, Y., Jensen, M. L., and Balsley, B. (2003). Turbulence Measurements with the CIRES Tethered Lifting System during CASES-99: Calibration and Spectral Analysis of Temperature and Velocity. *Journal of the Atmospheric Sciences*, 60(20):2487–2495.

Fritts, D. C. and Rastogi, P. K. (1985). Convective and dynamical instabilities due to gravity wave motions in the lower and middle atmosphere: Theory and observations. *Radio Science*, 20(6):1247–1277.

Fritts, D. C. and Wang, L. (2013). Gravity wave-fine structure interactions. Part II: Energy dissipation evolutions, statistics, and implications. *Journal of the Atmospheric Sciences*, 70(12):3735–3755.

Fritts, D. C., Wang, L., Werne, J., Lund, T., and Wan, K. (2009a). Gravity Wave Instability Dynamics at High Reynolds Numbers. Part I: Wave Field Evolution at Large Amplitudes and High Frequencies. *Journal of the Atmospheric Sciences*, 66(5):1126–1148.

Fritts, D. C., Wang, L., Werne, J., Lund, T., and Wan, K. (2009b). Gravity Wave Instability Dynamics at High Reynolds Numbers. Part II: Turbulence

Evolution, Structure, and Anisotropy. *Journal of the Atmospheric Sciences*, 66(5):1149–1171.

Fritts, D. C., Wang, L., and Werne, J. A. (2013). Gravity Wave–Fine Structure Interactions. Part I: Influences of Fine Structure Form and Orientation on Flow Evolution and Instability. *Journal of the Atmospheric Sciences*, 70(12):3710–3734.

Fua, D., Chimonas, G., Einaudi, F., and Zeman, O. (1982). Analysis of Wave-Turbulence Interaction. *Journal of the Atmospheric Sciences*, 39(11):2450–2463.

Gage, K. S. and Balsley, B. B. (1980). On the scattering and reflection mechanisms contributing to clear air radar echoes from the troposphere, stratosphere, and mesophere. *Radio Science*, 15(2):243–257.

Gage, K. S. and Green, J. L. (1978). Evidence for specular reflection from monostatic VHF radar observations of the stratosphere. *Radio Science*, 13(6):991–1001.

Garman, K. E., Hill, K. A., Wyss, P., Carlsen, M., Zimmerman, J. R., Stirm, B. H., Carney, T. Q., Santini, R., and Shepson, P. B. (2006). An airborne and wind tunnel evaluation of a wind turbulence measurement system for aircraft-based flux measurements. *Journal of Atmospheric and Oceanic Technology*, 23(12):1696–1708.

Gasch, P., Wieser, A., Lundquist, J. K., and Kalthoff, N. (2020). An LES-

based airborne Doppler lidar simulator and its application to wind profiling in inhomogeneous flow conditions. *Atmos. Meas. Tech.*, 13(3):1609–1631.

Gossard, E. E., Chadwick, R. B., Detman, T. R., and Gaynor, J. (1984). Capability of Surface-Based Clear-Air Doppler Radar for Monitoring Meteorological Structure of Elevated Layers. *Journal of Climate and Applied Meteorology*, 23(3):474–485.

Hocking, W. K. (1983). On the extraction of atmospheric turbulence parameters from radar backscatter Doppler spectra—I. Theory. *Journal of Atmospheric and Terrestrial Physics*, 45(2):89–102.

Holland, G. J., McGeer, T., and Youngren, H. (1992). Autonomous Aerosondes for Economical Atmospheric Soundings Anywhere on the Globe. *Bulletin of the American Meteorological Society*, 73(12):1987–1998.

Houston, A. L., Argrow, B., Elston, J., Lahowetz, J., Frew, E. W., and Kennedy, P. C. (2012). The Collaborative Colorado–Nebraska Unmanned Aircraft System Experiment. *Bulletin of the American Meteorological Society*, 93(1):39–54.

Hunt, J. C. R., Kaimal, J. C., and Gaynor, J. E. (1985). Some observations of turbulence structure in stable layers. *Quarterly Journal of the Royal Meteorological Society*, 111(469):793–815.

Johansen, T. A., Cristofaro, A., Sorensen, K., Hansen, J. M., and Fossen, T. I. (2015). On estimation of wind velocity, angle-of-attack and sideslip angle

of small UAVs using standard sensors. In *2015 International Conference on Unmanned Aircraft Systems, ICUAS 2015*, pages 510–519. Institute of Electrical and Electronics Engineers Inc.

Kantha, L., Lawrence, D., Luce, H., Hashiguchi, H., Tsuda, T., Wilson, R., Mixa, T., and Yabuki, M. (2017a). Shigaraki UAV-Radar Experiment (ShUREX): overview of the campaign with some preliminary results. *Progress in Earth and Planetary Science*, 4(1).

Kantha, L., Lawrence, D., Luce, H., Hashiguchi, H., Tsuda, T., Wilson, R., Mixa, T., and Yabuki, M. (2017b). Shigaraki UAV-Radar Experiment (ShUREX): overview of the campaign with some preliminary results. *Progress in Earth and Planetary Science*, 4(1):19.

Kantha, L. and Luce, H. (2018). Mixing Coefficient in Stably Stratified Flows. *Journal of Physical Oceanography*, 48(11):2649–2665.

Kantha, L., Luce, H., Hashiguchi, H., and Doddi, A. (2019). Atmospheric structures in the troposphere as revealed by high-resolution backscatter images from MU radar operating in range-imaging mode. *Progress in Earth and Planetary Science*, 6(1):32.

Kolmogorov, A. N. (1962). A refinement of previous hypotheses concerning the local structure of turbulence in a viscous incompressible fluid at high Reynolds number. *Journal of Fluid Mechanics*, 13(1):82–85.

Lawrence, D. A. and Balsley, B. B. (2013). Design of a low-cost UAS for

high-resolution atmospheric sensing. In *AIAA Infotech at Aerospace (I at A) Conference*.

Lawrence, D. A., Frew, E. W., and Pisano, W. J. (2008). Lyapunov Vector Fields for Autonomous Unmanned Aircraft Flight Control. *arc.aiaa.org*, 31(5):1220–1229.

Lenschow, D. (1972). The Measurement of Air Velocity and Temperature Using The NCAR Buffalo Aircraft Measuring System.

Luce, H., Crochet, M., Dalaudier, F., and Sidi, C. (1995). Interpretation of VHF ST radar vertical echoes from in situ temperature sheet observations. *Radio Science*, 30(4):1003–1025.

Luce, H., Fukao, S., Yamamoto, M., Sidi, C., and Dalaudier, F. (2001). Validation of Winds Measured by MU Radar with GPS Radiosondes during the MUTSI Campaign. *Journal of Atmospheric and Oceanic Technology*, 18(6):817–829.

Luce, H., Kantha, L., Hashiguchi, H., and Lawrence, D. (2019). Estimation of Turbulence Parameters in the Lower Troposphere from ShUREX (2016–2017) UAV Data.

Luce, H., Kantha, L., Hashiguchi, H., Lawrence, D., and Doddi, A. (2018a). Turbulence kinetic energy dissipation rates estimated from concurrent UAV and MU radar measurements. *Earth, Planets and Space*, 70(1).

Luce, H., Kantha, L., Hashiguchi, H., Lawrence, D., Mixa, T., Yabuki, M.,

and Tsuda, T. (2018b). Vertical structure of the lower troposphere derived from MU radar, unmanned aerial vehicle, and balloon measurements during ShUREX 2015. *Progress in Earth and Planetary Science*, 5(1).

Luce, H., Kantha, L., Hashiguchi, H., Lawrence, D., Yabuki, M., Tsuda, T., and Mixa, T. (2017). Comparisons between high-resolution profiles of squared refractive index gradient M 2 measured by the Middle and Upper Atmosphere Radar and unmanned aerial vehicles (UAVs) during the Shigaraki UAV-Radar Experiment 2015 campaign. 35:423–441.

Lundquist, J. K., Churchfield, M. J., Lee, S., and Clifton, A. (2015). Quantifying error of lidar and sodar Doppler beam swinging measurements of wind turbine wakes using computational fluid dynamics. *Atmos. Meas. Tech.*, 8(2):907–920.

Mahrt, L. (1999). Stratified Atmospheric Boundary Layers. *Boundary-Layer Meteorology*, 90(3):375–396.

Marwitz, J. D. (1972). The Structure and Motion of Severe Hailstorms. Part I: Supercell Storms. *Journal of Applied Meteorology*, 11(1):166–179.

Meischner, P., Baumann, R., Höller, H., and Jank, T. (2001). Eddy Dissipation Rates in Thunderstorms Estimated by Doppler Radar in Relation to Aircraft In Situ Measurements. *Journal of Atmospheric and Oceanic Technology*, 18(10):1609–1627.

Muschinski, A., Frehich, R., Jensen, M., Hugo, R., Hoff, A., Eaton, F., Bals-

ley, B., Frehlich, R., Jensen, M., Hugo, R., Hoff, A., Eaton, F., and Balsley, B. (2001a). Fine-Scale Measurements Of Turbulence In The Lower Troposphere: An Intercomparison Between A Kite- And Balloon-Borne, And A Helicopter-Borne Measurement System. *Boundary-Layer Meteorology*, 98(2):219–250.

Muschinski, A., Frehlich, R., Jensen, M., Hugo, R., Hoff, A., Eaton, F., and Balsley, B. (2001b). Fine-scale measurements of turbulence in the lower troposphere: An intercomparison between a kit-and balloon-borne, and a helicopter-borne measurement system. *Boundary-Layer Meteorology*, 98(2):219–250.

Muschinski, A. and Wode, C. (1998). First In Situ Evidence for Coexisting Submeter Temperature and Humidity Sheets in the Lower Free Troposphere. *Journal of the Atmospheric Sciences*, 55(18):2893–2906.

Neumann, P. P. and Bartholmai, M. (2015). Real-time wind estimation on a micro unmanned aerial vehicle using its inertial measurement unit. *Sensors and Actuators, A: Physical*, 235:300–310.

Payne, F. R. and Lumley, J. L. (1966). One-dimensional spectra derived from an airborne hot-wire anemometer. *Quarterly Journal of the Royal Meteorological Society*, 92(393):397–401.

Rautenberg, A., Allgeier, J., Jung, S., and Bange, J. (2019). Calibration Procedure and Accuracy of Wind and Turbulence Measurements with Five-

Hole Probes on Fixed-Wing Unmanned Aircraft in the Atmospheric Boundary Layer and Wind Turbine Wakes.

Rautenberg, A., Graf, M. S., Wildmann, N., Platis, A., and Bange, J. (2018). Reviewing wind measurement approaches for fixed-wing unmanned aircraft. *Atmosphere*, 9(11):1–24.

Reineman, B. D., Lenain, L., Statom, N. M., and Melville, W. K. (2013). Development and Testing of Instrumentation for UAV-Based Flux Measurements within Terrestrial and Marine Atmospheric Boundary Layers. *Journal of Atmospheric and Oceanic Technology*, 30(7):1295–1319.

Reuder, J., Brisset, P., Jonassen, M., Müller, M., and Mayer, S. (2008). SUMO: A Small Unmanned Meteorological Observer for atmospheric boundary layer research. *IOP Conference Series: Earth and Environmental Science*, 1.

Röttger, J. (1980). Structure and dynamics of the stratosphere and mesosphere revealed by VHF radar investigations. *pure and applied geophysics*, 118(1):494–527.

Röttger, J. and Liu, C. H. (1978). Partial reflection and scattering of VHF radar signals from the clear atmosphere. *Geophysical Research Letters*, 5(5):357–360.

Saarenrinne, P. and Piirto, M. (2000). Turbulent kinetic energy dissipation

rate estimation from PIV velocity vector fields. *Experiments in Fluids*, 29(1):S300–S307.

Scipión, D. E., Lawrence, D. A., Milla, M. A., Woodman, R. F., Lume, D. A., and Balsley, B. B. (2016). Simultaneous observations of structure function parameter of refractive index using a high-resolution radar and the DataHawk small airborne measurement system. *ann-geophys.net*, 34:767–780.

Sidi, C., Lefrere, J., Dalaudier, F., and Barat, J. (1988). An improved atmospheric buoyancy wave spectrum model. *Journal of Geophysical Research: Atmospheres*, 93(D1):774–790.

Siebert, H., Lehmann, K., and Shaw, R. A. (2007). On the Use of Hot-Wire Anemometers for Turbulence Measurements in Clouds. *Journal of Atmospheric and Oceanic Technology*, 24(6):980–993.

Smith, S. A., Fritts, D. C., and Vanzandt, T. E. (1987). Evidence for a Saturated Spectrum of Atmospheric Gravity Waves. *Journal of the Atmospheric Sciences*, 44(10):1404–1410.

Tennekes, H. and Lumley, J. L. (2011). *A first course in turbulence*. MIT Press, Cambridge, Mass.

Theuerkauf, A., Gerding, M., and Lübken, F.-J. (2011). LITOS – a new balloon-borne instrument for fine-scale turbulence soundings in the stratosphere. *Atmos. Meas. Tech.*, 4(1):55–66.

Thomas, R. M., Lehmann, K., Nguyen, H., Jackson, D. L., Wolfe, D., and Ramanathan, V. (2012a). Measurement of turbulent water vapor fluxes using a lightweight unmanned aerial vehicle system. *Atmos. Meas. Tech.*, 5(1):243–257.

Thomas, R. M., Lehmann, K., Nguyen, H., Jackson, D. L., Wolfe, D., and Ramanathan, V. (2012b). Measurement of turbulent water vapor fluxes using a lightweight unmanned aerial vehicle system. *Atmos. Meas. Tech.*, 5(1):243–257.

Tjernström, M., Balsley, B. B., Svensson, G., and Nappo, C. J. (2009). The Effects of Critical Layers on Residual Layer Turbulence. *Journal of the Atmospheric Sciences*, 66(2):468–480.

van den Kroonenberg, A., Martin, T., Buschmann, M., Bange, J., and Vörsmann, P. (2008). Measuring the Wind Vector Using the Autonomous Mini Aerial Vehicle M2AV. *Journal of Atmospheric and Oceanic Technology*, 25(11):1969–1982.

VanZandt, T. E., Green, J. L., Gage, K. S., and Clark, W. L. (1978). Vertical profiles of refractivity turbulence structure constant: Comparison of observations by the Sunset Radar with a new theoretical model. *Radio Science*, 13(5):819–829.

Velasco-Carrau, J., García-Nieto, S., Salcedo, J. V., and Bishop, R. H. (2016). Multi-Objective Optimization for Wind Estimation and Aircraft Model

Identification. *Journal of Guidance, Control, and Dynamics*, 39(2):372–389.

Wainwright, C. E., Stepanian, P. M., Chilson, P. B., Palmer, R. D., Fedorovich, E., and Gibbs, J. A. (2014). A time series sodar simulator based on large-eddy simulation. *Journal of Atmospheric and Oceanic Technology*, 31(4):876–889.

Weiss, G. (1961). Wave Propagation in a Turbulent Medium. V. I. Tatarski. Translated by R. A. Silverman. McGraw-Hill, New York, 1961. 285 pp. Illus. 9.75. *Science*, 134(3475) : 324 − −325.

Wildmann, N., Hofsäß, M., Weimer, F., Joos, A., and Bange, J. (2014a). MASC-a small Remotely Piloted Aircraft (RPA) for wind energy research. *Adv. Sci. Res*, 11:55–61.

Wildmann, N., Ravi, S., and Bange, J. (2014b). Towards higher accuracy and better frequency response with standard multi-hole probes in turbulence measurement with remotely piloted aircraft (RPA). *Atmospheric Measurement Techniques*, 7(4):1027–1041.

Witte, B. M., Schlagenhauf, C., Mullen, J., Helvey, J. P., Thamann, M. A., and Bailey, S. (2016). Fundamental Turbulence Measurement with Unmanned Aerial Vehicles (Invited). In *8th AIAA Atmospheric and Space Environments Conference*, AIAA AVIATION Forum. American Institute of Aeronautics and Astronautics.

Witte, B. M., Singler, R. F., and Bailey, S. C. C. (2017). Development of an unmanned aerial vehicle for the measurement of turbulence in the atmospheric boundary layer. *Atmosphere*, 8(10):1–25.

Woodman, R. F. and Chu, Y. (1989). Aspect sensitivity measurements of VHF backscatter made with the Chung-Li radar: Plausible mechanisms. *Radio Science*, 24(02):113–125.

Woodman, R. F. and Guillen, A. (1974). Radar Observations of Winds and Turbulence in the Stratosphere and Mesosphere. *Journal of the Atmospheric Sciences*, 31(2):493–505.

Wyngaard, J. C. (1968). Measurement of small-scale turbulence structure with hot wires. *Journal of Physics E: Scientific Instruments*, 1(11):1105–1108.

Xing-Sheng, L., Gaynor, J. E., and Kaimal, J. C. (1983). A study of multiple stable layers in the nocturnal lower atmosphere. *Boundary-Layer Meteorology*, 26(2):157–168.